Theoretical Studies of Lithium-Ion Diffusion in LISICON-Type Solid Electrolytes

Koji Fujimura

2013

Contents

Chapter 1

General Introduction

In this thesis, theoretical studies of lithium-ion diffusion in inorganic solid electrolytes are introduced. We focused on LIthium Super Ionic CONductor (LISICON) type electrolytes as candidate systems. The purpose of this study is to elucidate Li-ion migration mechanism in solid electrolytes using first-principles calculations. Based on the learned knowledge, we aim to design novel solid electrolytes exhibiting high ionic conductivity. In this chapter, backgrounds of this study, especially experimental researches related to LISICON-type electrolytes, are presented. And then, overviews of Chapter 2-5 are described.

1. 1. Lithium-Ion Solid Electrolytes

Lithium-ion secondary batteries are important for energy storage in a wide variety of applications as exemplified by consumer electronics, transportation and stationary load-leveling system. Battery performance depends markedly on the materials including cathode, anode, separator and electrolyte. Our present work is concerned with the electrolyte. There has been considerable interest in inorganic solid electrolytes for use in all-solid-state batteries over the last few decades [1-3]. Solid electrolytes present potential advantages, such as absence of leakage and pollution, a large electrochemical stability window, thermal stability, a high resistance to shocks and vibrations, and easy miniaturization, especially using thin-film techniques. However, their ionic conductivities are typically lower than those of commercially-used organic liquid electrolytes. The solid electrolytes must possess high ionic conductivity at operating temperature (preferably ambient temperature). If polycrystalline materials are used, a negligibly small grain-boundary resistance is important. Electronic conductivity must be negligible to avoid internal short circuits. They should be stable in contact with the electrodes, especially with elemental Li or Li alloy anodes. Matching of thermal expansion coefficients with both electrodes is also important. Toward industrial

developments, candidate materials should be non-hygroscopic, environmentally benign, and cheap to produce. In this study, especially the ionic conductivity which is the most important properties for electrolytes is discussed.

The properties of inorganic solid electrolytes depend critically on their composition, constituent elements and crystal structure. Figure 1.1 shows the variation in conductivity measured for several well-known Li-ion solid electrolytes [4-11]. For comparison, the conductivity of organic electrolyte is also plotted [12]. Oxide-based Li-ion conductors have been energetically studied since the 1970s. Those representative compounds are LISICON-type [4,13], NASICON-type [14,15], perovskite-type Lithium Lanthanum Titanates (LLTO) [6,16,17], and garnet-type Lithium Lanthanum Zirconates (LLZ) [7]. In about a last decade, various sulfide-based Li-ion conductors exhibiting better ionic conductivities over oxides have been discovered [8,9,18-22]. And, in 2011, Kamaya *et al.* reported $Li_{10}GeP_2S_{12}$ which exhibits the ionic conductivity of 12 mS cm^{-1} at room temperature [10]. This conductivity exceeds those of organic electrolytes as seen in Figure 1.1.

In spite of abundant experimental researches on solid electrolytes, theoretical understanding about Li-ion migration mechanisms in solid electrolytes is not still enough. In addition, design principle for achieving high ionic conductivity has not been constructed yet. According to past references [8,23], with the view to exhibit good ionic conductivity for crystalline ionic conductors, the following qualitative criteria are required. (i) mobile ions should have a suitable size for conduction pathways in the lattice, (ii) highly polarizable mobile ions and anion sublattices are preferable, and (iii) mobile ions should be disorderly arranged. In order to theoretically evaluate these criteria, first-principles calculations based on density functional theory (DFT) are expected to be greatly useful thanks to rapidly-developing computer performance. The criteria (i) and (ii) are taken into account if the atomic and electronic structures can be accurately estimated in first-principles calculations. Moreover, it is possible to investigate the criterion (iii) using the DFT calculations for a series of mobile-ion configurations or the first-principles molecular dynamics (FPMD) simulations. They will be discussed more fully in Chapter 2 and 3. In this study, we adopted LISICON-type electrolytes. The original LISICON composition is $Li_{3.5}Zn_{0.25}GeO_4$. This exhibits relatively high ionic conductivity at high temperatures among solid electrolytes. A lot of

solid solutions which substitute diverse elements for Zn or Ge have been also reported and are called LISICONs [1]. Owing to the abundant experimental data, LISICONs are expected to be suitable to evaluate the reproducibility of systematic first-principles calculations for a diverse range of compositions. Further details of LISICONs are introduced in next section.

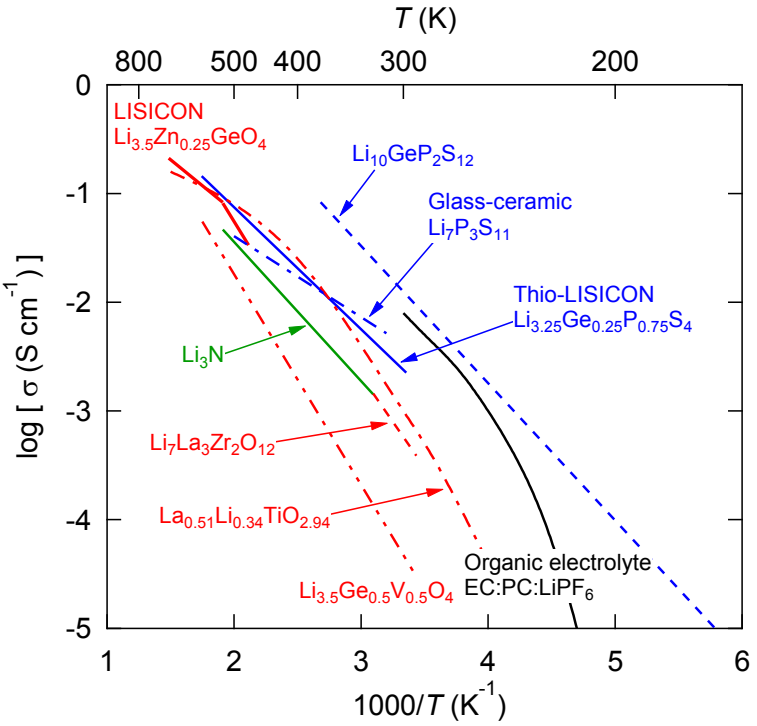

Figure 1.1. Arrhenius plot of conductivities measured for well-known inorganic Li-ion solid electrolytes.

1. 2. LISICONs

The first material to be named LISICON is $Li_{3.5}Zn_{0.25}GeO_4$ which is a member of the solid solution, $Li_{2+2x}Zn_{1-x}GeO_4$ ($0 \le x \le 1$) [4]. $Li_{3.5}Zn_{0.25}GeO_4$ ($x = 0.75$) exhibits high conductivity, 0.125 S cm^{-1} at 573 K. In the pseudobinary Li_2ZnGeO_4-Li_4GeO_4 phase diagram shown in Figure 1.2, the ground state structures change from β to γ and then α phase with increasing x from 0 to 1 at low temperatures [13]. According to structure analysis using neutron diffraction [24,25], $Li_{3.5}Zn_{0.25}GeO_4$ ($x = 0.75$) and $Li_3Zn_{0.5}GeO_4$ ($x = 0.5$) were identified as γ structure at low temperatures. Structures of α, β and γ phases in $Li_{2+2x}Zn_{1-x}GeO_4$ are shown in Figure 1.3. Oxide ions form sublattice of a distorted hexagonal close packing structure. Cations occupy regular tetrahedral sites. This site corresponds to one of two face-sharing tetrahedral coordination sites of a trigonal bipyramid. When the number of cations is more than that of oxide ions, excess Li ions are put into interstitial octahedral sites. Differences between the three structures are characterized by directions of [GeO_4] apexes. In β structure, an apex of all [GeO_4] tetrahedra is oriented in the same direction along the c axis, while in α and γ structure, half of [GeO_4] tetrahedra turn to the opposite direction. The b-axis lattice constant in a primitive cell of γ structure is about twice as long as that of α structure.

Since the discovery of LISICON, a lot of solid solutions which substitute diverse elements for Zn or Ge have been investigated and are called LISICONs. LISICONs can be represented by general formula $Li_{8-c}A_aB_bO_4$, where $c = ma + nb$. m and n denote the formal valence of cations A and B, respectively. In most cases of LISICONs, A corresponds to divalent, trivalent or pentavalent cation and B corresponds to tetravalent cation. We label those solid solutions as II-IV, III-IV and V-IV systems based on the valence states of the corresponding cations A and B.

We comprehensively surveyed the experimental conductivity data of LISICONs in launching this study. A collection of bulk ionic conductivities and the respective activation energies is given in Table 1.1 [4,5,26-53]. The conductivities of end member corresponding to $Li_{8-c}A_aO_4$ and Li_4BO_4 are also listed. Those end members are poor Li-ion conductors. Aliovalent cation doping of the end member leads to an increase in conductivity. Namely, conductivities of intermediate compositions are much higher than those of the end members. The general formula of II-IV system is $Li_{4-2x}A_xBO_4$ ($0 \le x \le 1$), where A is Zn^{2+} or Mg^{2+}, and B = Ge^{4+} or Si^{4+}. Replacement of Zn by Mg

or Ge by Si tends to cause a decrease in conductivity [4]. In III-IV system, two kinds of solid solutions have been reported. One solid solution is $Li_{4-3x}A_xBO_4$ ($0 \le x \le 0.5$) in which A is substituted for Li in Li_4BO_4, and the other is $Li_{4+x}A_xB_{1-x}O_4$ ($0 \le x \le 1$) in which A is substituted for B in Li_4BO_4, where A is Al^{3+} or Ga^{3+}, and B = Ge^{4+} or Si^{4+}. V-IV system has the general formula $Li_{4-x}A_xB_{1-x}O_4$ ($0 \le x \le 1$), where A is P^{5+}, V^{5+} or As^{5+}, and B = Ge^{4+}, Si^{4+} or Ti^{4+}. In this system, A is substituted for B in Li_4BO_4 and thereby Li vacancies are created. $Li_{3.4}V_{0.6}Ge_{0.4}O_4$, $Li_{3.6}As_{0.4}Ge_{0.6}O_4$ and $Li_{3.5}V_{0.5}Ti_{0.5}O_4$ exhibit the highest room temperature conductivity, 4×10^{-5} S cm^{-1}, among synthesized LISICON-type oxides.

The crystallographic data based on the experimental structure analysis for LISICONs are shown in Table 1.2 [4,24,25,52,54-69]. The end members $Li_{8-c}AO_4$ with divalent or trivalent cation A and Li_4BO_4 with tetravalent cation B have antifluorite (AF) and α structure, respectively. Li_3PO_4, Li_3AsO_4 and Li_2ZnGeO_4 in which the number of cations is the same as that of oxide ions form β structure at low temperature. As for the intermediate compositions shown in Table 1.2, the germanate systems form γ structure, while the silicate systems form α structure. West *et al.* constructed the pseudobinary phase diagrams about $Li_{4-2x}Zn_xGeO_4$ [13], $Li_{4-2x}Zn_xSiO_4$ [70], $Li_{4-2x}Mg_xSiO_4$ [71], $Li_{4-3x}Al_xGeO_4$ [45], $Li_{4-3x}Ga_xGeO_4$ [47], $Li_{4-3x}Ga_xSiO_4$ [72], $Li_{4-x}P_xSi_{1-x}O_4$ [73], and $Li_{4-x}As_xSi_{1-x}O_4$ [33]. The germanate systems form wide ranges of single γ phase. For example γ phase is stable at 1000 K in the range of $0.20 < x < 0.68$ in $Li_{4-2x}Zn_xGeO_4$, $0.04 < x < 0.30$ in $Li_{4-3x}Al_xGeO_4$ and $0.04 < x < 0.36$ in $Li_{4-3x}Ga_xGeO_4$. On the other hand, the range of γ phase in the silicate systems is smaller than that of the germanate systems. This difference of stable structure may be why the germanate systems exhibit higher conductivities than the silicate systems.

Sulfide systems found by Kanno *et al.* [8,18,19] also have the LISICON structure and are called thio-LISICONs in this study. The reported ionic conductivities and crystallographic data about sulfide systems are also given in Table 1.1 and 1.2, respectively [8,18,19,74-77]. The general formula is expressed as $Li_{8-c}A_aB_bS_4$, where A = Zn^{2+}, Al^{3+}, Ga^{3+} or P^{5+}, B = Ge^{4+} or Si^{4+}. Room temperature conductivity over 10^{-4} S cm^{-1} can be obtained in some compositions. Among a wide range of thio-LISICONs, $Li_{3.25}P_{0.75}Ge_{0.25}S_4$ shows the highest ionic conductivity of 2×10^{-3} S cm^{-1} at 298 K. A sulfide ion has larger ionic radius and larger polarizability than an oxide ion. This

character of a sulfide ion is supposed to improve the Li-ion diffusivity. However, theoretical understanding about Li-ion diffusion mechanisms of oxides and sulfides is not still enough. This issue will be discussed in Chapter 3.

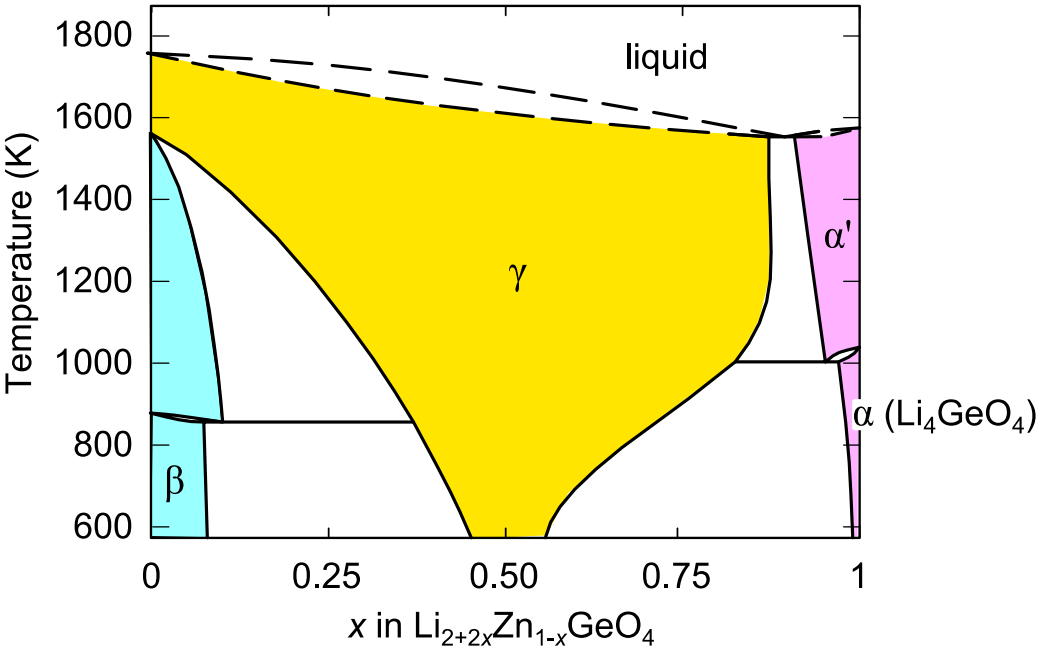

Figure 1.2. Pseudobinary Li_2ZnGeO_4-Li_4GeO_4 phase diagram.

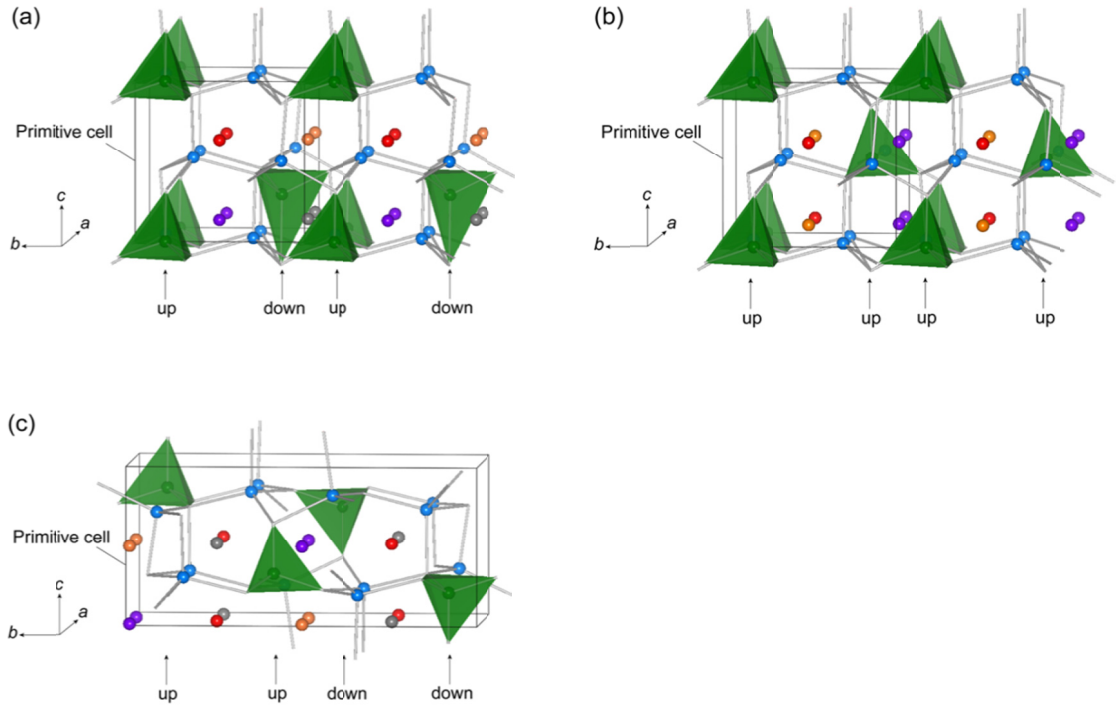

Figure 1.3. Crystal structures of (a) α, (b) β and (c) γ phases in $Li_{2+2x}Zn_{1-x}GeO_4$. The cuboid denotes a primitive cell of each structure. The green balls denote Ge ions. The light-blue balls denote Li or Zn ions at regular tetrahedral sites. Oxide ions are not shown in this figure. The "up/down" means the direction to the *c* axis of [GeO_4] apexes. Interstitial octahedral sites are categorized according to space group of each structure. In the panel (a), the red, orange, purple and gray balls denote interstitial octahedral sites, Li(3), Li(4), Li(5) and Li(6), respectively. In the panel (b), the red, orange and purple balls denote interstitial octahedral sites, Li(3), Li(4) and Li(5), respectively. In the panel (c), the red, orange, purple and gray balls denote interstitial octahedral sites, Li(3), Li(4), Li(5) and Li(6), respectively.

Table 1.1. Bulk ionic conductivities σ and activation energies E_a of LISICON-type compounds. A parenthesis of the E_a row is temperature range used to estimate E_a. The experimental conductivity data denoted by an asterisk of the ML row were used in machine learning algorithms in Chapter 4.

Oxides, End member

Compound		T (K)	σ (S cm^{-1})	E_a (eV)	Reference	ML
Li-Zn-O	Li_6ZnO_4	473	1.2×10^{-6}	0.759	[26] Table 6	
		673	5.8×10^{-4}	(393 - 653 K)		
		723	3.2×10^{-2}			
		423	2.00×10^{-7}	0.75	[27] Fig. 5,6	
		473	1.58×10^{-6}			
		523	1.00×10^{-5}			
		573	5.01×10^{-5}			
		623	1.58×10^{-4}			
Li-Al-O	Li_5AlO_4	473	2.3×10^{-7}	1.24	[26] Table 6	
		673	3.2×10^{-3}	(393 - 653 K)		
		723	3.0×10^{-1}			
		556	1.00×10^{-5}		[28] Fig. 4	
		690	2.00×10^{-3}			
		690	3.16×10^{-1}			
		833	7.94×10^{-1}			
Li-Ga-O	Li_5GaO_4	473	7.5×10^{-7}	0.893	[26] Table 6	
		673	5.8×10^{-4}	(393 - 653 K)		
		723	4.7×10^{-2}			
		423	2.51×10^{-6}	0.73	[27] Fig. 5,6	
		473	2.00×10^{-5}			
		523	1.00×10^{-4}			
		573	5.01×10^{-4}			
		623	1.26×10^{-3}			
Li-Si-O	Li_4SiO_4	373	7.0×10^{-10}		[29] Fig. 1	
		573	1.8×10^{-5}			
		373	3.0×10^{-9}		[28] Fig. 2	
		473	1.58×10^{-6}		[30] Fig. 3	
		523	1.00×10^{-5}			
		573	5.01×10^{-5}			
		623	2.00×10^{-4}			
		673	6.31×10^{-4}			
		723	2.51×10^{-3}			
		323	5.01×10^{-9}		[31] Fig. 3	
		400	1.00×10^{-7}			

		500	3.98×10^{-6}		
		523	1.00×10^{-5}		
		588	1.00×10^{-4}		
		714	1.58×10^{-3}		
		833	2.00×10^{-2}		
		909	1.26×10^{-1}		
		1000	6.31×10^{-1}		
		373	1.3×10^{-9}	0.867 (298 - 584 K)	[26] Table 4
		298	2.4×10^{-10}		[32] Table 1
		673	2.2×10^{-3}		
				1.005 (T > 563 K) 0.674 (T < 563 K)	[33] Fig. 7
Li-Ge-O	Li_4GeO_4	444	1.42×10^{-7}		[34] Fig. 7
		500	1.26×10^{-6}		
		588	2.70×10^{-5}		
		667	1.19×10^{-4}		
		800	9.93×10^{-4}		
		1000	1.58×10^{-2}		
		1073	1.48×10^{-1}		
		1173	1.86×10^{-1}		
		465	2.15×10^{-7}		[32] Fig. 2
		556	5.69×10^{-6}		
		645	4.90×10^{-5}		
		741	2.69×10^{-4}		
		833	1.20×10^{-3}		
		935	3.38×10^{-3}		
		1000	3.16×10^{-2}		
		1031	6.12×10^{-2}		
		1111	1.43×10^{-1}		
		298	3.10×10^{-12}	0.828	[32] Table 1
		673	8.70×10^{-5}		
Li-Ti-O	Li_4TiO_4	455	5.53×10^{-6}		[34] Fig. 5
		500	1.59×10^{-5}		
		667	7.52×10^{-4}		
Li-P-O	Li_3PO_4	373	1.30×10^{-14}	1.305 (427 - 887 K)	[26] Table 4
		523	1.52×10^{-9}		[26] Fig. 4
		873	7.23×10^{-5}		

Li-V-O	Li_3VO_4	473	5.01×10^{-9}	0.80	[35] Fig. 1	
		573	1.00×10^{-7}			

Oxides, II-IV system

Compound		T (K)	σ (S cm^{-1})	E_a (eV)	Reference	ML
Li-Zn-Ge-O	$Li_{3.5}Zn_{0.25}GeO_4$	473	3.35×10^{-2}	0.24	[4] Fig. 2	*
		523	8.16×10^{-2}	(523 - 673 K)		*
		573	1.24×10^{-1}			*
		623	1.61×10^{-1}			*
		673	2.10×10^{-1}			*
		483	1.66×10^{-3}	0.4	[36] Fig. 2	*
		549	5.46×10^{-3}			*
		599	1.00×10^{-2}			*
		641	1.40×10^{-2}			*
		694	2.59×10^{-2}			*
		735	3.13×10^{-2}			*
		775	4.52×10^{-2}			*
		333	2.73×10^{-5}	0.60	[37] Fig. 1,	*
		370	1.34×10^{-4}	(306 - 578 K)	Table 1	*
		417	9.76×10^{-4}			*
		476	4.67×10^{-4}			*
		323	2.00×10^{-6}	0.56	[38] Table 1	*
		373	5.00×10^{-5}	(323 - 573 K)		*
		473	1.70×10^{-3}	0.42		*
		573	1.25×10^{-2}	(573 - 773 K)		*
		673	4.20×10^{-2}			*
		773	9.00×10^{-2}			*
		333	1.89×10^{-6}		[39] Fig. 7	*
		350	5.70×10^{-6}			*
		390	8.11×10^{-5}			*
		444	1.13×10^{-3}			*
	$Li_3Zn_{0.5}GeO_4$	573	2.77×10^{-2}		[4] Fig. 3	*
		673	5.92×10^{-2}			*
		333	5.49×10^{-5}		[37] Fig. 1,	*
		370	2.22×10^{-4}		Table 1	*
		417	7.23×10^{-4}			*
		476	2.32×10^{-3}			*
		313	1.27×10^{-8}		[5] Fig. 7	*
		345	1.45×10^{-7}			*
		370	1.07×10^{-6}			*

		392	8.06×10^{-6}		*
		444	1.79×10^{-4}		*
		513	1.95×10^{-3}		*
		606	8.27×10^{-3}		*
		714	2.22×10^{-2}		*
		870	2.89×10^{-2}		*
	$Li_{2.5}Zn_{0.75}GeO_4$	573	1.75×10^{-3}	[4] Fig. 3	*
		673	9.38×10^{-3}		*
Li-Mg-Ge-O	$Li_{3.5}Mg_{0.25}GeO_4$	573	2.20×10^{-2}	[4] Fig. 3	*
		673	5.92×10^{-2}		*
	$Li_3Mg_{0.5}GeO_4$	573	8.75×10^{-3}	[4] Fig. 3	*
		673	4.70×10^{-2}		*
	$Li_{2.5}Mg_{0.75}GeO_4$	573	1.39×10^{-3}	[4] Fig. 3	*
		673	1.18×10^{-2}		*
Li-Zn-Si-O	$Li_{3.5}Zn_{0.25}SiO_4$	573	2.77×10^{-3}	[4] Fig. 3	*
		673	1.87×10^{-2}		*
	$Li_3Zn_{0.5}SiO_4$	573	6.95×10^{-3}	[4] Fig. 3	*
		673	3.73×10^{-2}		*
	$Li_{2.5}Zn_{0.75}SiO_4$	573	1.39×10^{-3}	[4] Fig. 3	*
		673	5.92×10^{-3}		*
	$Li_{3.4}Zn_{0.3}SiO_4$	714	2.00×10^{-4}	[31] Fig. 3	
		973	1.58×10^{-2}		
	$Li_{2.8}Zn_{0.6}SiO_4$	455	3.16×10^{-7}	[31] Fig. 4	
		714	7.94×10^{-4}		
Li-Mg-Si-O	$Li_{3.5}Mg_{0.25}SiO_4$	573	5.52×10^{-4}	[4] Fig. 3	
		673	4.70×10^{-3}		
	$Li_3Mg_{0.5}SiO_4$	573	8.75×10^{-4}	[4] Fig. 3	
		673	1.49×10^{-2}		
	$Li_{2.5}Mg_{0.75}SiO_4$	573	6.95×10^{-4}	[4] Fig. 3	
		673	1.18×10^{-2}		
	$Li_{3.8}Mg_{0.1}SiO_4$	473	1.26×10^{-5}	[30] Fig. 3	
		523	7.94×10^{-5}		
		573	5.01×10^{-4}		
		623	2.00×10^{-3}		
		673	6.31×10^{-3}		
		723	1.26×10^{-2}		
	$Li_{3.6}Mg_{0.2}SiO_4$	473	1.58×10^{-5}	[30] Fig. 3	
		523	1.26×10^{-4}		
		573	1.00×10^{-3}		
		623	3.16×10^{-3}		
		673	1.00×10^{-2}		

	723	2.51×10^{-2}		
$Li_{3.4}Mg_{0.3}SiO_4$	473	1.58×10^{-5}	[30] Fig. 3	
	523	1.58×10^{-4}		
	573	1.26×10^{-3}		
	623	5.01×10^{-3}		
	673	1.26×10^{-2}		
	723	3.98×10^{-2}		
$Li_{3.2}Mg_{0.4}SiO_4$	473	2.27×10^{-5}	[30] Table 1	
	523	1.68×10^{-4}		
	573	1.49×10^{-3}		
	623	6.32×10^{-3}		
	673	1.45×10^{-2}		
	723	5.01×10^{-2}		
$Li_{2.8}Mg_{0.6}SiO_4$	473	2.00×10^{-5}	[30] Fig. 3	
	523	2.00×10^{-4}		
	573	1.26×10^{-3}		
	623	6.31×10^{-3}		
	673	1.26×10^{-2}		
	723	2.51×10^{-2}		

Oxides, III-IV system

Compound		T (K)	σ (S cm^{-1})	E_a (eV)	Reference	ML
Li-Al-Si-O	$Li_{4.2}Al_{0.2}Si_{0.8}O_4$	373	2.00×10^{-6}	0.580	[29] Fig. 1	
		573	1.58×10^{-3}			
	$Li_{4.3}Al_{0.3}Si_{0.7}O_4$	434	6.40×10^{-5}		[40] Table 2	
		483	2.56×10^{-4}			
		533	7.75×10^{-4}			
		595	3.40×10^{-3}			
		652	5.68×10^{-3}			
	$Li_{4.4}Al_{0.4}Si_{0.6}O_4$	573	8.0×10^{-3}	0.56	[28] Table 1	
		298	2.8×10^{-7}		[41] Table 7	
		473	7.6×10^{-4}			
		573	8.0×10^{-3}			
	$Li_{4.5}Al_{0.5}Si_{0.5}O_4$	298	2.3×10^{-7}		[42]	*
	$Li_{4.6}Al_{0.6}Si_{0.4}O_4$	473	7.7×10^{-5}		[41] Table 7	
		573	1.0×10^{-3}			
	$Li_{3.82}Al_{0.06}SiO_4$	483	2.4×10^{-6}		[40] Table 2	
		537	1.6×10^{-5}			
		589	5.6×10^{-5}			
		649	2.0×10^{-4}			

		695	4.4×10^{-4}			
	$Li_{3.55}Al_{0.15}SiO_4$	323	3.98×10^{-7}	0.74	[43] Fig. 2,	
		345	1.58×10^{-6}		Table 2	
		385	2.00×10^{-5}			
	$Li_{3.4}Al_{0.2}SiO_4$	323	1.00×10^{-6}	0.68	[43] Fig. 2,	
		333	2.51×10^{-6}		Table 2	
		345	5.01×10^{-6}			
		370	2.51×10^{-5}			
	$Li_{2.8}Al_{0.4}SiO_4$	323	1.58×10^{-7}	0.78	[43] Fig. 2,	
		345	7.94×10^{-7}		Table 2	
		385	1.00×10^{-5}			
	$Li_{2.65}Al_{0.45}SiO_4$	357	1.00×10^{-7}	0.78	[43] Fig. 2,	
		370	2.51×10^{-7}		Table 2	
		400	2.00×10^{-6}			
		435	6.31×10^{-6}			
	$Li_{3.55}Al_{0.15}SiO_4$	373	1.3×10^{-5}		[28] Fig. 2	
	$Li_{3.4}Al_{0.2}SiO_4$	373	1.5×10^{-5}		[28] Fig. 2	
	$Li_{3.25}Al_{0.25}SiO_4$	373	1.5×10^{-5}		[28] Fig. 2	*
	$Li_{2.8}Al_{0.4}SiO_4$	373	5.0×10^{-6}		[28] Fig. 2	
	$Li_{2.65}Al_{0.45}SiO_4$	373	3.0×10^{-7}		[28] Fig. 2	
	$Li_{2.5}Al_{0.5}SiO_4$	373	1.0×10^{-9}		[28] Fig. 2	
Li-Ga-Si-O	$Li_{4.2}Ga_{0.2}Si_{0.8}O_4$	373	5.0×10^{-7}		[28] Fig. 1	
		573	5.0×10^{-4}			
	$Li_{3.7}Ga_{0.1}SiO_4$	373	1.3×10^{-6}		[28] Fig. 2	
	$Li_{3.4}Ga_{0.2}SiO_4$	373	1.5×10^{-6}		[28] Fig. 2	
	$Li_{3.25}Ga_{0.25}SiO_4$	373	1.0×10^{-6}		[28] Fig. 2	
	$Li_{3.1}Ga_{0.3}SiO_4$	373	3.0×10^{-7}		[28] Fig. 2	
	$Li_{2.8}Ga_{0.4}SiO_4$	373	1.0×10^{-7}		[28] Fig. 2	
	$Li_{2.5}Ga_{0.5}SiO_4$	373	1.0×10^{-8}		[28] Fig. 2	
Li-Al-Ge-O	$Li_{3.7}Al_{0.1}GeO_4$	298	1.00×10^{-5}		[44] Fig. 1	
		373	2.00×10^{-4}			
		573	4.00×10^{-2}			
		773	1.78×10^{-1}			
		973	2.30×10^{-1}			
		1173	2.30×10^{-1}			
		303	3.16×10^{-6}	0.6	[45] Fig. 4	
		370	1.58×10^{-4}			
		435	1.58×10^{-3}			
		526	3.16×10^{-2}			
		573	3.50×10^{-2}		[45] Fig. 3	
		673	1.00×10^{-1}			

		773	1.70×10^{-1}	
		873	2.10×10^{-1}	
		1073	2.30×10^{-1}	
		1273	2.30×10^{-1}	
	$Li_{3.55}Al_{0.15}GeO_4$	573	2.50×10^{-2}	[46] Table 4
Li-Ga-Ge-O	$Li_{3.7}Ga_{0.1}GeO_4$	333	1.58×10^{-5}	[47] Fig. 4
		473	1.26×10^{-3}	
	$Li_{3.55}Ga_{0.15}GeO_4$	573	3.00×10^{-2}	[46] Table 4

Oxides, V-IV system

Compound		T (K)	σ (S cm^{-1})	E_a (eV)	Reference	ML
Li-P-Si-O	$Li_{3.75}P_{0.25}Si_{0.75}O_4$	298	4.8×10^{-7}		[41] Table 7	*
		473	1.0×10^{-3}			*
		573	1.0×10^{-2}			*
	$Li_{3.95}P_{0.05}Si_{0.95}O_4$	714	8.83×10^{-3}	0.724	[48]	
		333	4.75×10^{-8}			
	$Li_{3.91}P_{0.09}Si_{0.91}O_4$	625	3.19×10^{-3}	0.633	[48]	
		333	1.89×10^{-7}			
	$Li_{3.8}P_{0.2}Si_{0.8}O_4$	625	1.60×10^{-2}	0.594	[48]	
		333	2.38×10^{-6}			
	$Li_{3.7}P_{0.3}Si_{0.7}O_4$	625	3.19×10^{-2}	0.590	[48]	
		333	4.75×10^{-6}			
	$Li_{3.6}P_{0.4}Si_{0.6}O_4$	625	5.06×10^{-2}	0.533	[48]	
		333	1.50×10^{-5}			
	$Li_{3.5}P_{0.5}Si_{0.5}O_4$	625	1.01×10^{-1}	0.516	[48]	*
		333	2.38×10^{-5}			*
	$Li_{3.4}P_{0.6}Si_{0.4}O_4$	625	6.37×10^{-2}	0.507	[48]	
		333	1.89×10^{-5}			
	$Li_{3.2}P_{0.8}Si_{0.2}O_4$	625	1.27×10^{-2}	0.529	[48]	
		333	3.00×10^{-6}			
	$Li_{3.09}P_{0.91}Si_{0.09}O_4$	625	3.19×10^{-3}	0.546	[48]	
		333	5.99×10^{-7}			
	$Li_{3.06}P_{0.94}Si_{0.06}O_4$	625	1.01×10^{-3}	0.598	[48]	
		333	5.99×10^{-8}			
Li-V-Si-O	$Li_{3.9}V_{0.1}Si_{0.9}O_4$	333	2.00×10^{-7}	0.601	[49] Fig. 4	
		500	2.00×10^{-4}			
	$Li_{3.8}V_{0.2}Si_{0.8}O_4$	333	3.16×10^{-6}	0.529	[49] Fig. 4	
		500	1.26×10^{-3}			
	$Li_{3.6}V_{0.4}Si_{0.6}O_4$	333	2.00×10^{-5}	0.497	[49] Fig. 4	
		500	3.98×10^{-3}			

	$Li_{3.4}V_{0.6}Si_{0.4}O_4$	333	6.31×10^{-5}	0.435	[49] Fig. 4	
		500	1.00×10^{-2}			
	$Li_{3.2}V_{0.8}Si_{0.2}O_4$	333	2.00×10^{-5}	0.456	[49] Fig. 4	
		500	3.98×10^{-3}			
	$Li_{3.3}V_{0.7}Si_{0.3}O_4$	298	1.00×10^{-5}	0.36	[35]	
				(315-465 K)		
	$Li_{3.8}V_{0.2}Si_{0.8}O_4$	323	5.01×10^{-7}	0.50	[35] Fig. 1	
		373	6.31×10^{-6}			
		473	2.00×10^{-4}			
		573	2.00×10^{-3}			
	$Li_{3.6}V_{0.4}Si_{0.6}O_4$	323	7.94×10^{-6}	0.39	[35] Fig. 1	
		373	6.31×10^{-5}			
		473	1.00×10^{-3}			
		573	7.94×10^{-3}			
	$Li_{3.5}V_{0.5}Si_{0.5}O_4$	323	1.59×10^{-5}	0.37	[35] Fig. 1	
		373	1.00×10^{-4}			
		473	1.59×10^{-3}			
		573	1.00×10^{-2}			
	$Li_{3.4}V_{0.6}Si_{0.4}O_4$	323	2.00×10^{-5}	0.34	[35] Fig. 1	
		373	1.00×10^{-4}			
		473	1.26×10^{-3}			
		573	1.00×10^{-2}			
	$Li_{3.3}V_{0.7}Si_{0.3}O_4$	323	2.00×10^{-5}	0.36	[35] Fig. 1	
		373	6.31×10^{-5}			
		473	7.94×10^{-4}			
		573	6.31×10^{-3}			
	$Li_{3.2}V_{0.8}Si_{0.2}O_4$			0.32	[35] Fig. 1	
	$Li_{3.1}V_{0.9}Si_{0.1}O_4$			0.50	[35] Fig. 1	
Li-As-Si-O	$Li_{3.9}As_{0.1}Si_{0.9}O_4$	294	7.94×10^{-9}	0.622	[33] Fig. 5,7	
		573	1.00×10^{-3}			
	$Li_{3.8}As_{0.2}Si_{0.8}O_4$	294	2.00×10^{-7}	0.549	[33] Fig. 5,7	
		573	6.31×10^{-3}			
	$Li_{3.6}As_{0.4}Si_{0.6}O_4$	294	2.00×10^{-6}	0.487	[33] Fig. 5,7	*
		573	1.58×10^{-2}			*
	$Li_{3.4}As_{0.6}Si_{0.4}O_4$	294	1.58×10^{-6}	0.466	[33] Fig. 5,7	
		573	1.26×10^{-2}			
	$Li_{3.2}As_{0.8}Si_{0.2}O_4$	294	1.26×10^{-6}	0.446	[33] Fig. 5,7	
		573	1.00×10^{-2}			
	$Li_{3.1}As_{0.9}Si_{0.1}O_4$	294	1.00×10^{-7}	0.497	[33] Fig. 5,7	
		573	1.26×10^{-3}			
Li-P-Ge-O	$Li_{3.75}P_{0.25}Ge_{0.75}O_4$	189	2.11×10^{-10}	0.529	[50] Fig. 4,9,14	*

		211	3.77×10^{-9}			*
		227	3.50×10^{-8}			*
		250	5.04×10^{-7}			*
		270	2.33×10^{-6}			*
		300	2.00×10^{-5}			*
	$Li_{3.5}P_{0.5}Ge_{0.5}O_4$	189	1.06×10^{-10}	0.513	[50] Fig. 4,9,14	*
		211	2.38×10^{-9}			*
		227	1.39×10^{-8}			*
		250	2.52×10^{-7}			*
		270	1.17×10^{-6}			*
		300	8.00×10^{-6}			*
	$Li_{3.25}P_{0.75}Ge_{0.25}O_4$	189	6.67×10^{-11}	0.529	[50] Fig. 4,9,14	*
		211	9.48×10^{-10}			*
		227	6.97×10^{-9}			*
		250	7.98×10^{-8}			*
		270	3.70×10^{-7}			*
		300	2.00×10^{-6}			*
	$Li_{3.75}P_{0.25}Ge_{0.75}O_4$	573	6.92×10^{-2}	0.425 (low-temp.)	[51] Fig. 3	*
		623	1.20×10^{-1}	0.290 (high-temp.)		*
		673	2.04×10^{-1}			*
		723	3.24×10^{-1}			*
		773	4.79×10^{-1}			*
		823	6.46×10^{-1}			*
		873	8.13×10^{-1}			*
		923	9.55×10^{-1}			*
		973	1.10			*
Li-V-Ge-O	$Li_{3.75}V_{0.25}Ge_{0.25}O_4$	300	6.00×10^{-6}	0.549	[50] Fig. 11,14	
	$Li_{3.6}V_{0.4}Ge_{0.6}O_4$	189	1.33×10^{-9}		[50] Fig. 6	
		211	1.50×10^{-8}			
		227	8.78×10^{-8}			
		250	1.00×10^{-6}			
		270	5.86×10^{-6}			
	$Li_{3.5}V_{0.5}Ge_{0.5}O_4$	189	2.66×10^{-9}	0.425	[50] Fig. 6,11,14	
		211	3.77×10^{-8}			
		227	2.78×10^{-7}			
		250	1.59×10^{-6}			
		300	3.00×10^{-5}			
	$Li_{3.4}V_{0.6}Ge_{0.4}O_4$	189	3.34×10^{-9}	0.415	[50] Fig. 6,11,14	
		211	4.75×10^{-8}			

		227	3.50×10^{-7}			
		250	2.00×10^{-6}			
		270	9.29×10^{-6}			
		300	4.00×10^{-5}			
	$Li_{3.2}V_{0.8}Ge_{0.2}O_4$	189	8.40×10^{-10}	0.420	[50] Fig. 6,11,14	
		211	9.48×10^{-9}			
		227	6.97×10^{-8}			
		250	4.00×10^{-7}			
		270	2.33×10^{-6}			
		300	1.30×10^{-5}			
	$Li_{3.5}V_{0.5}Ge_{0.5}O_4$	286	2.78×10^{-5}		[5] Fig. 5	
		317	7.91×10^{-5}			
		345	2.90×10^{-4}			
		377	1.05×10^{-3}			
		417	3.80×10^{-3}			
		476	1.05×10^{-2}			
		571	5.53×10^{-2}			
	$Li_{3.75}V_{0.25}Ge_{0.25}O_4$	298	6.31×10^{-6}		[52] Fig. 4	
		373	3.16×10^{-4}			
		473	1.00×10^{-2}			
		573	1.00×10^{-1}			
		673	3.98×10^{-1}			
		773	7.94×10^{-1}			
		873	1.00			
		973	1.26			
	$Li_{3.75}V_{0.25}Ge_{0.25}O_4$	291	1.00×10^{-5}		[53] Fig. 5	
		463	1.26×10^{-2}			
	$Li_{3.6}V_{0.4}Ge_{0.6}O_4$	291	1.00×10^{-5}	0.44	[53] Fig. 5	
		463	1.26×10^{-2}			
	$Li_{3.5}V_{0.5}Ge_{0.5}O_4$	291	6.31×10^{-6}		[53] Fig. 5	
		463	1.26×10^{-2}			
	$Li_{3.33}V_{0.67}Ge_{0.33}O_4$	291	3.98×10^{-6}		[53] Fig. 5	
		463	3.16×10^{-3}			
Li-As-Ge-O	$Li_{3.7}As_{0.3}Ge_{0.7}O_4$	300	1.60×10^{-5}	0.529	[50] Fig. 10,14	
	$Li_{3.6}As_{0.4}Ge_{0.6}O_4$	189	1.33×10^{-9}	0.472	[50] Fig. 5,10,14	
		211	1.89×10^{-8}			
		227	1.39×10^{-7}			
		250	1.26×10^{-6}			
		270	5.86×10^{-6}			
		300	4.00×10^{-5}			*
	$Li_{3.4}As_{0.6}Ge_{0.4}O_4$	300	2.00×10^{-5}	0.456	[50] Fig. 10,14	*

	$Li_{3.3}As_{0.7}Ge_{0.3}O_4$	300	1.30×10^{-5}	0.456	[50] Fig. 10,14
	$Li_{3.2}As_{0.8}Ge_{0.2}O_4$	300	4.00×10^{-6}	0.456	[50] Fig. 10,14
Li-V-Ti-O	$Li_{3.75}V_{0.25}Ti_{0.75}O_4$	300	3.00×10^{-6}	0.456	[50] Fig. 13,14
	$Li_{3.6}V_{0.4}Ti_{0.6}O_4$	300	1.60×10^{-5}	0.461	[50] Fig. 13,14
	$Li_{3.5}V_{0.5}Ti_{0.5}O_4$	189	4.21×10^{-9}	0.435	[50] Fig. 8,13,14
		211	4.75×10^{-8}		
		227	2.78×10^{-7}		
		250	2.00×10^{-6}		
		270	1.17×10^{-5}		
		300	4.00×10^{-5}		
	$Li_{3.4}V_{0.6}Ti_{0.4}O_4$	300	1.60×10^{-5}	0.430	[50] Fig. 13,14
	$Li_{3.25}V_{0.75}Ti_{0.25}O_4$	300	1.00×10^{-5}	0.415	[50] Fig. 13,14
Li-As-Ti-O	$Li_{3.75}As_{0.25}Ti_{0.75}O_4$	211	9.48×10^{-9}	0.461	[50] Fig. 3,12,14
		227	6.97×10^{-8}		
		250	5.04×10^{-7}		
		270	3.70×10^{-6}		
		300	2.00×10^{-5}		
	$Li_{3.6}As_{0.4}Ti_{0.6}O_4$	189	1.68×10^{-9}	0.461	[50] Fig. 7,12,14
		211	2.38×10^{-8}		
		227	1.39×10^{-7}		
		250	1.00×10^{-6}		
		270	5.86×10^{-6}		
		300	3.00×10^{-5}		
	$Li_{3.4}As_{0.6}Ti_{0.4}O_4$	300	3.00×10^{-5}	0.461	[50] Fig. 12,14
	$Li_{3.25}As_{0.75}Ti_{0.25}O_4$	300	5.00×10^{-6}	0.440	[50] Fig. 12,14

Sulfides

Compound		T (K)	σ (S cm^{-1})	E_a (eV)	Reference	ML
Li-Al-S	Li_5AlS_4	298	3.16×10^{-9}		[74] Fig. 9	
Li-Ga-S	Li_5GaS_4	373	5.10×10^{-8}		[18] Table 1	
Li-Si-S	Li_4SiS_4	298	1.26×10^{-8}		[74] Fig. 9	
Li-Ge-S	Li_4GeS_4	298	2.00×10^{-7}	0.529	[18]	
		323	1.00×10^{-6}		Table 1, Fig. 5	
		345	3.98×10^{-6}			
		400	5.01×10^{-5}			
		476	5.01×10^{-4}			
		526	1.58×10^{-3}			
		588	3.98×10^{-3}			
Li-P-S	Li_3PS_4	298	3.16×10^{-7}		[74] Fig. 9	
		373	1.00×10^{-5}	0.49	[75] Fig. 5	

		400	2.51×10^{-5}	(T < 463 K)	
		444	1.00×10^{-4}	0.46	
		473	7.94×10^{-4}	(T > 463 K)	
		573	5.01×10^{-3}		
		298	3.00×10^{-7}		[76] Fig. 3
		357	1.00×10^{-6}		
		417	1.26×10^{-5}		
		465	5.01×10^{-5}		
		556	1.58×10^{-3}		
		667	5.01×10^{-3}		
	$Li_{3.325}P_{0.935}S_4$	300	1.50×10^{-4}	0.228	[74] Fig. 6
		373	2.51×10^{-3}		
		473	1.00×10^{-2}		
	$Li_4P_{0.8}S_4$	298	1.26×10^{-6}		[74] Fig. 9
Li-Zn-Ge-S	$Li_{3.6}Zn_{0.2}GeS_4$	298	6.31×10^{-8}		[74] Fig. 9
	$Li_{3.8}Zn_{0.1}GeS_4$	298	1.00×10^{-7}		[74] Fig. 9
	$Li_{3.9}Zn_{0.05}GeS_4$	298	2.51×10^{-7}		[74] Fig. 9
		373	2.00×10^{-5}		[18] Fig. 5
		473	7.94×10^{-4}		
		573	3.16×10^{-3}		
	Li_2ZnGeS_4	323	1.40×10^{-9}		[18] Table 1
Li-Al-Si-S	$Li_{4.2}Al_{0.2}Si_{0.8}S_4$	298	2.00×10^{-8}		[74] Fig. 9
	$Li_{4.4}Al_{0.4}Si_{0.6}S_4$	298	3.16×10^{-8}		[74] Fig. 9
	$Li_{4.6}Al_{0.6}Si_{0.4}S_4$	298	1.26×10^{-8}		[74] Fig. 9
	$Li_{4.8}Al_{0.8}Si_{0.2}S_4$	298	2.51×10^{-7}		[74] Fig. 9
		298	2.30×10^{-7}	0.521	[19] Fig. 11
		373	7.94×10^{-6}		
		473	3.16×10^{-4}		
Li-Ga-Ge-S	$Li_{4.2}Ga_{0.2}Ge_{0.8}S_4$	298	6.31×10^{-5}		[74] Fig. 9
	$Li_{4.25}Ga_{0.25}Ge_{0.75}S_4$	298	7.94×10^{-5}		[74] Fig. 9
	$Li_{4.3}Ga_{0.3}Ge_{0.7}S_4$	298	3.16×10^{-5}		[74] Fig. 9
	$Li_{4.4}Ga_{0.4}Ge_{0.6}S_4$	298	5.01×10^{-6}		[74] Fig. 9
	$Li_{4.5}Ga_{0.5}Ge_{0.5}S_4$	298	5.01×10^{-7}		[74] Fig. 9
	$Li_{4.25}Ga_{0.25}Ge_{0.75}S_4$	298	6.31×10^{-5}		[18] Fig. 5
		373	1.00×10^{-3}		
		473	5.01×10^{-3}		
		573	1.00×10^{-2}		
Li-P-Si-S	$Li_{3.2}P_{0.8}Si_{0.2}S_4$	298	3.16×10^{-6}		[74] Fig. 9
	$Li_{3.3}P_{0.7}Si_{0.3}S_4$	298	1.00×10^{-5}		[74] Fig. 9
	$Li_{3.4}P_{0.6}Si_{0.4}S_4$	298	6.31×10^{-4}		[74] Fig. 9
		300	6.40×10^{-4}	0.29	[19] Fig. 8

		373	6.31×10^{-3}		
		473	3.16×10^{-2}		
	$Li_{3.5}P_{0.5}Si_{0.5}S_4$	298	1.26×10^{-4}		[74] Fig. 9
	$Li_{3.6}P_{0.4}Si_{0.6}S_4$	298	6.31×10^{-5}		[74] Fig. 9
	$Li_{3.8}P_{0.2}Si_{0.8}S_4$	298	7.94×10^{-7}		[74] Fig. 9
Li-P-Ge-S	$Li_{3.2}P_{0.8}Ge_{0.2}S_4$	298	5.01×10^{-4}	0.269	[8] Fig. 4
		323	1.26×10^{-3}		
		364	3.98×10^{-3}		
		423	1.26×10^{-2}		
		473	3.16×10^{-2}		
		573	1.00×10^{-1}		
	$Li_{3.25}P_{0.75}Ge_{0.25}S_4$	298	2.00×10^{-3}	0.207	[8] Fig. 4
		323	5.01×10^{-3}		
		364	1.00×10^{-2}		
		423	3.16×10^{-2}		
		473	6.31×10^{-2}		
		573	1.26×10^{-1}		
	$Li_{3.3}P_{0.7}Ge_{0.3}S_4$	298	1.58×10^{-3}	0.218	[8] Fig. 4
		323	3.98×10^{-3}		
		364	7.94×10^{-3}		
		423	2.51×10^{-2}		
		473	5.01×10^{-2}		
		573	1.00×10^{-1}		
	$Li_{3.35}P_{0.65}Ge_{0.35}S_4$	298	1.26×10^{-3}	0.228	[8] Fig. 4
		323	3.98×10^{-3}		
		364	7.94×10^{-3}		
		423	2.51×10^{-2}		
		473	5.01×10^{-2}		
		573	1.00×10^{-1}		
	$Li_{3.4}P_{0.6}Ge_{0.4}S_4$	298	6.31×10^{-4}	0.269	[8] Fig. 4
		323	1.26×10^{-3}		
		364	3.98×10^{-3}		
		423	1.26×10^{-2}		
		473	3.16×10^{-2}		
		573	1.00×10^{-1}		
	$Li_{3.6}P_{0.4}Ge_{0.6}S_4$	298	1.58×10^{-4}	0.342	[8] Fig. 4
		323	5.01×10^{-4}		
		364	1.58×10^{-3}		
		423	7.94×10^{-3}		
		473	2.00×10^{-2}		
		573	7.94×10^{-2}		

$Li_{3.8}P_{0.2}Ge_{0.8}S_4$	298	2.51×10^{-6}	0.466	[8] Fig. 4
	323	1.00×10^{-5}		
	364	6.31×10^{-5}		
	423	3.98×10^{-4}		
	473	1.58×10^{-3}		
	573	1.26×10^{-2}		

Table 1.2. Crystallographic data for LISICON-type compounds.

Oxides

Compound	Structure	*Z*	Crystal system	Space group (S.G.number)	Temperature	Reference
Li_6ZnO_4	AF	2	tetragonal	*P*4$_2$/*nmc* (137)		[54]
Li_5AlO_4	AF	2	orthorhombic	*Pmmn* (59)		[55]
Li_5GaO_4	AF	8	orthorhombic	*Pbca* (61)	low temp.	[56]
Li_4GeO_4	α	4	orthorhombic	*Bmmb* (63)		[57]
Li_4SiO_4	α	2	monoclinic	*P*2$_1$/*m* (11)		[58]
Li_4TiO_4	α	4	orthorhombic	*Cmcm* (63)		[59]
Li_3PO_4	β	2	orthorhombic	*Pmn*2$_1$ (31)	*T* < 775 K	[60]
	γ	4	orthorhombic	*Pmnb* (62)	*T* > 775 K	[61]
Li_3AsO_4	β	2	orthorhombic	*Pmn*2$_1$ (31)	low temp.	[62]
Li_2ZnGeO_4	β	2	monoclinic	*Pn* (7)		[63]
$Li_{3.5}Zn_{0.25}GeO_4$	γ	4	orthorhombic	*Pnma* (62)		[4]
	γ	4	orthorhombic	*Pnma* (62)		[24]
$Li_3Zn_{0.5}GeO_4$	γ	4	orthorhombic	*Pnma* (62)		[64]
	γ	4	orthorhombic	*Pnma* (62)		[25]
$Li_{3.05}P_{0.69}Ge_{0.31}O_4$	γ	4	orthorhombic	*Pnma* (62)		[65]
$Li_{3.75}V_{0.25}Ge_{0.75}O_4$	γ	4	orthorhombic	*Pnma* (62)	298 K	[52]
$Li_{3.5}V_{0.5}Ge_{0.5}O_4$	γ	4	orthorhombic	*Pnma* (62)	298 K	[66]
$Li_{3.26}Ga_{0.2}SiO_4$	α	2	monoclinic	*P*2$_1$/*m* (11)		[67]
$Li_{2.82}Ga_{0.33}SiO_4$	α	4	orthorhombic	*C*222$_1$ (20)		[68]
$Li_{3.75}P_{0.25}Si_{0.75}O_4$	α	2	monoclinic	*P*2$_1$/*m* (11)		[69]

Sulfides

Compound	Structure	*Z*	Crystal system	Space group (S.G.number)	Temperature	Reference
Li_4GeS_4	γ	4	orthorhombic	*Pnma* (62)		[18]
	γ	4	orthorhombic	*Pnma* (62)		[77]
Li_4SiS_4	α	2	monoclinic	*P*2$_1$/*m* (11)		[19]
Li_3PS_4	β	2	orthorhombic	*Pmn*2$_1$ (31)	297 K	[76]
	γ	4	orthorhombic	*Pnma* (62)	637 K	[76]

1. 3. Overview of Each Chapter

This thesis consists of five chapters. The overview of each chapter is described as follows.

In Chapter 2, a series of cation spatial configurations in a γ-unit cell size for classical Li-ion conductors Li_4GeO_4 and $Li_3Zn_{0.5}GeO_4$ were systematically evaluated using first-principles calculations. Based on these calculations, energy stability of Li-ion sites is discussed. Energy of a Li-ion site depends heavily on its chemical environments. The most stable configurations of Li_4GeO_4 and $Li_3Zn_{0.5}GeO_4$ were obtained from the structural patterns based on α and γ structures, respectively. They were consistent with experimental diffraction data. In Li_4GeO_4, the most stable configuration has extremely lower energy than other ones, while in $Li_3Zn_{0.5}GeO_4$, there are many configurations energetically close to the most stable one. These energy distributions imply that $Li_3Zn_{0.5}GeO_4$ prefers a Li-ion disordered structure than Li_4GeO_4 does.

In Chapter 3, ionic behaviors in $Li_{2+2x}Zn_{1-x}GeO_4$, $Li_{3+x}Ge_xP_{1-x}O_4$ and $Li_{3+x}Ge_xP_{1-x}S_4$ with γ-LISICON structure were simulated using the first-principles molecular dynamics (FPMD) method. The FPMD simulations were performed only at the temperatures over 800 K because of the limit of computational time, but extrapolation of calculated diffusion coefficients to lower temperatures approximately fit with the experimental ones. Sulfides exhibit higher calculated diffusion coefficients by about one order of magnitude than oxides. Moreover, the FPMD simulations as well as the transition state search simulations showed that Li ions in oxides mainly diffuse by the cooperative mechanism involving a pair of two Li ions at an octahedral site and a neighboring tetrahedral site. On the other hand, in the case of sulfides, a single Li ion can move between a tetrahedral site and a neighboring octahedral site by itself in addition to the cooperative mechanism. We infer that occurrence of both mechanisms leads to higher conductivities in sulfides.

In Chapter 4, we aimed to establish the method to design superior ionic conductor at operating temperatures. Some ionic conductors show a deflection point in ionic conductivity corresponding to phase transition. In such cases, the above-mentioned simple extrapolation of the calculated data is inappropriate. We first estimated the phase transition temperature using first-principles calculations based on the cluster expansion method. However, the theoretical data alone are not sufficient to estimate low-temperature ionic conductivity. We proposed a

machine-learning technique to use the theoretical data and the experimental conductivity data in combination. This technique was used to predict ionic conductivities at 373 K for 72 compositions of LISICON-type oxides.

In Chapter 5, important conclusions obtained through our investigations are summarized.

References

[1] A. D. Robertson, A. R. West and A. G. Ritchie, *Solid State Ionics* **104** (1997) 1-11.

[2] P. Knauth, *Solid State Ionics* **180** (2009) 911-916.

[3] J. W. Fergus, *J. Power Sources* **195** (2010) 4554-4569.

[4] H. Y-P. Hong, *Mat. Res. Bull.* **13** (1978) 117-124.

[5] P. G. Bruce and I. Abrahams, *J. Solid State Chem.* **95** (1991) 74-82.

[6] Y. Inaguma, L. Chen, M. Itoh and T. Nakamura, *Solid State Ionics* **70/71** (1994) 196-202.

[7] R. Murugan V. Thangadurai and W. Weppner, *Angew. Chem. Int. Ed.* **46** (2007) 7778-7781.

[8] R. Kanno and M. Murayama, *J. Electrochem. Soc.* **148** (2001) A742-A746.

[9] A. Hayashi, K. Minami, F. Mizuno and M. Tatsumisago, *J. Mater. Sci.* **43** (2008) 1885-1889.

[10] N. Kamaya, K. Homma, Y. Yamakawa, M. Hirayama, R. Kanno, M. Yonemura, T. Kamiyama, Y. Kato, S. Hama, K. Kawamoto and A. Mitsui, *Nat. Mater.* **10** (2011) 682–686.

[11] U. V. Alpen, A. Rabenau and G. H. Talat, *Appl. Phys. Lett.* **30** (1977) 621-623.

[12] P. E. Stallworth, J. J. Fontanella, M. C. Wintersgill, C. D. Scheidler, J. J. Immel, S. G. Greenbaum and A. S. Gozdz, *J. Power Sources* **81** (1999) 739-747.

[13] P. G. Bruce and A. R. West, *Mat. Res. Bull.* **15** (1980) 379-385.

[14] H. Aono, E. Sugimoto, Y. Sadaoka, N. Imanaka and G. Adachi, *J. Electrochem. Soc.* **136** (1989) 590-591.

[15] K. Arbi, J. M. Rojo, J. Sanz, *J. Eur. Ceram. Soc.* **27** (2007) 4215-4218.

[16] Y. Inaguma, C. Liquan, M. Itoh, T. Nakamura, T. Uchida, H. Ikuta and M. Wakihara, *Solid State Commun.* **86** (1993) 689-693.

[17] Y. Harada, T. Ishigaki, H. Kawai and J. Kuwano, *Solid State Ionics* **108** (1998) 407-413.

[18] R. Kanno, T. Hata, Y. Kawamoto and M. Irie, *Solid State Ionics* **130** (2000) 97-104.

[19] M. Murayama, R. Kanno, M. Irie, S. Ito, T. Hata, N. Sonoyama and Y. Kawamoto, *J. Solid State Chem.* **168** (2002) 140-148.

[20] M. Tatsumisago, F. Mizuno and A. Hayashi, *J. Power Sources* **159** (2006) 193-199.

[21] T. Minami, A. Hayashi and M. Tatsumisago, *Solid State Ionics* **177** (2006) 2715-2720.

[22] K. Minami, A. Hayashi, S. Ujiie and M. Tatsumisago, *J. Power Sources* **189** (2009) 651-654.

[23] A. R. West, *Basic Solid State Chemistry*, 2nd ed., Chap. 7.5, John Wiley & Sons, Chichester, U.K. (1999).

[24] I. Abrahams, P. G. Bruce, A. R. West and W. I. F. David, *J. Solid State Chem.* **75** (1988) 390-396.

[25] I. Abrahams, P. G. Bruce, I. F. David and A. R. West, *Acta Cryst.* **B45** (1989) 457-462.

[26] R. A. Huggins, *Electrochim. Acta* **22** (1977) 773-781.

[27] T. Esaka and M. Greenblatt, *Solid State Ionics* **21** (1986) 255-261.

[28] V. Thangadurai and W. Weppner, *Ionics* **8** (2002) 281-292.

[29] Y. Saito, T. Asai, K. Ado, H. Kageyama and O. Nakamura, *Solid State Ionics* **40/41** (1990) 34-37.

[30] M. Wakihara, T. Uchida and T. Gohara, *Solid State Ionics* **31** (1988) 17-20.

[31] A. R. West, *J. Appl. Electrochem.* **3** (1973) 327-335.

[32] B. E. Liebert and R. A. Huggins, *Mat. Res. Bull.* **11** (1976) 533-538.

[33] A. Khorassani and A. R. West, *Solid State Ionics* **7** (1982) 1-8.

[34] M. A. K. L. Dissanayake, R. P. Gunawardane, H. H. Sumathipala and A. R. West, *Solid State Ionics* **76** (1995) 215-210.

[35] C. Li-quan, W. Lian-zhong, C. Guang-can, W. Gang and L. Zi-rong, *Solid State Ionics* **9/10** (1983) 149-152.

[36] G. Jasinski, P. Jasinski, B. Chachulski and A. Nowakowski, *Mater. Sci. Poland* **24** (2006) 261-268.

[37] D. Mazumdar, D. N. Bose and M. L. Mukherjee, *Solid State Ionics* **14** (1984) 143-147.

[38] U. V. Alpen, M. F. Bell and W. Wichelhaus, *Electrochim. Acta* **23** (1978) 1395-1397.

[39] P. G. Bruce and A. R. West, *J. Solid State Chem.* **44** (1982) 354-365.

[40] K. Jackowska and A. R. West, *J. Appl. Electrochem.* **15** (1985) 459-468.

[41] R. D. Shannon, B. E. Taylor, A. D. English and T. Berzins, *Electrochim. Acta* **22** (1977) 783-796.

[42] B. J. Neudecker and W. Weppner, *J. Electrochem. Soc.* **143** (1996) 2198-2203.

[43] A. Garcia, G. Torres-Trevino and A. R. West, *Solid State Ionics* **40/41** (1990) 13-17.

[44] C. K. Lee and A. R. West, *J. Mater. Chem.* **1** (1991) 149-150.

[45] C. K. Lee and A. R. West, *J. Mater. Chem.* **3** (1993) 191-196.

[46] A. K. Ivanov-Shits and S. E. Sigaryov, *Solid State Ionics* **27** (1988) 89-100.

[47] A. Robertson and A. R. West, *Solid State Ionics* **58** (1992) 351-358.

[48] Y-W. Hu, I. D. Raistrick and R. A. Huggins, *J. Electrochem. Soc.* **124** (1977) 1240-1242.

[49] A. Khorassani and A. R. West, *J. Solid State Chem.* **53** (1984) 369-375.

[50] A. R. Rodger, J. Kuwano and A. R. West, *Solid State Ionics* **15** (1985) 185-198.

[51] E. I. Burmakin and G. Sh. Shekhtman, *Russ. J. Electrochem.* **46** (2010) 243-246.

[52] E. I. Burmakin, V. I. Voronin and G. Sh. Shekhtman, *Russ. J. Electrochem.* **39** (2003) 1124-1129.

[53] J. Kuwano and A. R. West, *Mat. Res. Bull.* **15** (1980) 1661-1667.

[54] H. Untenecker and R. Hoppe, *Z. anorg. allg. Chem.* **551** (1987) 147-150.

[55] V. F. Stewner and R. Hoppe, *Z. anorg. allg. Chem.* **381** (1971) 149-160.

[56] V. F. Stewner and R. Hoppe, *Acta Cryst.* **B27** (1971) 616-621.

[57] H. Völlenkle and A. Wittmann, *Naturwissensch.* **54** (1967) 441.

[58] H. Völlenkle, A. Wittmann and H. Nowotny, *Monatsh. Chem.* **99** (1968) 1360-1371.

[59] R. P. Gunawardane, J. G. Fletcher, M. A. K. L. Dissanayake, R. A. Howie and A. R. West, *J. Solid State Chem.* **112** (1994) 70-72.

[60] C. Keffer, A. Mighell, F. Mauer, H. Swanson and S. Block, *Inorg. Chem.* **6** (1967) 119-125.

[61] J. Zemann, *Acta Cryst.* **13** (1960) 863-867.

[62] A. Elfakir, G. Wallez, M. Quarton and J. Pannetier, *Phase Transition* **45** (1993) 281-288.

[63] E. Plattner, H. Völlenkle and A. Wittmann, *Monatsh. Chem.* **107** (1976) 921-927.

[64] E. Plattner and H. Völlenkle, *Monatsh. Chem.* **110** (1979) 693-698.

[65] M. Kh. Rabadanov, A. Pietraszko, V. V. Kirrev, A. K. Ivanov-Schitz and V. I. Simonov, *Crystallogr. Rep.* **48** (2003) 744-749.

[66] I. Abrahams and P. G. Bruce, *Acta Cryst.* **B47** (1991) 696-701.

[67] R. I. Smith and A. R. West, *J. Solid State Chem.* **88** (1990) 564-570.

[68] R. I. Smith and A. R. West, *J. Mater. Chem.* **1** (1991) 91-96.

[69] W. H. Baur and T. Ohta, *J. Solid State Chem.* **44** (1982) 50-59.

[70] A. R. West and F. P. Glasser, *J. Mater. Sci.* **5** (1970) 557-565.

[71] A. R. West and F. P. Glasser, *J. Mater. Sci.* **6** (1971) 1100-1110.

[72] P. Quintana and A. R. West, *J. Solid State Chem.* **81** (1989) 257-270.

[73] A. Khorassani, G. Izquierdo, and A. R. West, *Mater. Res. Bull.* **16** (1981) 1561-1567.

[74] M. Murayama, N. Sonoyama, A. Yamada and R. Kanno, *Solid State Ionics* **170** (2004) 173-180.

[75] M. Tachez, J.-P. Malugani, R. Mercier and G. Robert, *Solid State Ionics* **14** (1984) 181-185.

[76] K. Homma, M. Yonemura, T. Kobayashi, M. Nagao, M. Hirayama and R. Kanno, *Solid State Ionics* **182** (2011) 53-58.

[77] M. Murayama, R. Kanno, Y. Kawamoto and T. Kamiyama, *Solid State Ionics* **154/155** (2002) 789-794.

Chapter 2

Variation of Cation Configurations in LISICON-Type Oxides by First-Principles Calculations

2. 1. Introduction

Toward development of next-generation all-solid-state Li-ion rechargeable batteries, it is essential to further improve ionic conductivities of inorganic solid electrolytes. According to the previous experimental researches, ionic conductivities depend markedly on their composition, constituent elements and crystal structure. We focused on LISICON-type oxides as a typical case.

LISICON is the formula $Li_{3.5}Zn_{0.25}GeO_4$ and a member of a solid solution system of $Li_{2+2x}Zn_{1-x}GeO_4$ ($0 \leq x \leq 1$). The ionic conductivity of Li_2ZnGeO_4 ($x = 0$) is very low. With increasing Li content, the conductivity increases. $Li_{2.5}Zn_{0.75}GeO_4$ ($x = 0.25$), $Li_3Zn_{0.5}GeO_4$ ($x = 0.5$), and $Li_{3.5}Zn_{0.25}GeO_4$ ($x = 0.75$) show ionic conductivities of 0.009, 0.059, and 0.210 S cm^{-1} at 400 °C, respectively [1]. In contrast, the conductivity of Li_4GeO_4 ($x = 1$) is lower than 1×10^{-4} S cm^{-1} at 400 °C [2]. The reason of the maximal conductivity at $x = 0.75$ cannot be simply explained only by the Li content. As shown in Figure 1.2, the ground state structures change from β to γ and then α phase with increasing x from 0 to 1. Differences between those structures are characterized by Ge-ion configurations. It was reported that $Li_3Zn_{0.5}GeO_4$ and $Li_{3.5}Zn_{0.25}GeO_4$ have γ structure and a part of the Li-ion sites exhibits partial occupancy at room temperatures [3,4]. On the other hand, Li_4GeO_4 shows α structure [5]. Li-ion sites are fully occupied at room temperatures. Partial occupancy has not been reported in Li_4GeO_4. Based on those trends, the structure and the partial occupation as well as the Li content are expected to have great influence on the ionic conductivities. However, relationship between those factors and ionic conductivities about $Li_{2+2x}Zn_{1-x}GeO_4$ has not been studied theoretically so far.

As mentioned in Section 1.1, one of the necessary conditions for high ionic conductivity is assumed to be mobile-ion disordering. This leads to partial occupation on mobile-ion sites. In other words, mobile ions can have many sites in similar energy states. Therefore, in order to evaluate

mobile-ion disordering, it is important to calculate energy states of the mobile-ion sites. In this study, total energies of various cation configurations with α, β and γ structures for Li_4GeO_4 and $Li_3Zn_{0.5}GeO_4$ were systematically calculated. From the result, first, stable configurations were identified and local environments of the cations were analyzed. Then, based on the energy distribution dependence on those configurations, ionic conduction properties of Li_4GeO_4 and $Li_3Zn_{0.5}GeO_4$ were quantitatively discussed.

2. 2. Structures and Computational Models

According to reported diffraction data, the structure of α-Li_4GeO_4 is orthorhombic with a space group *Bmmb* (No.63) [5]. Although Li_4GeO_4 has excess Li ions based on the ratio of the number of cations to that of oxide ions, all Li ions have tetrahedral coordination and interstitial sites with octahedral coordination are not occupied. Volume of a conventional cell of α-Li_4GeO_4 is about twice as large as that of a primitive cell of α structure as shown in Figure 1.3(a) [6]. The structure of γ-$Li_3Zn_{0.5}GeO_4$ is orthorhombic with a space group *Pmnb* (No.62) [4]. Li and Zn ions are disorderly located at the same tetrahedral sites. Zn ions preferentially occupy 8*d* of tetrahedral sites. Excess Li ions partially occupy two interstitial octahedral sites, 4*c* and 4*b*. The Li occupancies of 4*c* and 4*b* are 0.420 and 0.081 respectively.

Computational models containing four formula units with α, β and γ structures in Li_4GeO_4 were constructed for geometry relaxation. Fractional coordinates in a primitive cell of β and γ structures were provided as shown in Table 2.1 and 2.2. The initial structures were borrowed from β-Li_3PO_4 [7] and γ-Li_3PO_4 [8], respectively. Fractional coordinates of α structure were determined according to those of β structure. The computational model of α and β structures corresponds to a 1 × 2 × 1 supercell, while the model of γ structure corresponds to the unit cell. Four Ge ions are located at tetrahedral sites. The coordinates of two Ge ions in α structure are translated −1/4 along the *c* axis from those of β structure. Twelve Li ions occupy residual tetrahedral sites, Li(1) and Li(2). The directions of [LiO_4] apexes in α, β and γ structures were set the same as those of α-Li_4GeO_4, β-Li_3PO_4 and γ-Li_3PO_4, respectively. Four excess Li ions partially occupy interstitial octahedral sites.

As shown in Table 2.1 and 2.2, the distinct octahedral sites of β and γ structures have different positional relationship with [GeO_4] tetrahedra. In α structure, coordination polyhedra of Li(3) sites have one edge sharing with [GeO_4], those of Li(4) sites have two edges sharing with [GeO_4], those of Li(5) sites have one face sharing with [GeO_4], and those of Li(6) sites have two faces sharing with [GeO_4]. A variety of cation configurations as initial structures for total energy calculations can be set. Since four excess Li ions partially occupy sixteen octahedral sites, the number of structural patterns is ${}_{16}C_4 = 1820$. It is possible to reduce the number of structural patterns of α, β and γ structures to 292, 272 and 292 by using symmetric operations in each space group, respectively. Although site symmetry is reduced from the original one depending on cation configuration, we keep the site label unchanged as in Table 2.1 and 2.2.

Computational models with α, β and γ structures in $Li_3Zn_{0.5}GeO_4$ were constructed in the same way as the models for Li_4GeO_4. Four Ge ions are located at tetrahedral sites. In the cell of γ structure, Zn ions were set to be located at only Zn(1) sites based on the measurement by Abrahams *et al* [4]. In the cell of α and β structures, Zn ions were set at only Zn(1) sites in consistent with that of γ structure. Moreover, two Zn ions are put at farthest sites in the cell because we assume that Zn ions prefer to be separated due to Coulomb repulsion forces between them. Ten Li ions occupy residual tetrahedral sites, Li(1) and Li(2). Since there are two excess Li ions in the cell, the number of structural patterns is ${}_{16}C_2 = 120$. Adopting symmetric operation, the number of structural patterns can be reduced to 64 for α, β and γ structures.

In this study, the initial directions of [LiO_4] apexes for geometry relaxation were fixed the same as those of structures reported experimentally. This means that only one of two face-sharing tetrahedral sites of a trigonal bipyramid was taken into account. However, Li-ion can move to the opposite site of a bipyramid, namely Li-ion disordering in a bipyramid. The fractional coordinate of this opposite site is shown in the parentheses of Table 2.1 and 2.2. We found that energy distribution against cation configurations without Li-ion disordering in the bipyramids is almost the same as that with the disordering by calculating energies of configurations for β-Li_4GeO_4. Therefore, Li-ion disordering in a bipyramid can be neglected in order to understand the relationship between cation configurations and energies. This verification is described in detail in Appendix (Section 2.6).

Table 2.1. Fractional coordinates in a primitive cell of β structure with a space group $Pmn2_1$. Ge, Li(1)/Zn(1) and Li(2)/Zn(2) are regular tetrahedral sites. Li(3), Li(4) and Li(5) are interstitial octahedral sites partially occupied by excess Li ions.

Site	W. L.	*x*	*y*	*z*	w. [GeO_4]**
O(1)	4*b*	0.20777	0.68676	0.8961	-
O(2)	2*a*	0	0.1052	0.9004	-
O(3)	2*a*	0.5	0.1814	0.8172	-
Ge	2*a*	0	0.82430	0	-
Li(1)/Zn(1)	4*b*	0.2481	0.3277	0.9860 (0.7360)*	-
Li(2)/Zn(2)	2*a*	0.5	0.8428	0.9893 (0.7393)*	-
Li(3)	2*a*	0	0.5	0.625	es × 1
Li(4)	2*a*	0	0.5	0.125	fs × 1
Li(5)	4*b*	0.25	0	0.125	es × 1, fs × 1

* The fractional coordinates of Li ions which tetrahedra have the opposite direction relative to the *c* axis according to β-Li_3PO_4 are shown in parentheses.
** "es" means the number of edges sharing the Li-ion octahedra with [GeO_4] tetrahedra. "fs" means the number of faces sharing the Li-ion octahedra with [GeO_4] tetrahedra.

Table 2.2. Fractional coordinates in a primitive cell of γ structure with a space group *Pmnb*. Ge, Li(1)/Zn(1) and Li(2)/Zn(2) are regular tetrahedral sites. Li(3), Li(4), Li(5) and Li(6) are interstitial octahedral sites partially occupied by excess Li ions.

Site	W. L.	*x*	*Y*	*z*	w. [GeO_4]
O(1)	8*d*	0.042	0.342	0.205	-
O(2)	4*c*	0.250	0.052	0.295	-
O(3)	4*c*	0.750	0.090	0.125	-
Ge	4*c*	0.250	0.4115	0.308	-
Li(1)/Zn(1)	8*d*	0.495	0.162	0.304 (0.054)*	-
Li(2)/Zn(2)	4*c*	0.750	0.422	0.196 (0.446)*	-
Li(3)	4*c*	0.25	0.25	0	es × 1
Li(4)	4*b*	0	0	0.5	es × 2
Li(5)	4*a*	0	0	0	fs × 2
Li(6)	4*c*	0.25	0.25	0.5	fs × 1

* The fractional coordinates of Li ions which tetrahedra have the opposite direction relative to the *c* axis according to γ-Li_3PO_4 are shown in parentheses.

2. 3. Computational Methods

First-principles calculations were performed using density functional theory [9,10] with the projector augmented wave (PAW) method [11] as implemented in the VASP code [12-14]. The form of the exchange-correlation term was taken to be the generalized gradient approximation (GGA) [15]. The plane-wave cutoff energies of 400 eV were employed. Computational models discussed in Section 2.2 in detail were adopted. Total energies of a series of Li-ion configurations were evaluated. The configurations of valence electrons are $1s^2\ 2s^1$ for Li, $3d^{10}\ 4s^2$ for Zn, $3d^{10}\ 4s^2\ 4p^2$ for Ge, $2s^2\ 2p^4$ for O. The radial cutoffs of the PAW potentials of Li, Zn, Ge and O are 2.05, 2.30, 2.30 and 1.85 Å, respectively. Numerical integration over the Brillouin zone was carried out by 4 × 2 × 4 k-point meshes. All internal positions and lattice constants were relaxed. The optimization procedure was truncated when the residual forces on the relaxed atoms became smaller than 0.02 eV / Å. The software VESTA [16] was used to visualize crystal structures.

2. 4. Results and Discussion

2. 4. 1. Cation Configurations for Li_4GeO_4

Total energies of 292, 272 and 292 cation configurations with α, β and γ structures for Li_4GeO_4 were evaluated using first-principles calculations. Relationship between volume and total energy is shown in Figure 2.3. Configurations are different among data points in the figure. Total energies are plotted as energy difference from the lowest energy configuration. The lowest energy configuration shows α structure. 50 of 292 initial configurations with α structure result in the lowest energy one. This most stable configuration in the present calculations is consistent with the experimental report on Li_4GeO_4 by Völlenkle *et al*. [5]. Energy difference between the most stable configuration and the second stable one is large, 0.56 eV per the computational cell ($Li_{16}Ge_4O_{16}$). The lowest energy configurations of β and γ structures have 1.46 and 0.87 eV per $Li_{16}Ge_4O_{16}$ higher than that of α structure. The energy distribution width for α, β and γ structures is 4.36, 1.76 and 3.27 eV per $Li_{16}Ge_4O_{16}$, respectively. There is a rough tendency that total energy increases with increasing volume. In an unfavorable configuration, cations repel each other, which may result in the

volume expansion.

In order to analyze the local environments of cations in the model, bond lengths between the cations and oxide ions of the lowest energy configuration were investigated. This result is summarized in Table 2.3. Four bond lengths for a cation at a regular tetrahedral site and six bond lengths for a cation at an interstitial octahedral site are shown. As shown in Table 2.3, cations in the three structures have similar local coordinations. Basically, Li and Ge ions at regular sites are tetrahedrally coordinated with oxide ions. Only Li(2) of β structure can be regarded as not 4-fold but 3-fold coordination. The bond lengths of Ge-O and Li-O are about 1.8 Å and 2.0 Å, respectively. Difference in the bond length is attributed to ionic radii of Li^{+} (0.59 Å) and Ge^{4+} (0.39 Å) [17]. Initially all of excess Li ions are located at ideal octahedral sites. In relaxed structures, distances between the excess Li ions and oxide ions can be divided into two types, shorter or longer than 2.2 Å. Coordination environment of the excess Li ions in the lowest energy configuration changes from octahedral to three or four-fold coordination through geometry optimization. Such coordination changes around excess Li ions are commonly found in all the three structures.

Excess Li ions in the lowest configuration of β and γ structures occupy the Li(3) sites which have an edge sharing with [GeO_4]. The reason is supposed to be that the repulsion between the Li ion and adjacent Ge ions are smaller. While, excess Li ions in the lowest configuration of α structure occupy the Li(5) sites which have a face sharing with [GeO_4]. In α structure, the relationship between excess Li ions and other adjacent Li ions are probably dominant. Local environments of excess Li ions are discussed in more detail for $Li_3Zn_{0.5}GeO_4$ in Section 2.4.2.

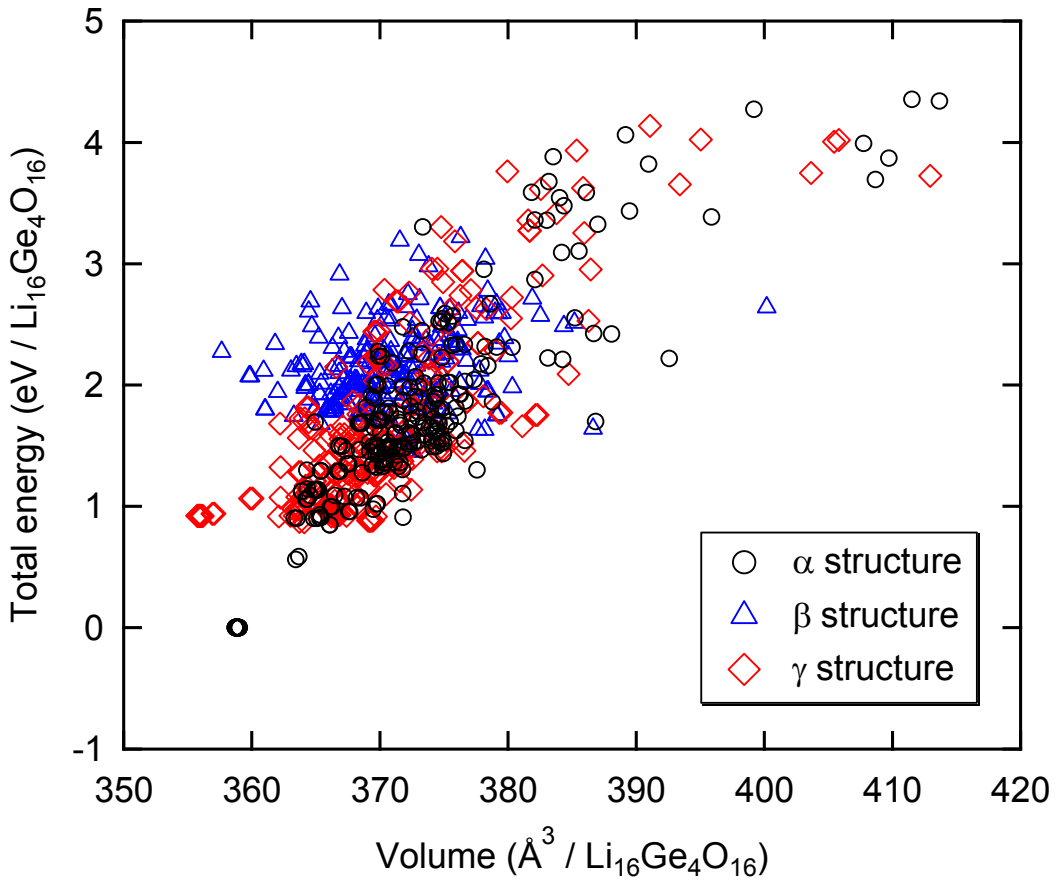

Figure 2.3. Relationship between volume and total energy of 292, 272 and 292 cation configurations with α, β and γ structures for Li_4GeO_4 evaluated using first-principles calculations.

Table 2.3. Bond lengths between cations and oxide ions of the lowest energy configuration with α, β and γ structures in Li_4GeO_4. n_a denotes the number of atoms in the computational cell.

α structure

Atom	n_a	Bond length (Å)
Ge	4	1.784, 1.784, 1.796, 1.796
Li(1)	8	1.927, 1.927, 1.978, 1.978
Li(2)	4	2.003, 2.026, 2.026, 2.138
Li(5)	4	2.007, 2.027, 2.027, 2.141, 3.148, 3.148

β structure

Atom	n_a	Bond length (Å)
Ge	4	1.781, 1.781, 1.788, 1.808
Li(1)	4	1.995, 2.023, 2.052, 2.120
	4	1.907, 1.972, 2.024, 2.139
Li(2)	4	1.877, 1.925, 1.957, (2.934), (3.136), 3.213
Li(3)	4	1.980, 1.983, 2.024, 2.075, 2.993, 3.018

A parenthesis means a distance to oxide ions those are not located at apexes of the nearest neighbor coordination polyhedron.

γ structure

Atom	n_a	Bond length (Å)
Ge	4	1.768, 1.791, 1.801, 1.808
Li(1)	2	1.892, 1.908, 2.007, 2.055
	2	1.896, 1.912, 1.996, 2.077
	2	1.925, 1.969, 1.993, 2.048
	2	1.927, 1.970, 1.987, 2.066
Li(2)	2	1.921, 1.977, 2.061, 2.166
	2	1.926, 1.985, 2.060, 2.096
Li(3)	2	1.914, 1.973, 2.017, 2.626, 2.887, 3.100
	2	1.920, 1.982, 2.020, 2.701, 2.796, 3.088

2. 4. 2. Cation Configurations for $Li_3Zn_{0.5}GeO_4$

Relationship between volume and total energy for $Li_3Zn_{0.5}GeO_4$ is shown in Figure 2.4. Unlike Li_4GeO_4, the lowest energy configuration was obtained from the structural patterns based on γ structure. This agrees with the experimental report [4]. The lowest energy configurations of α and β structures have 0.33 and 0.39 eV per $Li_{12}Zn_2Ge_4O_{16}$ higher than that of γ structure. The energy distribution widths of the three structures are similar. They are 1.48, 1.24 and 1.59 eV per $Li_{12}Zn_2Ge_4O_{16}$ for α, β and γ structures, respectively. β structure has the smallest volume, followed by γ and α. Turn to the opposite direction of [GeO_4] tetrahedra with reference to β phase results in increase of volume. Total energy tends to increase with increasing volume in all the three structures.

Bond lengths between cations and oxide ions of the lowest energy configuration with α, β and γ structures in $Li_3Zn_{0.5}GeO_4$ are summarized in Table 2.4. Bond lengths of Li-O and Ge-O in $Li_3Zn_{0.5}GeO_4$ are almost the same as those in Li_4GeO_4. Excess Li ions of $Li_3Zn_{0.5}ZnO_4$ prefer to have tetrahedral coordination in all the three structures. Bond lengths of Zn-O are nearly similar to those of Li-O. This is probably due to that ionic radius of Zn^{2+} (0.60 Å) is close to that of Li^+ (0.59 Å). Interstitial sites occupied by excess Li ions in the lowest energy configuration for $Li_3Zn_{0.5}GeO_4$ is also the same as those of Li_4GeO_4. Li(3) sites are occupied in β and γ structures, while Li(5) sites are occupied in α structure.

Based on initial structural patterns, energy difference between cation configurations is supposed to be attributed to chemical environments of excess Li ions at interstitial octahedral sites. The chemical environments include the geometrical relation between the excess Li ions and the neighboring Ge or Zn or Li ions. Figure 2.5 shows the interstitial sites occupied by excess Li ions of all configurations with γ, β and α structures. The vertical axis is total energy. The horizontal axis is average distance between excess Li ions and the neighboring Ge ions under the assumption that Coulomb repulsive force from high-valence Ge ions is predominant. In several cases, a Li ion at a regular tetrahedral site moves away to adjacent interstitial sites during optimization. Those configurations are not plotted.

In γ structure, the most stable site is Li(3) and the next stable one is Li(4). In contrast to α-Li_4GeO_4, there are a lot of configurations energetically close to the lowest energy one. Total

energy clearly increases when excess Li ions are located at Li(5) or Li(6) sites. In the neutron diffraction data of γ-$Li_3Zn_{0.5}GeO_4$ [4], Li-ion occupancies of Li(3) and Li(4) sites are 0.420 and 0.081, respectively. This experimental result suggests that Li(3) is energetically favorable site. Occupation at Li(5) and Li(6) sites have not been experimentally identified because they are unstable. Our calculations agree to experimental tendency of site occupation. On the other hand, the stable interstitial sites in β structure are in order of Li(3), Li(4) and Li(5). The stable interstitial sites in α structure are Li(5), Li(4), Li(3) and Li(6), in this order.

As shown in Figure 2.5(a), in the case of γ structure, energies of cation configurations are strongly correlated with distances between excess Li ions and the neighboring Ge ions. Distances between Li ions at the most stable site Li(3) and Ge ions are the longest, followed by Li(4), Li(6) and Li(5). This implies that Li ions diffuse via the sites relatively far from surrounding Ge ions in γ-$Li_3Zn_{0.5}GeO_4$. The correlation between Li-Ge distance and energy in β structure is smaller than that in γ structure. Moreover, the correlation in α structure is not clearly found. Therefore, it is difficult to attribute stability of interstitial sites to Li-Ge distance only in α structure. Spatial relationships with surrounding other cations are supposed to determine stability of interstitial sites. We found that Li(5) sites occupied by excess Li ions in the lowest energy configuration with α structure have four edges sharing with [LiO_4] tetrahedra and the distance between the excess Li ion and four adjacent Li ions is 2.550 Å. On the other hand, Li(3) sites occupied by excess Li ions in the highest energy configuration with α structure have four faces sharing with [LiO_4] tetrahedra. The distance between the excess Li ion and four adjacent Li ions is 2.230 Å. Longer distances between neighboring Li ions suppress repulsive Coulomb interaction and result in stable energy states in α structure.

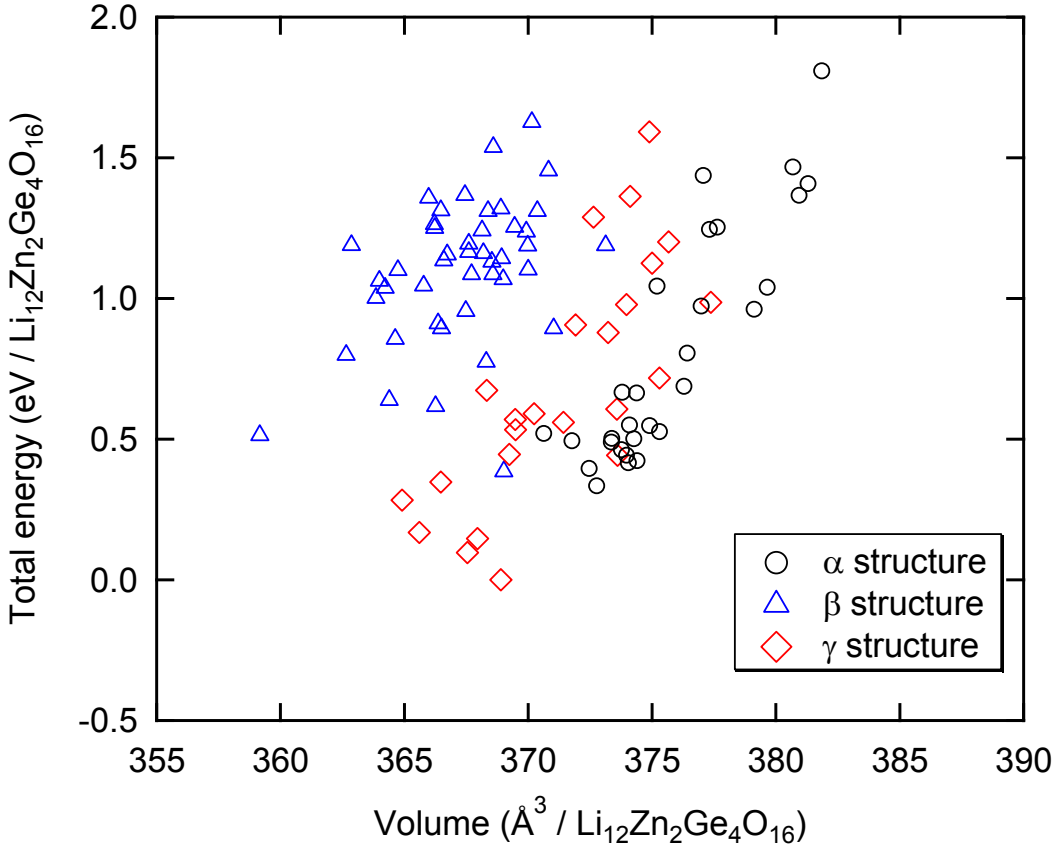

Figure 2.4. Relationship between volume and total energy of 64 cation configurations with α, β and γ structures for $Li_3Zn_{0.5}GeO_4$ evaluated using first-principles calculations.

Table 2.4. Bond lengths between cations and oxide ions of the lowest energy configuration with γ, β and α structures in $Li_3Zn_{0.5}GeO_4$. n_a denotes the number of atoms in the computational cell.

γ structure

Atom	n_a	Bond length (Å)
Ge	2	1.774, 1.777, 1.801, 1.807
	2	1.754, 1.786, 1.793, 1.817
Zn	2	1.948, 1.967, 1.972, 2.057
Li(1)	2	1.941, 1.980, 2.048, 2.111
	2	1.917, 2.010, 2.016, 2.026
	2	1.887, 1.964, 1.976, 2.117
Li(2)	2	1.932, 2.001, 2.088, 2.098
	2	1.957, 1.975, 2.021, 2.034
Li(3)	2	1.923, 2.003, 2.023, 2.422, 2.761, 3.183

β structure

Atom	n_a	Bond length (Å)
Ge	2	1.756, 1.789, 1.802, 1.811
	2	1.772, 1.778, 1.805, 1.806
Zn	2	1.969, 1.974, 1.991, 2.018
Li(1)	2	1.924, 1.971, 2.052, 2.109
	2	1.910, 2.010, 2.038, 2.042
	2	1.920, 1.953, 2.020, 2.064
Li(2)	2	1.960, 1.976, 1.981, 2.021
	2	1.957, 2.074, 2.086, 2.119
Li(3)	2	1.884, 1.983, 2.010, 2.453, 2.821, 3.073

α structure

Atom	n_a	Bond length (Å)
Ge	2	1.755, 1.789, 1.792, 1.803
	2	1.769, 1.781, 1.787, 1.815
Zn	2	1.952, 1.972, 1.976, 2.065
Li(1)	2	1.924, 1.938, 2.010, 2.020
	2	1.924, 1.991, 2.010, 2.089
	2	1.909, 1.979, 1.994, 2.067
Li(2)	2	1.999, 2.023, 2.031, 2.041
	2	1.931, 1.991, 2.005, 2.184
Li(5)	2	1.915, 1.981, 2.072, 2.569, 2.977, 3.002

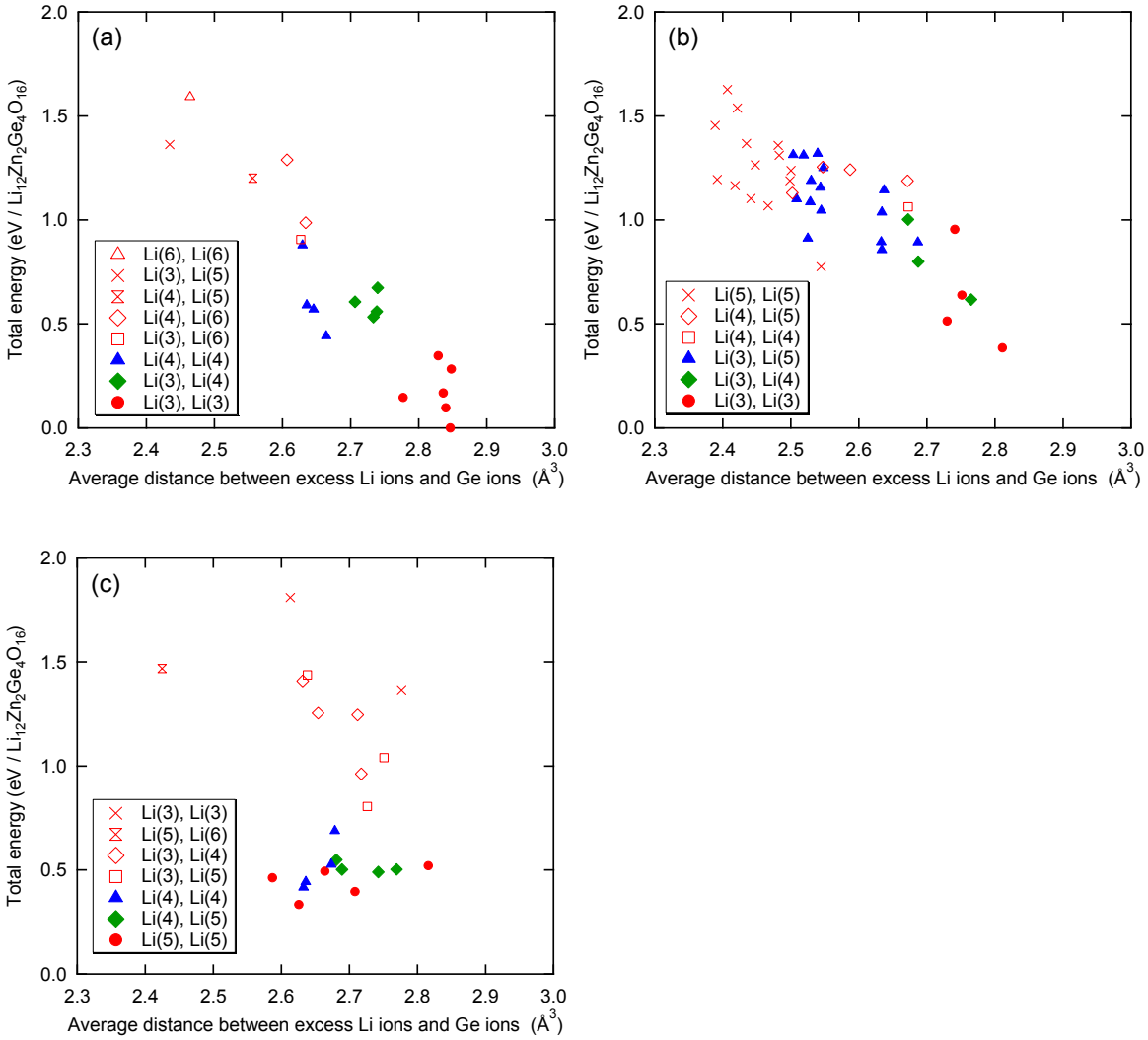

Figure 2.5. Total energy versus average distance between excess Li ions and the neighboring Ge ions in cation configurations with (a) γ, (b) β, (c) α structures for $Li_3Zn_{0.5}GeO_4$. Each configuration is classified according to the interstitial octahedral sites occupied by two excess Li ions.

2. 4. 3. Energy Change due to Ionic Jump

As mentioned in Section 2.4.1 and 2.4.2, energy distributions of cation configurations were determined using first-principles calculations. However, those data is unsatisfactory for the purpose of predicting ionic conductivity. Assuming that the ionic conductivity σ obey the Arrhenius equation $\sigma T = A\exp(-E_a/RT)$, where A, E_a, R and T are the pre-exponential factor, the activation energy, the gas constant and the absolute temperature, low E_a is required in order to exhibit high σ. The straight forward procedures to quantitatively estimate E_a are as follows: (i) A mobile-ion configuration as an initial state for an ionic jump is determined and its energy E_{ini} is calculated. (ii) Another mobile-ion configuration as an final state for the ionic jump is determined and its energy E_{fin} is calculated. Energy change ΔE due to the ionic jump is written as $\Delta E = E_{fin} - E_{ini}$. (iii) The minimum energy path for the ionic jump is determined by a transition state search algorithm such as the nudged elastic band (NEB) method [18]. E_a corresponds to the energy barrier of this path. This approach is a heavy task and thereby the detailed study will be discussed in Chapter 3. However, based on the energy distribution dependence on cation configurations, each configuration can be regarded as an initial or final state for ionic jump within the limit of the γ-unit cell size. Since low ΔE is essential to low E_a, it is possible to estimate the potential to exhibit good ionic conductivity to even compare ΔE.

The stable phases of Li_4GeO_4 and $Li_3Zn_{0.5}GeO_4$ show α and γ structures, respectively. In α-Li_4GeO_4, ΔE between the most stable configuration and the second stable one is 0.56 eV per $Li_{16}Ge_4O_{16}$. This value is quite larger than activation energies of typical superionic conductors. This large ΔE implies that Li_4GeO_4 has an ordered structure as the most stable configuration even at high temperatures. This is consistent with the experimental result that the conductivity of an end member Li_4GeO_4 is very low [2]. On the other hand, in γ-$Li_3Zn_{0.5}GeO_4$, there are a lot of configurations energetically close to the lowest energy one. In the six configurations within a higher energy range of 0.35 eV per $Li_{12}Zn_2Ge_4O_{16}$ from the lowest energy one, two excess Li ions partially occupy a half of four Li(3) sites. The positions of excess Li ions or the directions of apexes of [LiO_4] tetrahedra are different among these six configurations. This result implies that $Li_3Zn_{0.5}GeO_4$ can have a disordered

structure. We infer that this is the reason that the conductivity of $Li_3Zn_{0.5}GeO_4$ is higher among $Li_{2+2x}Zn_{1-x}GeO_4$ solid solution systems.

Next, the structures other than the most stable one are discussed. In order to estimate possibility of synthesis for these structures, free energies at high temperatures must be compared between different phases. This attempt is beyond our purpose of this study. However, we can estimate the potential of conductive property from the energy distribution. Regarding β-Li_4GeO_4, energy difference between the lowest configuration and the second lowest one is 0.11 eV per $Li_{16}Ge_4O_{16}$. The energy difference is approximately a quarter of that of α-Li_4GeO_4. Regarding γ-Li_4GeO_4, in the lowest energy configuration, four excess Li ions occupy Li(3) sites. While, in the fifth lowest energy configuration, four excess Li ions occupy Li(4) sites. The energy difference between the lowest configuration and the fifth lowest one is small, 0.046 eV per $Li_{16}Ge_4O_{16}$ in spite of different excess Li-ion configurations. These results imply that γ-Li_4GeO_4 can have more disordered structures including a variety of cation configurations compared with α- and β-Li_4GeO_4. α and β structures of $Li_3Zn_{0.5}GeO_4$ can be discussed in the same way. In particular, in the case of α-$Li_3Zn_{0.5}GeO_4$ shown in Figure 2.5(c), two excess Li ions occupy Li(5) sites in the lowest energy configuration. There are twelve configurations within a higher energy range of 0.21 eV per $Li_{12}Zn_2Ge_4O_{16}$ from the lowest energy one. In twelve configurations, excess Li ions can occupy not only Li(5) but also Li(4). Therefore, α-$Li_3Zn_{0.5}GeO_4$ has a potential to change Li-ion positions as high as γ-$Li_3Zn_{0.5}GeO_4$.

As discussed above, it is possible to evaluate energy change due to ionic jump semiquantitatively from energy distribution of cation configurations. In order to precisely estimate ionic conduction property such as diffusion coefficient, we have to take into account the motion of surrounding ions associated with Li-ion movement. Therefore, in the next stage, we combined calculations of energy barrier heights using transition state search method and molecular dynamics simulation at finite temperatures. They will be discussed in Chapter 3.

2. 5. Conclusions

Total energies of diverse cation configurations in a γ-unit cell size with α, β and γ structures for Li_4GeO_4 and $Li_3Zn_{0.5}GeO_4$ were systematically estimated by first-principles calculations. Major results are as follows:

1. Total energy of cation configuration tends to increase with increasing its volume. It is surmised that in an energetic unfavorable configuration, cations repel each other, resulting in the volume expansion.

2. The lowest energy configurations of Li_4GeO_4 and $Li_3Zn_{0.5}GeO_4$ were obtained from the structural patterns of α and γ structures, respectively. Those structures are consistent with reported diffraction data.

3. Excess Li ions at interstitial sites as well as at Li ions at regular tetrahedral sites are tetrahedrally coordinated with oxide ions. Such coordination is common in the lowest energy configurations with α, β and γ structures for Li_4GeO_4 and $Li_3Zn_{0.5}GeO_4$.

4. In γ-$Li_3Zn_{0.5}GeO_4$, excess Li ions prefer the interstitial Li(3) and Li(4) sites which have edges sharing with [GeO_4]. Energy stability of an interstitial site is strongly correlated with distances between an excess Li ion at the interstitial site and the neighboring Ge ions.

5. In α-Li_4GeO_4, energy difference, ΔE, between the most stable configuration and the second stable one is large, 0.56 eV per $Li_{16}Ge_4O_{16}$. This large ΔE implies that Li_4GeO_4 has an ordered structure even at high temperatures. This is consistent with experimental data that the conductivity of Li_4GeO_4 is very low.

6. On the other hand, in γ-$Li_3Zn_{0.5}GeO_4$, there are a lot of configurations energetically close to the lowest energy one. Those configurations have different Li-ion spatial arrangements. This implies that γ-$Li_3Zn_{0.5}GeO_4$ has a more disordered structure than α-Li_4GeO_4.

7. It was suggested that γ-Li_4GeO_4 and α-$Li_3Zn_{0.5}GeO_4$ have the possibilities of exhibiting ionic

conductivities higher than that of the most stable phase based on the energy distributions of their cation configurations.

2. 6. Appendix: Li-Ion Disordering in a Bipyramid

Initial cation configurations in this study were chosen based on two following assumptions. (1) Excess Li ions partially occupy interstitial octahedral sites. (2) [LiO_4] apexes can have the opposite direction relative to the *c* axis according to a basis model (β-Li_3PO_4 for β phase). This corresponds to Li-ion disordering in a trigonal bipyramid.

We constructed initial configurations according to only assumption (1) in the main text. In the Appendix, we show the effect of assumption (2) by using β-structure model of Li_4GeO_4. The number of structural patterns for $Li_{16}Ge_4O_{16}$ cell according to assumption (1) + (2) is enormous, over seven million. Therefore, we adopted $Li_8Ge_2O_8$ cell corresponding to β primitive cell. According to assumption (1), the number of structural patterns is ${}_8C_2 = 28$ since excess two Li ions partially occupy eight interstitial octahedral sites. Moreover, according to assumption (1) + (2), the number is ${}_8C_2 \times 2^6 = 1792$ since six Li ions are located at either up site or down site in each bipyramid. By using symmetric operation of space group $Pmn2_1$, it is possible to reduce the number of structural patterns to 11 for assumption (1), and to 496 for assumption (1) + (2), respectively.

Figure 2.6 shows the relationship between volume and total energy of the configuration patterns for β structures. Total energies are plotted as energy difference from the lowest energy configuration for α structure. Results based on assumption (1) and assumption (1) + (2) are plotted with different marks. Configuration A and B have the lowest energy and the second lowest one, respectively. Configuration B is obtained from assumption (1) and corresponds to the lowest energy one for $Li_{16}Ge_4O_{16}$ cell. Total energy of B is +1.457 eV per $Li_{16}Ge_4O_{16}$. Configuration A is obtained from only assumption (1) + (2). Total energy of A is +1.441 eV per $Li_{16}Ge_4O_{16}$. Although Li positions are different between A and B, total energies of A and B are very close. With respect to higher energy side than configuration B, although there are many configurations obtained from assumption (1) + (2), the energy distribution width calculated from only assumption (1) is nearly

equal to that of assumption (1) + (2). From above-mentioned discussions, the results obtained from assumption (1) are sufficient in order to understand the relationship between cation configurations and energy distribution.

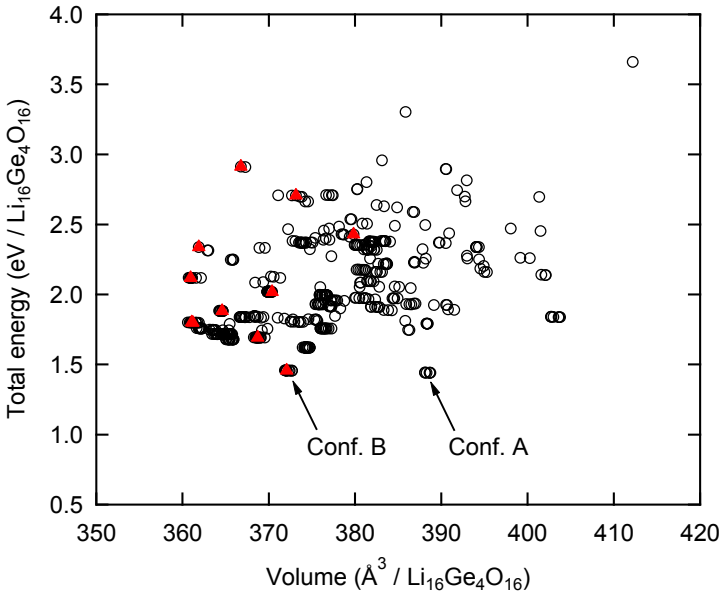

Figure 2.6. Relationship between volume and total energy of cation configurations calculated from assumption (1) (red triangle) and assumption (1) + (2) (black open circle) for β-Li_4GeO_4.

References

[1] H. Y-P. Hong, *Mat. Res. Bull.* **13** (1978) 117-124.

[2] B. E. Liebert and R. A. Huggins, *Mat. Res. Bull.* **11** (1976) 533-538.

[3] I. Abrahams, P. G. Bruce, A. R. West and W. I. F. David, *J. Solid State Chem.* **75** (1988) 390-396.

[4] I. Abrahams, P. G. Bruce, I. F. David and A. R. West, *Acta Cryst.* **B45** (1989) 457-462.

[5] H. Völlenkle and A. Wittmann, *Naturwissensch.* **54** (1967) 441.

[6] The lattice vectors of a conventional cell of α-Li_4GeO_4, $\mathbf{a}_c$, $\mathbf{b}_c$ and $\mathbf{c}_c$ have the orientation relationship, $\mathbf{a}_c \approx \mathbf{c}_p - \mathbf{b}_p$, $\mathbf{b}_c \approx \mathbf{a}_p$, and $\mathbf{c}_c \approx \mathbf{c}_p + \mathbf{b}_p$, where $\mathbf{a}_p$, $\mathbf{b}_p$ and $\mathbf{c}_p$ are the lattice vectors of a primitive cell of α phase shown in Figure 1.3(a).

[7] C. Keffer, A. Mighell, F. Mauer, H. Swanson and S. Block, *Inorg. Chem.* **6** (1967) 119-125.

[8] J. Zemann, *Acta Cryst.* **13** (1960) 863-867.

[9] P. Hohenberg and W. Kohn, *Phys. Rev.* **136** (1964) B864-B871.

[10] W. Kohn and L. J. Sham, *Phys. Rev.* **140** (1965) A1133-A1138.

[11] P. E. Blöchl, *Phys. Rev. B* **50** (1994) 17953-17979.

[12] G. Kresse and J. Hafner, *Phys. Rev. B* **48**, (1993) 13115-13118.

[13] G. Kresse and J. Furthmüller, *Phys. Rev. B* **54** (1996) 11169-11186.

[14] G. Kresse and D. Joubert, *Phys. Rev. B* **59** (1999) 1758-1775.

[15] J. P. Perdew, K. Burke, and M. Ernzerhof, *Phys. Rev. Lett.* **77** (1996) 3865-3868.

[16] K. Momma and F. Izumi, *J. Appl. Cryst.* **41** (2008) 653-658.

[17] R. D. Shannon, *Acta Cryst.* **A32** (1976) 751-767.

[18] H. Jónsson, G. Mills and K. W. Jacobsen, in *Classical and Quantum Dynamics in Condensed Phase Simulations*, edited by B. J. Berne, G. Ciccotti and D. F. Coker (World Scientific, Singapore, 1998), pp. 385-404.

Chapter 3

First-Principles Study of Oxide and Sulfide-Based Li-Ion Conducting Solid Electrolytes

3. 1. Introduction

Ceramic lithium-ion conductors are expected as solid electrolytes in next-generation rechargeable all-solid-state batteries [1-3]. Oxide-based Li-ion solid electrolytes have been energetically studied from 1970s. Those representative compounds are LISICON-type [4,5], NASICON-type [6,7], perovskite-type [8,9] and garnet-type [10]. In about a last decade, various sulfide-based Li-ion conductors exhibiting better ionic conductivities over oxides have been discovered [11-16]. And, in 2011, Kamaya *et al*. reported $Li_{10}GeP_2S_{12}$ which exhibits the ionic conductivity of 12 mS cm^{-1} at room temperature [17]. This conductivity exceeds those of organic liquid electrolytes. A sulfide ion has larger ionic radius and larger ionic polarizability than an oxide ion. It has been qualitatively understood that this difference is why sulfides have wider Li-ion migration paths than oxides. However, theoretical understanding about Li-ion diffusion mechanisms of oxides and sulfides is not still sufficient. In order to design novel solid electrolytes exhibiting high ionic conductivity, it is important to elucidate those Li-ion diffusion mechanisms.

Among crystalline inorganic Li-ion conductors, LISICON-based compounds are most common. $Li_{3.5}Zn_{0.25}GeO_4$ is the original LISICON composition and exhibits high ionic conductivity, 0.125 S cm^{-1} at 573 K. LISICON is a member of a solid solution system of $Li_{2+2x}Zn_{1-x}GeO_4$ ($0 \leq x \leq 1$) [4]. Thereafter a lot of solid solutions which replace zinc or germanium with diverse elements have been investigated [18-23] and are called LISICONs in this study. Sulfide systems found by Kanno *et al.* also have the LISICON structure and are known as thio-LISICON family [11-13].

Figure 3.1 shows a unit cell of γ-$Li_{2+2x}Zn_{1-x}GeO_4$. Its structure is orthorhombic with a space group *Pmnb* (No.62). Oxide ions are arrayed as distorted hexagonal close packing. Cations fully occupy tetrahedral sites according to structure refinements using neutron diffraction [24]. Tetrahedral sites are categorized into Li(1) and Li(2). Excess Li ions partially occupy interstitial

octahedral sites. Octahedral sites are categorized into Li(3), Li(4), Li(5) and Li(6). The distinct octahedral sites have different positional relationship with [GeO_4] tetrahedra. A bipyramid shown in Figure 3.1(a) is composed of two tetrahedra. Only one cation can be located in one bipyramid due to electrostatic repulsion between cations. LISICONs have three crystalline polymorphs which are labeled γ as well as α and β [25,26]. The difference between three polymorphs depends on position of a cation in a bipyramid as shown in Figure 1.3. On the other hand, the structural data of Li_3PS_4 at 673 K shows that the occupancy of tetrahedral sites is much less than unity [26]. This means that sulfides have more Li-ion disordered configurations than oxides.

In order to analyze ionic jumps, first-principles calculations based on density functional theory (DFT) have been widely used. LISICONs have low symmetric and disordered structures. If we evaluate ionic jumps in LISICONs, a lot of Li-ion configurations should be taken account. As discussed in Chapter 2, we qualitatively estimated Li-ion migration energies for Li_4GeO_4 and $Li_3Zn_{0.5}GeO_4$ from DFT energy distribution of diverse cation configurations. In order to evaluate ionic jumps more quantitatively, the nudged elastic band (NEB) method [27] is suitable to calculate energy barrier associated with an ionic migration path for a given atomic configuration [28,29]. Effective frequency for the ionic jump can also be computed from first-principles [30]. However, it is complicated and heavy task to cover all migration paths for enormous varieties of chemical environments using the above ways. In such cases, the first-principles molecular dynamics (FPMD) simulation is an attractive alternative and has been recently used [31,32], since it does not require an *a priori* specification of the migration path or mechanism for the ionic self-diffusion to be probed.

The LISICON structure is suitable for comparison between oxides and sulfides because a wide range of oxides and sulfides with the LISICON structure have been reported so far. We adopted $Li_{2+2x}Zn_{1-x}GeO_4$ ($0 \leq x \leq 1$) as well as $Li_{3+x}Ge_xP_{1-x}O_4$ ($0 \leq x \leq 1$) and $Li_{3+x}Ge_xP_{1-x}S_4$ ($0 \leq x \leq 1$) as solid solution candidates to compute Li-ion diffusion. First, energy barriers of Li-ion migration paths were evaluated using the NEB method. Based on this result, the relation between the assumed migration mechanisms and the energy barriers is discussed. Next, Li-ion diffusion behavior at finite temperatures was computed using the FPMD simulations. As a result, diffusion coefficients, activation energies and Li-ion density distributions are statistically estimated and possible migration

mechanisms are discussed.

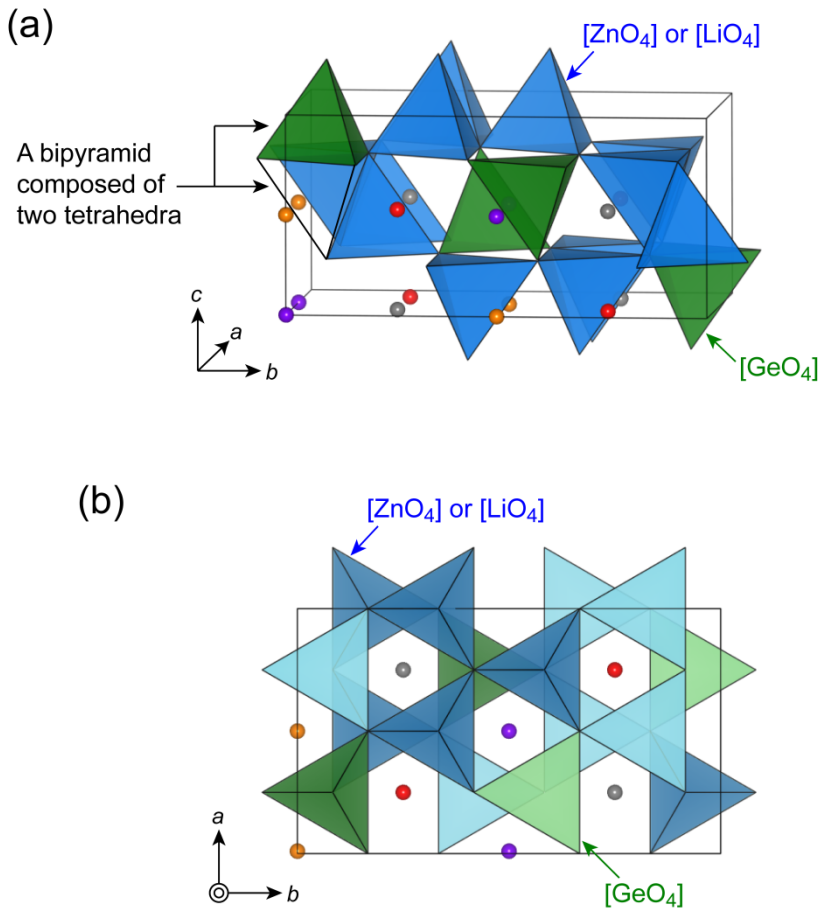

Figure 3.1. (a) perspective view and (b) projection view down the *c* axis of a unit cell of γ-$Li_{2+2x}Zn_{1-x}GeO_4$. The red, orange, purple and gray balls denote four crystallographically distinct interstitial octahedral sites, Li(3); (0.25, 0.25, 0.5), Li(4); (0, 0, 0.5), Li(5); (0, 0, 0) and Li(6); (0.25, 0.25, 0). Li(3), Li(4), Li(5) and Li(6) correspond to Wyckoff positions, 4*c*, 4*b*, 4*a* and 4*c*, respectively. Coordination octahedra of Li(3) sites have one edge sharing with [GeO_4], those of Li(4) sites have two edges sharing with [GeO_4], those of Li(5) sites have two faces sharing with [GeO_4], and those of Li(6) sites have one face sharing with [GeO_4].

3. 2. Computational Methods

All calculations in this study were performed using DFT [33,34] with the projector augmented wave (PAW) method [35] as implemented in the VASP code [36-38]. The form of the exchange-correlation term was taken to be the generalized gradient approximation (GGA) [39]. The configurations of valence electrons were $1s^2\ 2s^1$ for Li, $3d^{10}\ 4s^2$ for Zn, $3d^{10}\ 4s^2\ 4p^2$ for Ge, $3s^2\ 3p^3$ for P, $2s^2\ 2p^4$ for O, $3s^2\ 3p^4$ for S. The radial cutoffs of the PAW potentials of Li, Zn Ge, P, O and S are 2.05, 2.30, 2.30, 1.90, 1.85 and 1.90 Å, respectively. The γ-Li_3PO_4 structure [40] was adopted as a computational model since most LISICONs exhibiting high ionic conductivity are known to have this structure. Details on the migration path search simulations, the FPMD simulations and computational models used in those simulations are expressed in Section 3.2.1 and 3.2.2. The total energy convergence was better than 10^{-2} meV per cell. The software VESTA [41] was used to visualize crystal structures.

3. 2. 1. The Migration Path Search Simulations

In this study, Li-ion migration paths in $Li_3Zn_{0.5}GeO_4$, $Li_{3.5}Ge_{0.5}P_{0.5}O_4$ and $Li_{3.5}Ge_{0.5}P_{0.5}S_4$ were investigated. These compounds have two excess Li ions in a γ-unit cell. It is considered that excess Li ions contribute to ionic diffusion assuming that those ions partially occupy interstitial octahedral sites. We propose two kinds of migration mechanisms, “the interstitial mechanism” and “the cooperative mechanism”. Figure 3.2 demonstrates the schematic view of each mechanism. In the interstitial mechanism, an excess Li ion at an octahedral site moves to another octahedral site. In the cooperative mechanism, an excess Li ion at an octahedral site moves to a neighboring tetrahedral site and the Li ion at the tetrahedral site simultaneously moves to another neighboring octahedral site.

Energy barriers of migration paths are calculated using the NEB method. This is a method to find a saddle point and a minimum energy path for ionic hopping to a neighboring site. First, potential energies of two atomic configurations corresponding to an initial state and a final state for ionic hopping are calculated. Next, a series of intermediate images corresponding to a trajectory of

ionic motion between two obtained potential minima is generated. Then, those images are relaxed to minimize the total energies under the constraint that each image remains on a plane perpendicular to the hypertangent between two neighboring images.

In order to precisely evaluate energy barriers for Li-ion disordered compounds like LISICONs, ionic jumps for enormous varieties of atomic configurations must be taken into account. Moreover, for a given atomic configuration, multiple hoppings from the initial position to the same symmetric one must be covered. However, we adopted only a Li-ion migration to a neighboring site for a particular initial state from a viewpoint of computational task. This initial state was set to be the lowest energy configuration among diverse ones. Even this restricted way is expected to be useful to compare different migration mechanisms.

In order to determine an initial state, spatial atomic configurations for a γ-unit cell containing four formula units were constructed according to the γ-Li_3PO_4 structure as mentioned in Chapter 2. In the case of $Li_3Zn_{0.5}GeO_4$, Ge ions occupy P sites in the γ-Li_3PO_4 structure, two Zn ions are located at the farthest Li(1) sites each other and ten Li ions are located at the residual tetrahedral sites. In the case of $Li_{3.5}Ge_{0.5}P_{0.5}O_4$ and $Li_{3.5}Ge_{0.5}P_{0.5}S_4$, two Ge ions are located at the farthest P sites each other in the γ-Li_3PO_4 structure, two P ions are located in the same way and twelve Li ions are located at the residual tetrahedral sites. Two excess Li ions partially occupy 16 octahedral sites and thereafter DFT energies were estimated for ${}_{16}C_2 = 120$ configurations. In these calculations, all internal positions, lattice constants and lattice shapes were relaxed. Numerical integration over the Brillouin zone was carried out by 4 × 2 × 4 k-point meshes. The plane-wave cutoff energies of 400 eV were employed. The relaxation procedure was truncated when the residual forces on the relaxed atoms became smaller than 0.02 eV/Å.

The cell with the lowest energy configuration was magnified to 2 × 1 × 2 γ-unit cells as an initial state to enable relaxation of surrounding environment associated with Li-ion migration. Then, total energy of a final state was calculated. Before the NEB calculation, the internal position of the *i*-th atom for the *j*-th image was set to be

$$\mathbf{r}_{i,j} = \mathbf{r}_{i,ini} + \frac{j}{n+1}\left(\mathbf{r}_{i,fin} - \mathbf{r}_{i,ini}\right),$$

where n is the number of intermediate images. $\mathbf{r}_{i,ini}$ and $\mathbf{r}_{i,fin}$ are the internal positions of the i-th atom for the initial state and the final state, respectively. Each image is placed at even distances under a usual way as shown in the above equation. However, the number of images and the distance between images should be changed flexibly depending on complexity of migration path. In the NEB calculation, all internal atomic positions are allowed to relax without change of lattice constants.

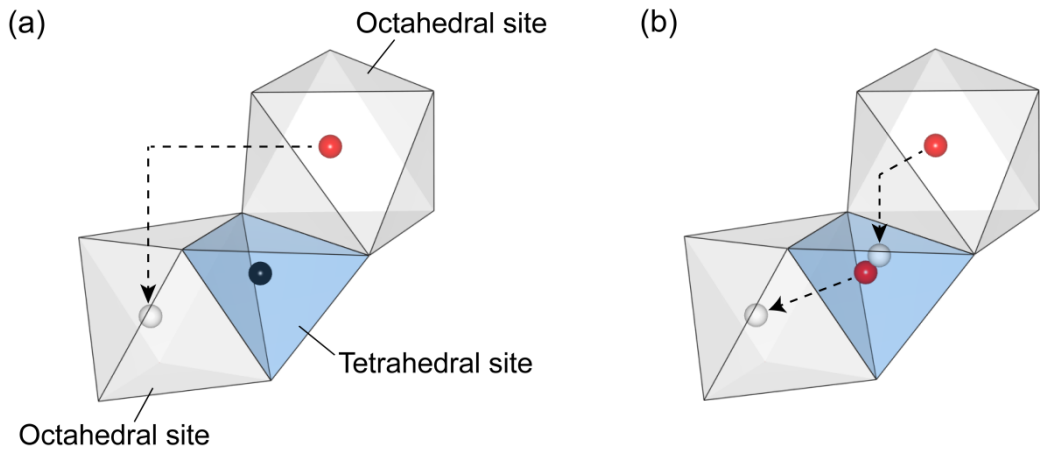

Figure 3.2. Proposed migration mechanisms: (a) the interstitial mechanism and (b) the cooperative mechanism. The red and white balls denote Li ions at the initial and final state, respectively. The black ball denotes a Li ion at a tetrahedral site which does not contribute to the interstitial mechanism.

3. 2. 2. The FPMD Simulations

We adopted $Li_{2+2x}Zn_{1-x}GeO_4$ (x = 0, 0.25, 0.50, 0.75 and 1), $Li_{3+x}Ge_xP_{1-x}O_4$ (x = 0, 0.25, 0.50, 0.75 and 1) and $Li_{3+x}Ge_xP_{1-x}S_4$ (x = 0, 0.25, 0.50, 0.75 and 1) for candidates of the FPMD simulations. Computational cells were constructed from 2 × 1 × 2 γ-unit cells containing 16 formula units. In the case of $Li_{2+2x}Zn_{1-x}GeO_4$, Ge ions occupy P sites of the γ-Li_3PO_4 structure. In order to model disordered solid solutions, Zn and Li ions are randomly distributed over residual tetrahedral sites and excess Li ions (x per formula unit) are randomly distributed over octahedral sites. In the

case of $Li_{3+x}Ge_xP_{1-x}O_4$ and $Li_{3+x}Ge_xP_{1-x}S_4$, Ge and P ions are randomly distributed over P sites of the γ-Li_3PO_4 structure. Li ions occupy residual tetrahedral sites and excess Li ions are randomly distributed over octahedral sites. Before the FPMD simulations, all internal positions, lattice constants and lattice shapes were relaxed. In this relaxation, the plane-wave cutoff energies of 400 eV were employed. Integration in reciprocal space was performed at the Γ-point only.

The FPMD simulations were performed within the *NVT* ensemble using Nosé thermostat [42] for the relaxed computational cells. Volume and shape of the cell were fixed during the FPMD simulations and thereby any contributions from thermal expansion were neglected. The plane-wave cutoff energy was reduced to 300 eV to keep the computational cost at an acceptable level. The initial temperature was set to the value according to Boltzmann distribution. The time step was chosen to be 2 fs which is sufficient to reproduce vibration frequencies for typical ionic conductors. The first 2500 steps, corresponding to 5 ps, were treated as a thermal equilibrium stage and discarded before analyzing diffusivity.

3. 3. Results and Discussion

3. 3. 1. The Migration Path Search Simulations

In order to construct an initial state of ionic migration, total energies of a variety of cation configurations for a γ-unit cell were calculated. Energy stability of each octahedral site can be understood based on these calculations. In the lowest energy cation configuration of $Li_3Zn_{0.5}GeO_4$ and $Li_{3.5}Ge_{0.5}P_{0.5}O_4$, two excess Li ions occupy Li(3) sites. The most stable site is Li(3) and the second most stable site is Li(4). While, in the lowest energy configuration of $Li_{3.5}Ge_{0.5}P_{0.5}S_4$, two excess Li ions occupy Li(4) sites. The most stable site is Li(4) and the second most stable site is Li(3). If an excess Li ion moves to Li(5) or Li(6) in all the three compounds, energy states become higher. The cell with the lowest energy configuration was magnified to 2 × 1 × 2 γ-unit cells as an initial state.

Migration paths in $Li_3Zn_{0.5}GeO_4$ are discussed. Excess Li-ion movements from the octahedral Li(3) site to neighboring octahedral sites were investigated. Assuming that neighboring octahedral sites are restricted to Li(3) and Li(4), a total of eight kinds of migration paths are enumerated. The final states for two of those eight paths are not energetically stable and Li ions return to the original position. For one of the residual six paths, energy profiles of the interstitial mechanism and the cooperative one are shown in Figure 3.3(a). A cubic spline curve interpolates between images. In the interstitial mechanism of this path, a Li ion at a Li(3) site moves to another Li(3) site. The Li ion passes through an octahedral Li(6) site on the path. The position corresponds to the normalized migration distance d_m = 0.4. In the cooperative mechanism, a Li ion at a Li(3) site moves to a neighboring Li(1) site and the Li ion at the Li(1) site moves to another neighboring Li(3) site. The interstitial mechanism has more complicated profile than the cooperative one. Energy barrier of the interstitial mechanism is 1.26 eV and considerably higher than that of the cooperative one, 0.38 eV. Therefore, Li-ion migration by the interstitial mechanism is expected to be rare extremely.

Energy profiles of the six paths with the cooperative mechanism in $Li_3Zn_{0.5}GeO_4$ are shown in Figure 3.3(b). Sites where two Li ions jump through and the energy barriers are listed in Table 3.1. The above discussed path corresponds to the path 2. All energy profiles have only one

maximal value except the path 4. Energy barriers of the paths 1-6 are different from 0.38 to 1.10 eV. This quite difference is attributed to the sites where mobile Li ions jump through. Moreover, it was found that Li ions surrounding the mobile Li ions can move in a bipyramid from up to down and vice versa. Position change of surrounding Li ions leads to decrease of energy barrier. In this study, an initial state was restricted to only the lowest energy cation configuration. If the number of initial state patterns increases including position change of surrounding Li ions, paths exhibiting smaller energy barriers may be found.

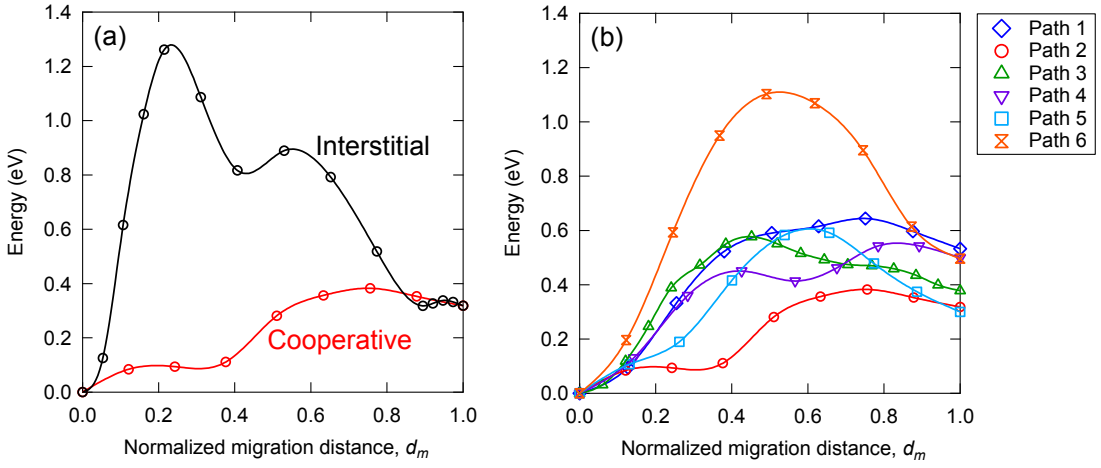

Figure 3.3. Energy profiles of Li-ion migration in $Li_3Zn_{0.5}GeO_4$. (a) the path 2 with the interstitial mechanism and the cooperative mechanism. (b) the paths 1-6 with the cooperative mechanism.

Table 3.1. Sites where two Li ions jump through and the energy barriers for the six paths with cooperative mechanism in $Li_3Zn_{0.5}GeO_4$. Since positions of one tetrahedral site and the other tetrahedral site in a bipyramid correspond to up and down along the *c* axis, each tetrahedral site is indicated by a subscript "up" or "down".

Path	Sites where one Li ion jump through	Sites where the other Li ion jump through	Energy barrier (eV)
1	Li(3) => $Li(1)_{down}$ => $Li(1)_{up}$	$Li(1)_{up}$ => Li(3)	0.64
2	Li(3) => $Li(1)_{up}$	$Li(1)_{up}$ => $Li(1)_{down}$ => Li(3)	0.38
3	Li(3) => $Li(1)_{down}$ => $Li(1)_{up}$	$Li(1)_{up}$ => Li(4)	0.58
4	Li(3) => $Li(2)_{up}$ => $Li(2)_{down}$	$Li(2)_{down}$ => Li(4)	0.54
5	Li(3) => $Li(2)_{up}$ => $Li(2)_{down}$	$Li(2)_{down}$ => Li(4)	0.59
6	Li(3) => $Li(1)_{up}$	$Li(1)_{up}$ => Li(4)	1.10

In the case of $Li_{3.5}Ge_{0.5}P_{0.5}O_4$, five migration paths are enumerated in the same way as $Li_3Zn_{0.5}GeO_4$. Energy profiles for these paths with the cooperative mechanism via a tetrahedral site are shown in Figure 3.4. All energy profiles have only one maximal value except the path 3. Shapes of energy profiles of $Li_{3.5}Ge_{0.5}P_{0.5}O_4$ are similar to those of $Li_3Zn_{0.5}GeO_4$. The energy barriers are from 0.35 to 0.61 eV.

In the case of $Li_{3.5}Ge_{0.5}P_{0.5}S_4$, seven migration paths are enumerated in the same way. Energy profile for one of these paths with the interstitial mechanism and the cooperative one are shown in Figure 3.5(a). In the interstitial mechanism, a Li ion at a Li(4) site moves to another Li(4) site. The Li ion moves especially in the normalized migration distance range of $0.36 < d_m < 0.65$ of the energy profile. The energy changes in the other distance range are attributed to the movement of other surrounding Li ions in the bipyramids. In the cooperative mechanism, a Li ion at a Li(4) site moves to a neighboring Li(2) site and the Li ion at the Li(2) site moves to another neighboring Li(4) site. Energy barriers of the interstitial mechanism and the cooperative one are 0.59 eV and 0.21 eV, respectively. Similarly to $Li_3Zn_{0.5}GeO_4$, it is predicted that the cooperative mechanism is more frequent than the interstitial one. Energy profiles of the seven paths with the cooperative mechanism are shown in Figure 3.5(b). The above discussed path corresponds to the path 1. Energy barriers are from 0.21 to 0.64 eV.

As discussed above, even if an initial state is restricted to a particular atomic configuration, it is possible to compare different mechanisms qualitatively. However, since energy barrier strongly depends on Li-ion migration path, it is difficult to precisely evaluate an average activation energy for the solid solution. Li-ion migration mechanisms were investigated by not only the migration path search simulations but also the FPMD simulations. The detailed results are discussed in Section 3.3.2.

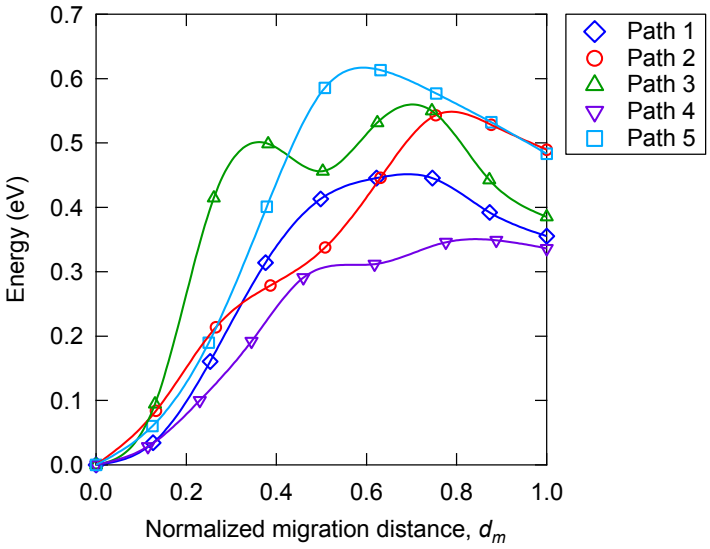

Figure 3.4. Energy profiles of Li-ion migration for the five paths with the cooperative mechanism in $Li_{3.5}Ge_{0.5}P_{0.5}O_4$.

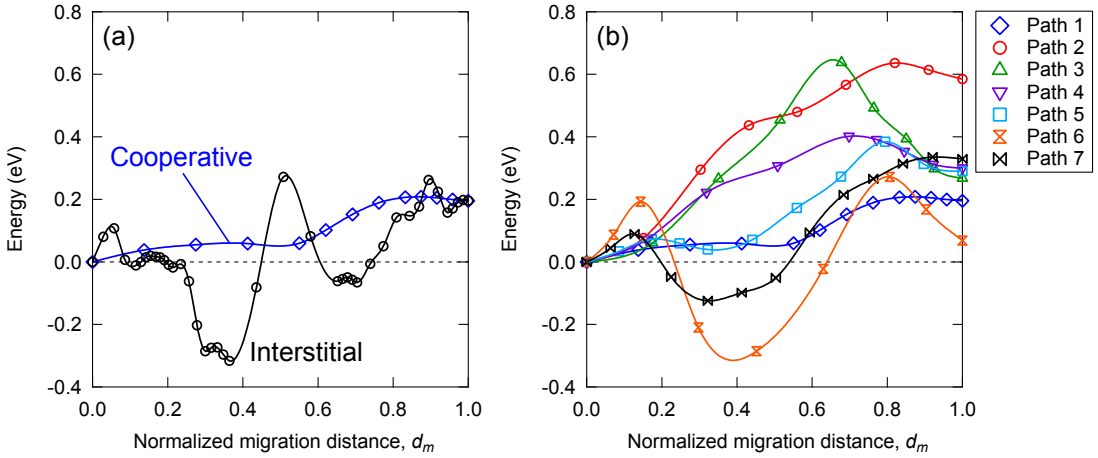

Figure 3.5. Energy profiles of Li-ion migration in $Li_{3.5}Ge_{0.5}P_{0.5}S_4$. (a) the path 1 with the interstitial mechanism and the cooperative mechanism. (b) the paths 1-7 with the cooperative mechanism.

3. 3. 2. The FPMD Simulations

3. 3. 2. 1. Lattice Volume

Lattice volumes per formula unit for $Li_{2+2x}Zn_{1-x}GeO_4$, $Li_{3+x}Ge_xP_{1-x}O_4$ and $Li_{3+x}Ge_xP_{1-x}S_4$ with the γ structure after geometry relaxation expressed in Section 3.2.2 are shown in Figure 3.6. Since the structure analysis of end member (x = 0 and 1) for each solid solution have been reported by using X-ray diffraction or neutron diffraction, the experimental and calculated values with ordered structure at the end member are also plotted. The β structure is most stable at x = 0 for all solid solutions [43,44,26]. The α structure is most stable at x = 1 for $Li_{2+2x}Zn_{1-x}GeO_4$ and $Li_{3+x}Ge_xP_{1-x}O_4$, i.e. Li_4GeO_4 [45]. The γ structure is most stable at x = 1 for $Li_{3+x}Ge_xP_{1-x}S_4$, i.e. Li_4GeS_4 [13]. Moreover, the experimental values at the intermediate member are plotted. x = 0.5 and 0.75 for $Li_{2+2x}Zn_{1-x}GeO_4$ have the γ structure [24]. Structures of the intermediate member for $Li_{3+x}Ge_xP_{1-x}O_4$ and $Li_{3+x}Ge_xP_{1-x}S_4$ are unknown in detail [21,12]. However, it is supposed that x = 0.4, 0.6 and 0.8 of $Li_{3+x}Ge_xP_{1-x}S_4$ have the γ structure because those lattice volumes are similar to that of x = 1. The lattice volumes of $Li_{3+x}Ge_xP_{1-x}S_4$ are about twice as large as those of $Li_{2+2x}Zn_{1-x}GeO_4$ and $Li_{3+x}Ge_xP_{1-x}O_4$. The slight overestimation comparing to the experiment falls within a general error based on GGA. The calculation results could reproduce the relationship that volume decreases with increasing x in $Li_{2+2x}Zn_{1-x}GeO_4$ and volume increases with increasing x in $Li_{3+x}Ge_xP_{1-x}O_4$ and $Li_{3+x}Ge_xP_{1-x}S_4$.

3. 3. 2. 2. Charge State

The electronic charge density calculated by DFT for the relaxed structure can be decomposed into atomic contributions using the Bader analysis [46-48]. In this analysis, the dividing surface is at a minimum in the charge density. Figure 3.7 shows the average of charge states of each element in the computational cell. The charge states of any elements are nearly independent of x, i.e. stoichiometry. The Li charge states of all solid solutions are almost the same, from +0.87 to +0.89. This means that Li ions are attached to anions by ionic chemical bonds in whether oxides or sulfides. The charge states of Ge and P in $Li_{3+x}Ge_xP_{1-x}O_4$ are approximately +2.2 and +3.5, respectively. While, the charge states of Ge and P in $Li_{3+x}Ge_xP_{1-x}S_4$ are reduced to approximately +1.3 and +1.2,

respectively. Therefore, the chemical bonding character between Ge or P and anions in sulfides is more covalent than that in oxides.

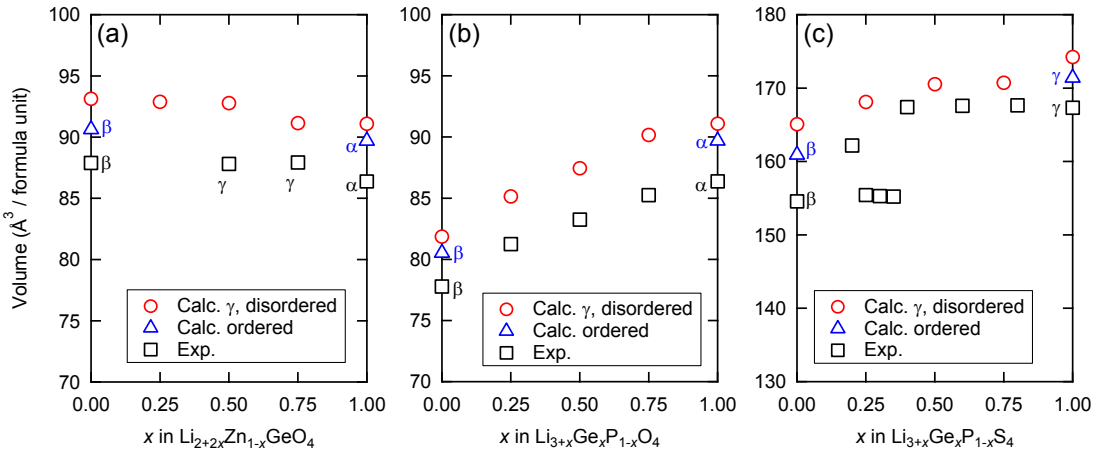

Figure 3.6. Lattice volumes of solid solutions. (a) $Li_{2+2x}Zn_{1-x}GeO_4$, (b) $Li_{3+x}Ge_xP_{1-x}O_4$, and (c) $Li_{3+x}Ge_xP_{1-x}S_4$.

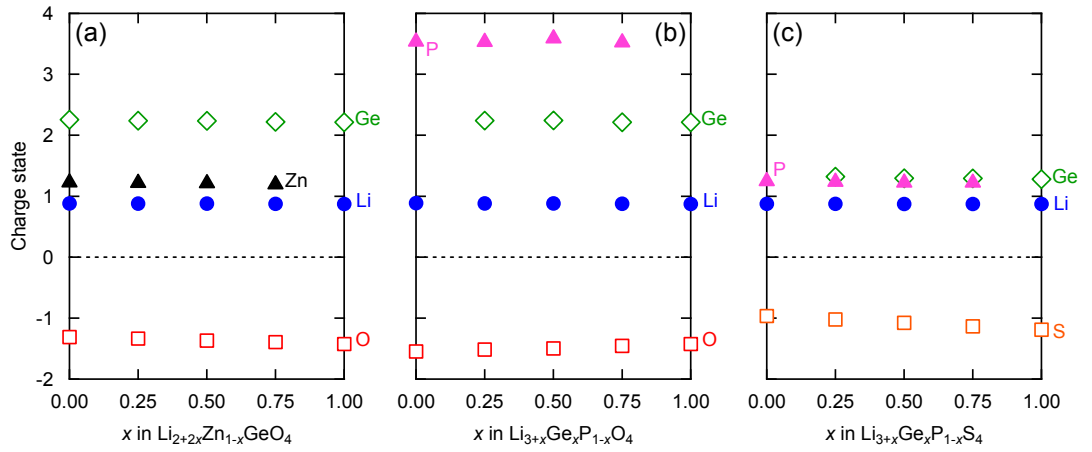

Figure 3.7. Charge states of each element calculated based on the Bader analysis. (a) $Li_{2+2x}Zn_{1-x}GeO_4$, (b) $Li_{3+x}Ge_xP_{1-x}O_4$, and (c) $Li_{3+x}Ge_xP_{1-x}S_4$.

3. 3. 2. 3. Convergence of Diffusion Coefficient

Diffusion coefficients for the LISICON-based compounds were estimated from the FPMD simulations. The diffusion coefficient is defined from the Einstein relationship as

$$D = \lim_{t\to\infty} \frac{\left\langle [\mathbf{r}(t)]^2 \right\rangle}{6t},$$

where $<[\mathbf{r}(t)^2]>$ is the mean square displacement (MSD) of a given species over time t measured from initial time t_0. The MSD of Li ions can be written

$$\left\langle [\mathbf{r}(t)]^2 \right\rangle_{\mathrm{Li}} = \frac{1}{N_{\mathrm{Li}}} \sum_{i=1}^{N_{\mathrm{Li}}} [\mathbf{r}_i(t+t_0) - \mathbf{r}_i(t_0)]^2 ,$$

where N_{Li} is the total number of Li ions within the computational cell and $\mathbf{r}_i(t)$ is the position of the i-th Li ion at time t. Therefore, D can be obtained by a linear fitting of the MSD curve over $6t$.

Estimated diffusion coefficient tends to converge with increasing time t. In order to verify its convergence, the FPMD simulations of $Li_3Zn_{0.5}GeO_4$ at 1600 K were performed using 10 sample cells under following two conditions, I and II. The condition I is that the 10 sample cells have the same initial atomic position but the different initial atomic velocity distributions. The condition II is that the 10 sample cells have the different initial atomic positions and the different initial atomic velocity distributions.

Figure 3.8 summarizes the time dependence of 10 samples average of the diffusion coefficients for the two conditions. The 95 % confidence intervals are also plotted as error bar format. For the condition I, the average diffusion coefficient has a tendency to converge. The averages at 20, 25 and 30 ps are almost the same, 3.8×10^{-5} cm^2/s. The error corresponding to the difference between sample average and confidence limit is about ±9 % of the absolute value and does not really decrease after 15 ps. On the other hand, for the condition II, the average diffusion coefficient is between 3.8×10^{-5} and 3.9×10^{-5} cm^2/s and varies only slightly from 5 ps to 30 ps. This few changes are due to averaging of different initial atomic configurations. Since the error for the condition II is about ±9 % of the absolute value and is similar to the condition I, the contribution of initial atomic position to diffusion coefficient is estimated to be very few. As a result, 20 ps data is sufficient for $Li_3Zn_{0.5}GeO_4$ to estimate average and error of diffusion coefficient. The MSD of Li

ions at 20 ps is almost 40 $Å^2$. This corresponds to three jumps of a Li ion, assuming that the migration distance to a neighboring site is about 2 Å. We decided to perform the FPMD simulations in this study for 20 ps excluding a thermal equilibrium stage. However, from the above verification, if the MSD of Li ions is smaller than 40 $Å^2$ at 20 ps, the FPMD simulations were continued until it reaches into 40 $Å^2$. $Li_{2.5}Zn_{0.75}GeO_4$ at 1200 K is the case of the longest simulation time corresponding to 100 ps.

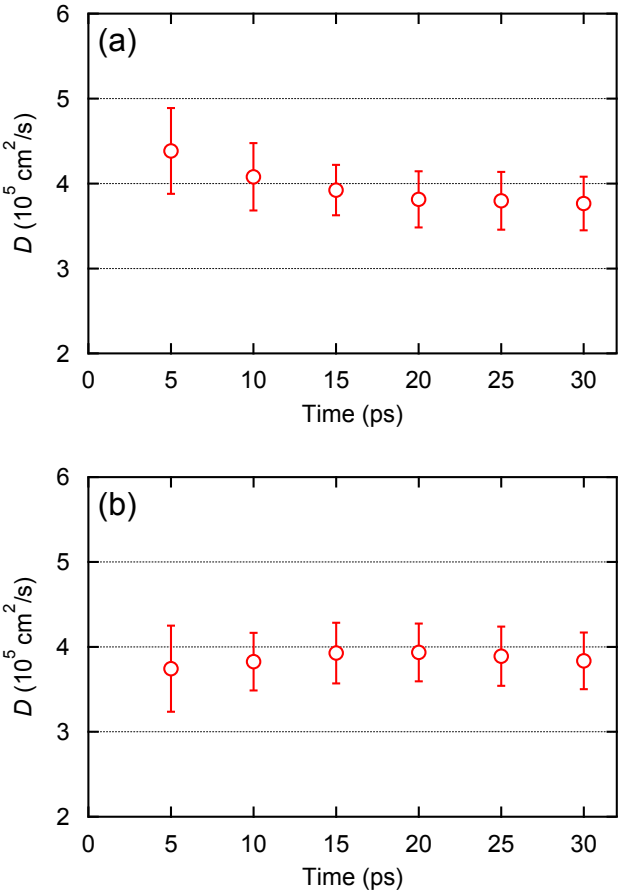

Figure 3.8. Time dependence of diffusion coefficients for (a) the condition I and (b) the condition II. The open circle and the error bar denote the average and the 95 % confidence interval of diffusion coefficients for 10 sample cells.

3. 3. 2. 4. Li-Ion Diffusivity

The MSDs of Li ions in $Li_3Zn_{0.5}GeO_4$ at six temperatures are shown in Figure 3.9(a). The MSD increases with increasing temperature. Ge and O ions do not jump between those sites and the γ-Li_3PO_4 structure is maintained at any temperature during the FPMD simulations. The MSD of Zn ions is almost zero at lower than 1400 K, while it is nearly 10 % of the MSD of Li ions at higher than 1600 K. The MSDs of Li ions in the *a*, *b* and *c* directions are also shown in Figure 3.9(b), (c) and (d). Anisotropic Li-ion diffusion was not significantly found except that the MSD in the *b* direction is larger than other directions at 1400 K. Although anisotropic diffusion is likely since LISICONs are orthorhombic, these calculation results are consistent with the fact that distinct anisotropic conductivities have not been observed for LISICONs.

We performed the FPMD simulations for $Li_{2+2x}Zn_{1-x}GeO_4$ (x = 0.25, 0.50, 0.75 and 1.00) at six temperatures. Figure 3.10 shows calculated Li-ion diffusion coefficients for the four compositions as a function of inverse temperature. For comparison, the diffusion coefficients extracted from the experimental conductivities [4,49] according to the Nernst-Einstein equation are also shown. The simulations were carried out at higher temperatures than the experiments to enable to a statistically significant number of ionic jumps to occur in the short time span as mentioned in Section 3.3.2.3. The calculated diffusion coefficient increases with increasing x from 0.25 to 1.00. This relationship between x and D reproduced the experimental one. Extrapolation of the calculated diffusion coefficients to lower temperature and their temperature dependence for x = 0.50 and 0.75 approximately fit with the experimental ones. However, since the conductivities measured by different groups are sometimes inconsistent in more than one digit, calculated diffusion coefficients should be carefully compared with experimental ones. In contrast, the experimental activation energies are mostly independent of those groups. In order to understand temperature dependence precisely, the activation energies E_a are estimated and shown in Table 3.2. The calculated E_a is close to the experimental one for x = 0.50 and 0.75. This implies that the ionic conduction mechanism is the same over two temperature regions, as might be expected since no phase change occurs. Moreover, for x = 0.50, calculated E_a, 0.36 eV, is close to the lowest energy barrier obtained from the NEB method, 0.38 eV, as shown in Figure 3.3.

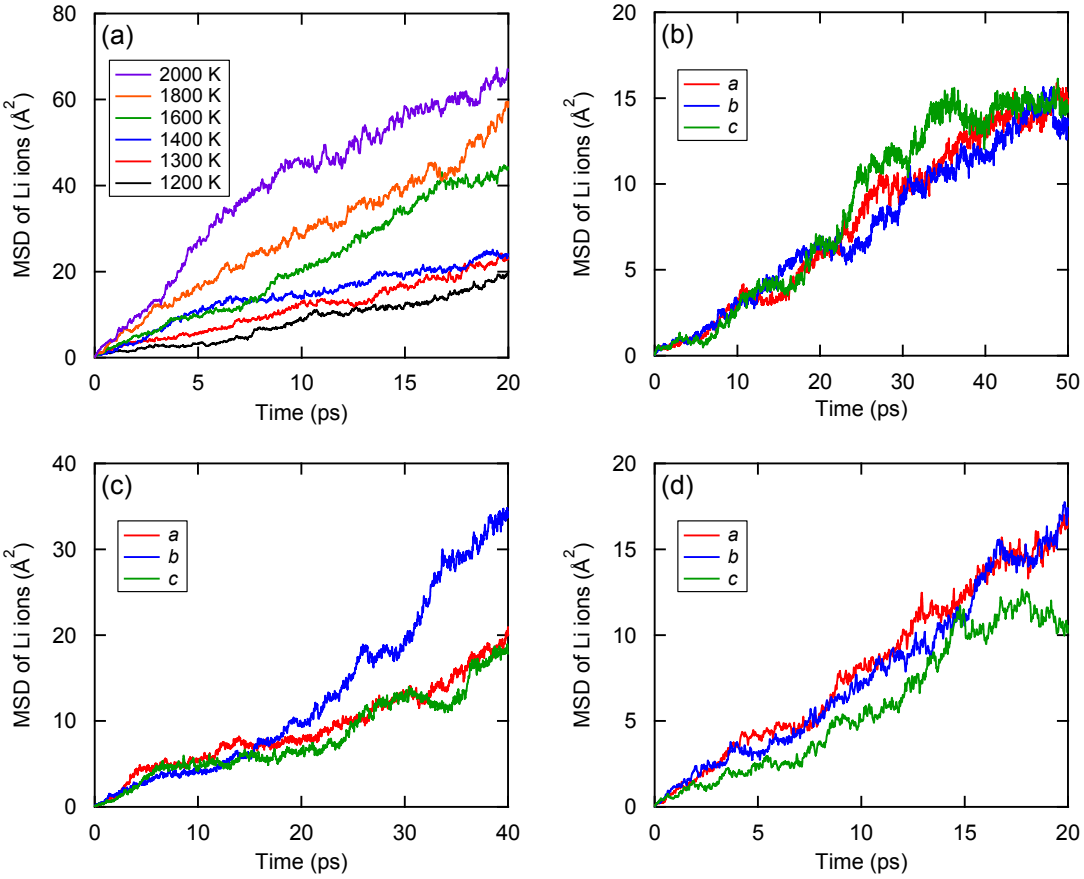

Figure 3.9. MSD of Li ions in $Li_3Zn_{0.5}GeO_4$. (a) the overall directions at six temperatures, 1200, 1300, 1400, 1600, 1800 and 2000 K. The *a*, *b* and *c* directions at (b) 1200 K, (c) 1400 K and (d) 1600 K.

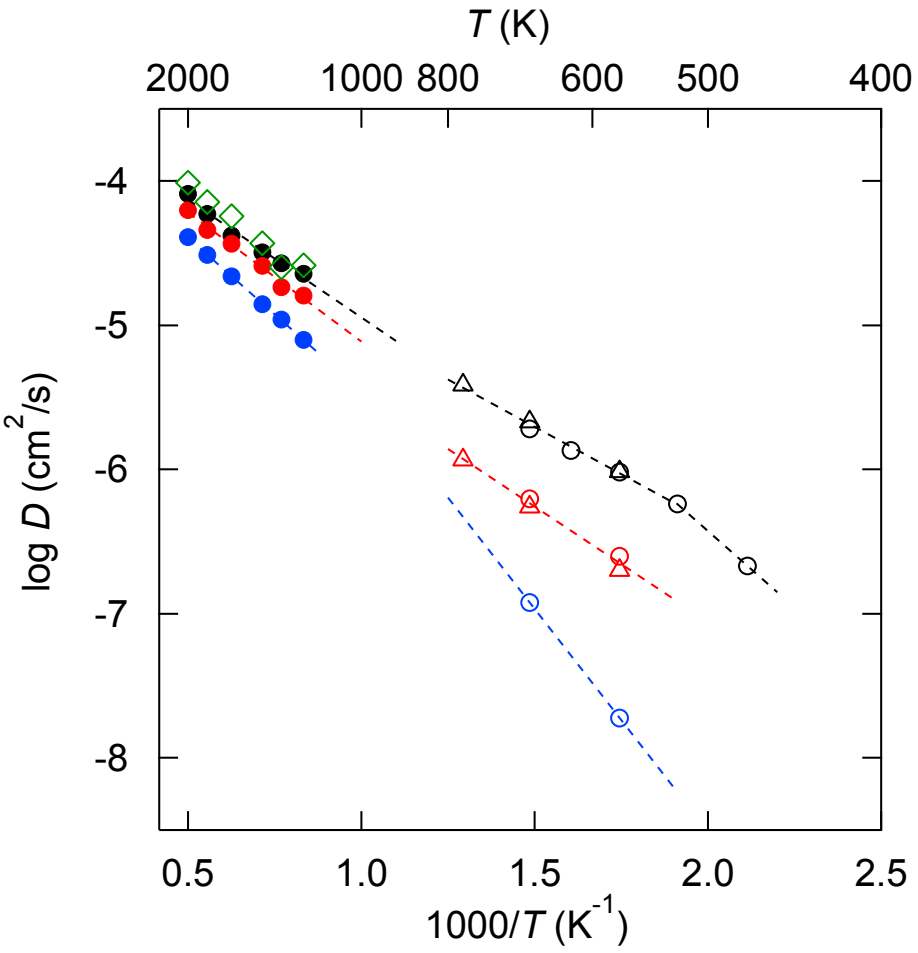

Figure 3.10. Arrhenius plots of calculated Li-ion diffusion coefficients for $Li_{2+2x}Zn_{1-x}GeO_4$. Blue, red, black closed circles and green open diamonds denote diffusion coefficients for x = 0.25, 0.50, 0.75 and 1.00, respectively. Experimental data, shown as open circles [4] and open triangles [49], are provided for comparison. Blue, red and black denote experimental diffusion coefficients for x = 0.25, 0.50 and 0.75, respectively.

Table 3.2. Calculated and experimental activation energies E_a (eV) of $Li_{2+2x}Zn_{1-x}GeO_4$. The number in parenthesis is temperature range used to estimate E_a.

x	Calculated	Experimental
0.25	0.42 (1200-2000 K)	0.61 (573-673 K) [4]
0.50	0.36 (1200-2000 K)	0.31 (573-673 K) [4] 0.34 (573-773 K) [49]
0.75	0.32 (1200-2000 K)	0.24 (523-673 K) [4] 0.27 (573-773 K) [49]
1.00	0.37 (1200-2000 K)	0.84 (444-1000 K) [50]

Experimental E_a increases at lower than 523 K for x = 0.75, indicative of a change in migration mechanism. That change is also assumed to be why the experimental E_a, 0.61 eV, is larger than the calculated E_a, 0.42 eV, for x = 0.25. In these cases, simple extrapolation of the high temperature data to low temperatures is inappropriate. In order to solve this issue, we proposed a method to predict a phase transition temperature and low temperature conductivities, assuming that a deflection point corresponds to ordering and disordering of Li ions at interstitial octahedral sites [51]. They will be discussed in Chapter 4.

Experimental conductivity for x = 1, i.e. Li_4GeO_4 with the γ structure has not been reported in the past. On the other hand, for α-Li_4GeO_4, since all Li ions occupy tetrahedral sites and no excess Li ions are located at interstitial octahedral sites [45], its conductivity is very low [50] and thus is not included in Figure 3.10. The FPMD simulation of Li_2ZnGeO_4 (x = 0) including no excess Li ions was also performed. The calculated MSD of Li ions in Li_2ZnGeO_4 was nearly zero. These discussions support that the number of excess Li ions at interstitial octahedral sites makes a significant contribution to Li-ion conductivity.

Figure 3.11 shows the calculated Li-ion diffusion coefficients of $Li_{3+x}Ge_xP_{1-x}O_4$ (x = 0.25, 0.50, 0.75 and 1.00) and $Li_{3+x}Ge_xP_{1-x}S_4$ (x = 0.00, 0.25, 0.50, 0.75 and 1.00) as a function of inverse

temperature. $Li_{3+x}Ge_xP_{1-x}S_4$ exhibit larger diffusivities by about one order of magnitude than $Li_{3+x}Ge_xP_{1-x}O_4$. This result reproduced the relationship between experimental conductivities of sulfides and those of oxides at low temperatures. Ge, P, O and S ions hardly jump between those sites, while S ions in Li_3PS_4 at 1100 and 1200 K have nearly 10 % of the MSD of Li ions. The γ-Li_3PO_4 structure is maintained during the FPMD simulations in all cases.

The calculated activation energies E_a of $Li_{3+x}Ge_xP_{1-x}O_4$ and $Li_{3+x}Ge_xP_{1-x}S_4$ are shown in Table 3.3. For comparison, experimental data of the activation energies and the diffusion coefficients D extracted from the conductivities at room temperature are also shown. For $Li_{3+x}Ge_xP_{1-x}O_4$, the calculated D increases with increasing x as shown in Figure 3.11. This is consistent with the relationship between x and experimental D at room temperature. Moreover, the calculated E_a of x = 0.75 is 0.34 eV and close to the experimental one, 0.29 eV (around 973 K). It should be notice that E_a of $Li_{3+x}Ge_xP_{1-x}O_4$ tends to increase with falling temperature as well as $Li_{2+2x}Zn_{1-x}GeO_4$. On the other hand, the relationship between x and calculated D of $Li_{3+x}Ge_xP_{1-x}S_4$ is opposite to $Li_{3+x}Ge_xP_{1-x}O_4$. This notable difference implies that the ionic conduction mechanism of $Li_{3+x}Ge_xP_{1-x}S_4$ is distinctly different from that of $Li_{3+x}Ge_xP_{1-x}O_4$. It may be inappropriate to compare the diffusion coefficients calculated by use of the γ structure with the experimental ones, since in reality the crystal structure depends on x. However, the relationship between x and D of the FPMD simulation agrees with the experiment in the wide range except x = 0 and 0.20. The calculated E_a increases with increasing x. This trend also agrees with the experiment in the wide range except x = 0 and 0.20. The discrepancy in x = 0 and 0.20 may be attributed to the fact that the solid solutions in this range has β structure or an ordered Li-ion configuration.

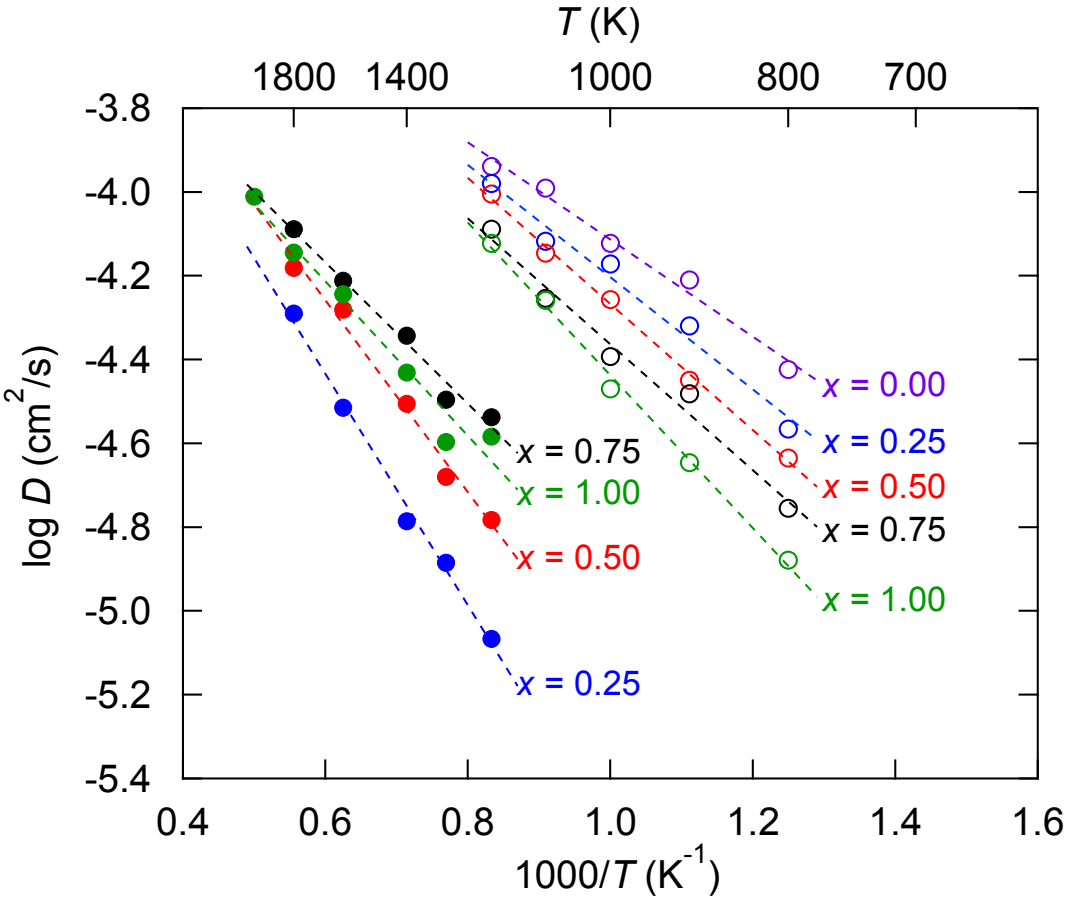

Figure 3.11. Arrhenius plots of the calculated Li-ion diffusion coefficients. $Li_{3+x}Ge_xP_{1-x}O_4$ and $Li_{3+x}Ge_xP_{1-x}S_4$ are shown as closed circles and open circles, respectively.

Table 3.3. Activation energies E_a and diffusion coefficients D at room temperature of $Li_{3+x}Ge_xP_{1-x}O_4$ and $Li_{3+x}Ge_xP_{1-x}S_4$. The number in parenthesis is the temperature range used to estimate E_a. The experimental data of $Li_{3+x}Ge_xP_{1-x}O_4$ are extracted from Ref. [21] and [52]. The experimental data of $Li_{3+x}Ge_xP_{1-x}S_4$ with $x = 0.00$, $0.20 < x < 0.80$, and $x = 1.00$ are extracted from Ref. [53], [12], and [11], respectively.

	Calculated		Experimental		
	x	E_a (eV)	x	E_a (eV)	D ($cm^2\ s^{-1}$) at RT
$Li_{3+x}Ge_xP_{1-x}O_4$	0.25	0.55 (1200-1800 K)	0.25	0.48 (190-270 K)	8.1×10^{-12}
	0.50	0.45 (1200-1800 K)	0.50	0.51 (190-270 K)	3.1×10^{-11}
	0.75	0.34 (1200-1800 K)	0.75	0.53 (190-270 K)	7.3×10^{-11}
				0.43 (around 573 K)	
				0.29 (around 973 K)	
$Li_{3+x}Ge_xP_{1-x}S_4$	0.00	0.23 (800-1200 K)	0.00	0.49 ($T < 463$ K)	2.5×10^{-12}
				0.46 ($T > 463$ K)	
	0.25	0.27 (800-1200 K)	0.20	0.27 (298-573 K)	4.1×10^{-9}
	0.50	0.30 (800-1200 K)	0.25	0.21 (298-573 K)	1.5×10^{-8}
	0.75	0.30 (800-1200 K)	0.30	0.22 (298-573 K)	1.2×10^{-8}
	1.00	0.36 (800-1200 K)	0.35	0.23 (298-573 K)	9.3×10^{-9}
			0.40	0.27 (298-573 K)	5.0×10^{-9}
			0.60	0.34 (298-573 K)	1.2×10^{-9}
			0.80	0.47 (298-573 K)	1.8×10^{-11}
			1.00	0.53 (298-573 K)	1.4×10^{-12}

3. 3. 2. 5. Li-Ion Density Distribution

Li-ion density distributions within the computational cells for Li_2ZnGeO_4 (x = 0) and $Li_3Zn_{0.5}GeO_4$ (x = 0.5) were obtained from the 20 ps FPMD simulations at 1600 K. As shown in Figure 3.12 (a) and (b), they were divided into four regions which have γ-unit cell size and were superposed. For Li_2ZnGeO_4, all Li ions are located at only teterahedral sites. No Li ions are found at interstitial octahedral sites due to absence of excess Li ions. This means that Li ions remain at tetrahedral sites and do not move to other sites. The Li-ion distribution shape for each tetrahedral site is a prolate ellipsoid which is long along the c axis because a Li ion moves back and forth between two tetrahedral sites in a bipyramid. For $Li_3Zn_{0.5}GeO_4$, Li ions are mainly located at tetrahedral sites and partially occupy octahedral sites, Li(3) and Li(4). The Li-ion densities are the highest at tetrahedral sites. Li(3) sites have larger density than Li(4) sites. No density is found at Li(5) and Li(6) sites. That is, Li ions diffuse via octahedral sites which have edge sharing with [GeO_4]. These results are consistent with the experimental data [24] and the stability of octahedral sites mentioned in Section 3.3.1. The same results were obtained from the FPMD simulations for x = 0.25, 0.75 and 1. Li-ion density distributions of $Li_{3+x}Ge_xP_{1-x}O_4$ are comparable to those of $Li_{2+2x}Zn_{1-x}GeO_4$.

Trajectories connecting between an octahedral site and another octahedral site could not be found in the Li-ion distribution. While, trajectories connecting between a tetrahedral site and an octahedral site could be clearly found. Therefore, these trajectories are mainly caused by the cooperative mechanism. This result is consistent with the energy profiles obtained by the NEB method.

Li-ion density distributions of Li_3PS_4 and $Li_{3.5}Ge_{0.5}P_{0.5}S_4$ are shown in Figure 3.13 (a) and (b). Li_3PS_4 has no excess Li ions as well as Li_2ZnGeO_4, but many Li ions were found at Li(3) and Li(4). This is consistent with the X-ray diffraction measurements of Li_3PS_4 at 637 K which have identified Li(1) and Li(2) as well as Li(4) sites for Li ions [26]. It was also found that Li ions in $Li_{3.5}Ge_{0.5}P_{0.5}S_4$ can be located at Li(3) and Li(4).

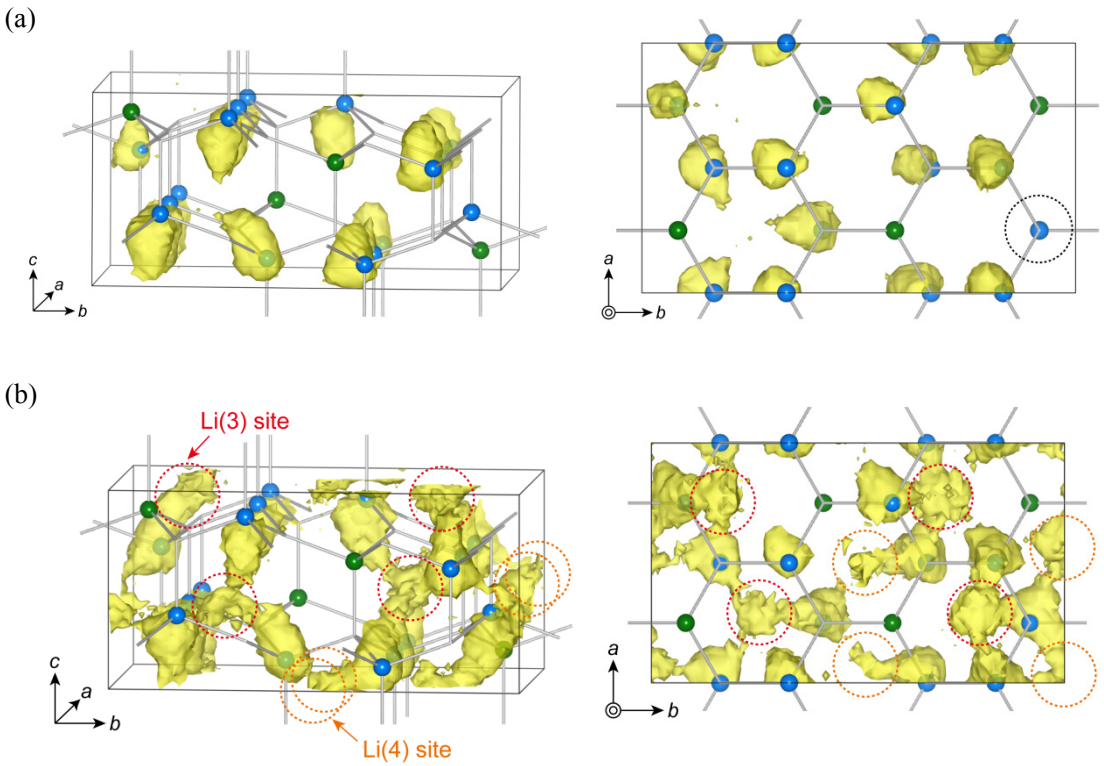

Figure 3.12. Perspective view and projection view down the *c* axis of Li-ion density distribution during the 20 ps FPMD simulations at 1600 K for (a) Li_2ZnGeO_4 and (b) $Li_3Zn_{0.5}GeO_4$. Isosurface shows 40 ($1/Å^3$ × volume of the unit cell). The blue balls denote Li or Zn ions. The green balls denote Ge ions. The Li-ion density of the site which is denoted by a broken black circle in the panel (a) is almost zero because only Zn ions occupy this site in the computational cell. The red and orange broken circles denote Li(3) and Li(4) sites in the panel (b).

(a)

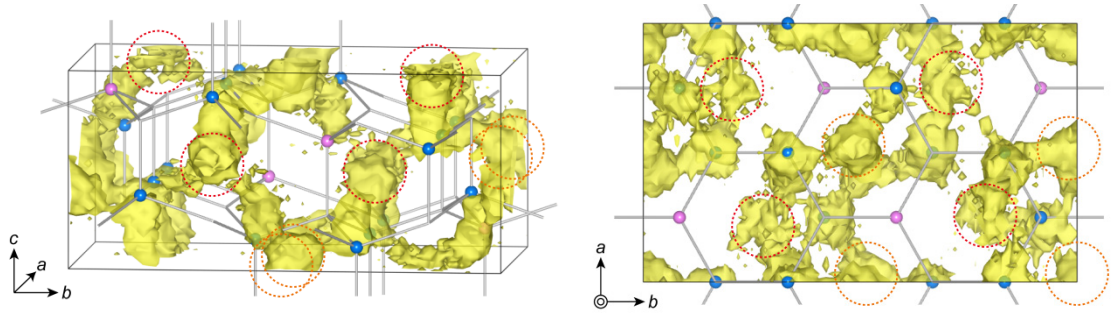

(b)

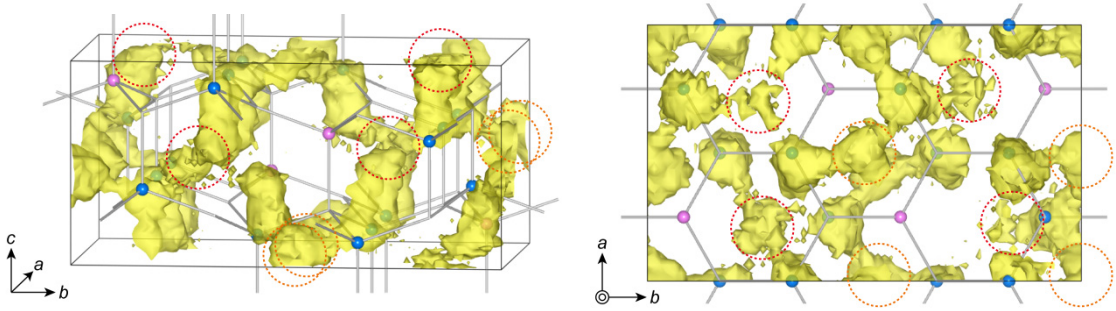

Figure 3.13. Perspective view and projection view down the *c* axis of Li-ion density distribution during the 20 ps FPMD simulation at 900 K for (a) Li_3PS_4 and (b) $Li_{3.5}Ge_{0.5}P_{0.5}S_4$. Isosurface shows 40 ($1/Å^3$ × volume of the unit cell). The blue balls denote Li ions. The pink balls denote P or Ge ions. The red and orange broken circles denote Li(3) and Li(4) sites.

In order to quantitatively analyze Li-ion density distributions, we evaluated occupancy of Li-ion site. We performed a nonlinear least squares fitting of the Li-ion density distribution to the sum of spherical Gaussian functions centered at Li(1), Li(2), Li(3) and Li(4) [54]. Since no Li-ion density was found at Li(5) and Li(6), Gaussian functions centered at those sites are not taken account. Although the Li-ion distribution shape is expected to be an ellipsoid, we roughly assumed it as spherical to improve convergence of a nonlinear fitting. The fitting function $f(\mathbf{r})$ at position $\mathbf{r}$ is expressed as

$$f(\mathbf{r}) = \sum_{i=1}^{4}\sum_{j=1}^{N_i} \frac{g_i}{\left(2\pi\sigma^2\right)^{3/2}} \exp\left[-\frac{\mathbf{r}-\mathbf{r}_{i,j}}{2\sigma^2}\right],$$

where g_i corresponds to the Li-ion occupancy of Li(i) site ($0 \le g_i \le 1$), and σ is the variance of the Gaussian and was assumed to be common for every site. N_i denotes the number of Li(i) site in a γ-unit cell. N_i for $i = 1 \sim 4$ is 8, 4, 4 and 4, respectively. Since the total number of Li ions per a γ-unit cell of $Li_{2+2x}Zn_{1-x}GeO_4$ is $4(2+2x)$, g_i satisfies the equation, $\sum_{i=1}^{4} N_i g_i = 4(2+2x)$. $\mathbf{r}_{i,j}$ denotes the coordinate of the j-th Li(i) site. The coordinates of the representative point for Li(i) site are $\mathbf{r}_1 = (x_1, y_1, z_1)$, $\mathbf{r}_2 = (0.25, y_2, z_2)$, $\mathbf{r}_3 = (0.25, y_3, z_3)$ and $\mathbf{r}_4 = (0, 0, 0.5)$, respectively. Therefore, 11 unknown parameters, g_1, g_2, g_3, σ, x_1, y_1, z_1, y_2, z_2, y_3, z_3, are optimized.

The number of Li ions at each Li site within a unit cell was estimated from the optimized occupancies g_i and is listed in Table 3.3. For $Li_{2+2x}Zn_{1-x}GeO_4$, the numbers of Li ions at tetrahedral and octahedral sites are nearly equal to $4(2+x)$ and $4x$, respectively. The numbers of Li ions at both Li(3) and Li(4) increase with increasing x. The number of Li ions at Li(3) is larger than that at Li(4). The neutron diffraction data show that the occupancy of tetrahedral sites is unity at room temperature [24]. The FPMD results also indicate that the tetrahedral sites are almost fully occupied by cations at 1600 K, since Zn ions can be found at only tetrahedral sites and the number of Zn ions per a unit cell is $4(1-x)$. Since tetrahedral sites are fully occupied, Li ions at octahedral sites mainly contribute to ionic conduction.

For $Li_{3+x}Ge_xP_{1-x}O_4$, the number of Li ions at each site is quite similar to $Li_{2+2x}Zn_{1-x}GeO_4$ as shown in Table 3.3. On the other hand, for $Li_{3+x}Ge_xP_{1-x}S_4$, the number of vacancies at tetrahedral

sites is much larger than oxides and increases with decreasing x. The number of Li ions at octahedral sites is approximately four and almost independent of x. The number of Li ions at Li(4) is about three times more than that of Li(3). These results are consistent with the trend of diffraction data that Li(4) is identified in Li_4GeS_4 [13] and Li_3PS_4 [26].

Table 3.3. The number of Li ions at tetrahedral and octahedral sites per a γ-unit cell containing four formula units for $Li_{2+2x}Zn_{1-x}GeO_4$ at 1600 K, $Li_{3+x}Ge_xP_{1-x}O_4$ at 1600 K and $Li_{3+x}Ge_xP_{1-x}S_4$ at 900 K. N_{Li} denotes the total number of Li ions per a γ-unit cell.

	x	N_{Li}	Tetrahedral	Octahedral		
			Li(1) + Li(2)	Li(3) + Li(4)	Li(3)	Li(4)
$Li_{2+2x}Zn_{1-x}GeO_4$	0.25	10	8.95	1.05	0.74	0.31
	0.50	12	10.03	1.96	1.29	0.68
	0.75	14	10.65	3.35	2.30	1.06
	1.00	16	11.63	4.37	2.24	2.12
$Li_{3+x}Ge_xP_{1-x}O_4$	0.25	13	11.49	1.51	0.94	0.57
	0.50	14	11.52	2.48	1.61	0.87
	0.75	15	11.64	3.36	1.98	1.38
	1.00	16	11.63	4.37	2.24	2.12
$Li_{3+x}Ge_xP_{1-x}S_4$	0.00	12	7.67	4.33	1.28	3.05
	0.25	13	8.73	4.26	1.14	3.13
	0.50	14	10.05	3.95	0.96	2.99
	0.75	15	10.58	4.42	1.03	3.38
	1.00	16	11.03	4.97	1.07	3.90

Due to absence of cations at tetrahedral sites in $Li_{3+x}Ge_xP_{1-x}S_4$, Li ions can diffuse by not only the cooperative mechanism but also "the single mechanism" shown in Figure 3.14. In this single mechanism, a Li ion at a tetrahedral site moves to a neighboring octahedral site or a Li ion at an octahedral site moves to a neighboring tetrahedral site. If Li ions diffuse by only the cooperative mechanism like $Li_{2+2x}Zn_{1-x}GeO_4$, the conduction carrier is a pair of Li ions. Therefore, the carrier concentration is approximately x per formula unit. In contrast, since the conduction carrier of the single mechanism in $Li_{3+x}Ge_xP_{1-x}S_4$ is a single Li ion, the carrier concentration is approximately $3 + x$ per formula unit. This difference of carrier concentration makes a significant contribution to the difference between the ionic conductivities of sulfides and those of oxides. As shown in Figure 3.11, the diffusion coefficient of $Li_{3+x}Ge_xP_{1-x}S_4$ with γ-Li_3PO_4 structure decreases with increasing x. This trend opposite to oxides can be roughly explained by the single mechanism. For $Li_{3+x}Ge_xP_{1-x}S_4$, the number of vacancies at tetrahedral sites decreases with increasing x. This decreasing interferes Li-ion migration from an octahedral site to a neighboring tetrahedral site. As a result, with increasing x, the diffusion coefficient decreases in spite of increasing carrier concentration.

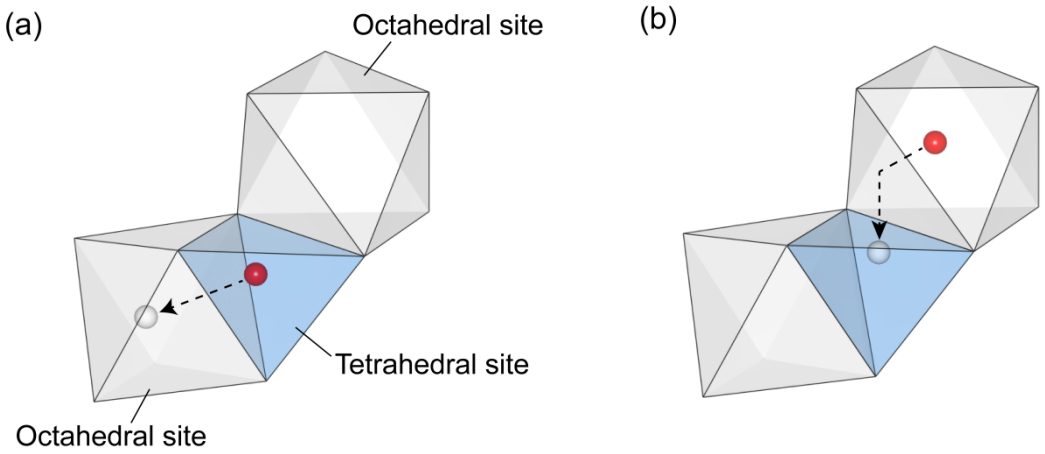

Figure 3.14. Single mechanisms proposed for $Li_{3+x}Ge_xP_{1-x}S_4$. The red and white balls denote Li ions at the initial and final state, respectively. (a) a Li ion at a tetrahedral site moves to a neighboring octahedral site. (b) a Li ion at an octahedral site moves to a neighboring tetrahedral site.

3. 4. Conclusions

First, energy barriers of Li-ion migration paths in $Li_3Zn_{0.5}GeO_4$, $Li_{3.5}Ge_{0.5}P_{0.5}O_4$ and $Li_{3.5}Ge_{0.5}P_{0.5}S_4$ with the γ-Li_3PO_4 structure were evaluated using the NEB method based on first-principles calculations. Major results are as follows:

1. In $Li_3Zn_{0.5}GeO_4$ and $Li_{3.5}Ge_{0.5}P_{0.5}O_4$, the most stable interstitial site is Li(3) and the second stable one is Li(4). In $Li_{3.5}Ge_{0.5}P_{0.5}S_4$, the most stable one is Li(4) and the second stable one is Li(3).

2. We proposed two kinds of migration mechanisms. In the interstitial mechanism, an excess Li ion at an octahedral site moves to another octahedral site. In the cooperative mechanism, an excess Li ion at an octahedral site moves to a neighboring tetrahedral site and the Li ion at the tetrahedral site simultaneously moves to another neighboring octahedral site. Energy barrier of the interstitial mechanism is much higher than that of the cooperative one in the oxides as well as the sulfide. We infer that Li ions diffuse mainly by the cooperative mechanism.

Next, Li-ion diffusion behaviors at high temperatures over 800 K in $Li_{2+2x}Zn_{1-x}GeO_4$ ($0 \leq x \leq 1$), $Li_{3+x}Ge_xP_{1-x}O_4$ ($0 \leq x \leq 1$) and $Li_{3+x}Ge_xP_{1-x}S_4$ ($0 \leq x \leq 1$) were computed using the FPMD simulations within the *NVT* ensemble. Major results are as follows:

1. The electronic charge density was decomposed into atomic contributions using the Bader analysis. The Li charge states of all solid solution are almost the same, from +0.87 to +0.89. On the other hand, the charge states of Ge and P in $Li_{3+x}Ge_xP_{1-x}S_4$ are considerably smaller than those in $Li_{3+x}Ge_xP_{1-x}O_4$. This means that the chemical bonding character between Ge or P and anions in sulfides is more covalent than that in oxides.

2. All ions except Li ions hardly move and the γ-Li_3PO_4 structure is maintained during the FPMD simulations.

3. Extrapolation of the calculated Li-ion diffusion coefficients to lower temperatures and their temperature dependence approximately fit with experimental ones for x = 0.50 and 0.75 in

$Li_{2+2x}Zn_{1-x}GeO_4$. This implies that the Li-ion conduction mechanism is the same over two temperatures regions.

4. $Li_{3+x}Ge_xP_{1-x}S_4$ exhibit larger Li-ion diffusion coefficients by about one order of magnitude than $Li_{3+x}Ge_xP_{1-x}O_4$.

5. The Li-ion density distribution showed that Li ions move between a tetrahedral site and an octahedral site. This supports occurrence of the cooperative mechanism involving a pair of two Li ions.

6. Tetrahedral sites are fully occupied in oxides, while vacancies form at tetrahedral sites in sulfides. Therefore, in sulfides, Li ions can migrate by not only the cooperative mechanism but also the single mechanism. In the single mechanism, a Li ion at a tetrahedral site moves to a neighboring octahedral site or a Li ion at an octahedral site moves to a neighboring tetrahedral site. Occurrence of both migration mechanisms results in an increase in the carrier concentration, and hense an increase in the ionic conductivity.

7. In $Li_{3+x}Ge_xP_{1-x}S_4$, the number of vacancies at tetrahedral sites decreases with increasing Li content. This decreasing interferes Li-ion migration from an octahedral site to a neighboring tetrahedral site. It is surmised that this is why Li-ion diffusion coefficient decreases with increasing Li content.

References

[1] A. D. Robertson, A. R. West and A. G. Ritchie, *Solid State Ionics* **104** (1997) 1-11.

[2] P. Knauth, *Solid State Ionics* **180** (2009) 911-916.

[3] J. W. Fergus, *J. Power Sources* **195** (2010) 4554-4569.

[4] H. Y-P. Hong, *Mat. Res. Bull.* **13** (1978) 117-124.

[5] P. G. Bruce and A. R. West, *Mat. Res. Bull.* **15** (1980) 379-385.

[6] H. Aono, E. Sugimoto, Y. Sadaoka, N. Imanaka and G. Adachi, *J. Electrochem. Soc.* **136** (1989) 590-591.

[7] K. Arbi, J. M. Rojo, J. Sanz, *J. Eur. Ceram. Soc.* **27** (2007) 4215-4218.

[8] Y. Inaguma, C. Liquan, M. Itoh, T. Nakamura, T. Uchida, H. Ikuta and M. Wakihara, *Solid State Commun.* **86** (1993) 689-693.

[9] Y. Harada, T. Ishigaki, H. Kawai and J. Kuwano, *Solid State Ionics* **108** (1998) 407-413.

[10] R. Murugan, V. Thangadurai and W. Weppner, *Angew. Chem. Int. Ed.* **46** (2007) 7778-7781.

[11] R. Kanno, T. Hata, Y. Kawamoto and M. Irie, *Solid State Ionics* **130** (2000) 97-104.

[12] R. Kanno and M. Murayama, *J. Electrochem. Soc.* **148** (2001) A742-A746.

[13] M. Murayama, R. Kanno, M. Irie, S. Ito, T. Hata, N. Sonoyama and Y. Kawamoto, *J. Solid State Chem.* **168** (2002) 140-148.

[14] M. Tatsumisago, F. Mizuno and A. Hayashi, *J. Power Sources* **159** (2006) 193-199.

[15] T. Minami, A. Hayashi and M. Tatsumisago, *Solid State Ionics* **177** (2006) 2715-2720.

[16] K. Minami, A. Hayashi, S. Ujiie and M. Tatsumisago, *J. Power Sources* **189** (2009) 651-654.

[17] N. Kamaya, K. Homma, Y. Yamakawa, M. Hirayama, R. Kanno, M. Yonemura, T. Kamiyama, Y. Kato, S. Hama, K. Kawamoto and A. Mitsui, *Nat. Mater.* **10** (2011) 682–686.

[18] Y-W. Hu, I. D. Raistrick and R. A. Huggins, *J. Electrochem. Soc.* **124** (1977) 1240-1242.

[19] A. Khorassani and A. R. West, *Solid State Ionics* **7** (1982) 1-8.

[20] A. Khorassani and A. R. West, *J. Solid State Chem.* **53** (1984) 369-375.

[21] A. R. Rodger, J. Kuwano and A. R. West, *Solid State Ionics* **15** (1985) 185-198.

[22] A. Garcia, G. Torres-Trevino and A. R. West, *Solid State Ionics* **40-41** (1990) 13-17.

[23] C. K. Lee and A. R. West, *J. Mater. Chem.* **3** (1993) 191-196.

[24] a) I. Abrahams, P. G. Bruce, A. R. West and W. I. F. David, *J. Solid State Chem.* **75** (1988) 390-396; b) I. Abrahams, P. G. Bruce, I. F. David and A. R. West, *Acta Cryst.* **B45** (1989) 457-462.

[25] P. G. Bruce and A. R. West, *Mat. Res. Bull.* **15** (1980) 379-385.

[26] K. Homma, M. Yonemura, T. Kobayashi, M. Nagao, M. Hirayama and R. Kanno, *Solid State Ionics* **182** (2011) 53-58.

[27] H. Jónsson, G. Mills and K. W. Jacobsen, in *Classical and Quantum Dynamics in Condensed Phase Simulations*, edited by B. J. Berne, G. Ciccotti and D. F. Coker (World Scientific, Singapore, 1998), pp. 385-404.

[28] I. Kishida, Y. Koyama, A. Kuwabara, T. Yamamoto, F. Oba and I. Tanaka, *J. Phys. Chem. B* **110** (2006) 8258-8262.

[29] Y. A. Du and N. A. W. Holzwarth, *Phys. Rev. B* **76** (2007) 174302.

[30] K. Toyoura, Y. Koyama, A. Kuwabara, F. Oba and I. Tanaka, *Phys. Rev. B* **78** (2008) 214303.

[31] a) Y. Mo, S. P. Ong and G. Ceder, *Chem. Mater.* **24** (2012) 15-17; b) S. P. Ong, Y. Mo, W. D. Richards, L. Miara, H. S. Lee and G. Ceder, *Energy Environ. Sci.* **6** (2013) 148-156.

[32] M. Xu, J. Ding and E. Ma, *Appl. Phys. Lett.* **101** (2012) 031901.

[33] P. Hohenberg and W. Kohn, *Phys. Rev.* **136** (1964) B864-B871.

[34] W. Kohn and L. J. Sham, *Phys. Rev.* **140** (1965) A1133-A1138.

[35] P. E. Blöchl, *Phys. Rev. B* **50** (1994) 17953-17979.

[36] G. Kresse and J. Hafner, *Phys. Rev. B* **48** (1993) 13115-13118.

[37] G. Kresse and J. Furthmüller, *Phys. Rev. B* **54** (1996) 11169-11186.

[38] G. Kresse and D. Joubert, *Phys. Rev. B* **59** (1999) 1758-1775.

[39] J. P. Perdew, K. Burke and M. Ernzerhof, *Phys. Rev. Lett.* **77** (1996) 3865-3868.

[40] J. Zemann, *Acta Cryst.* **13** (1960) 863-867.

[41] K. Momma and F. Izumi, *J. Appl. Cryst.* **41** (2008) 653-658.

[42] S. Nosé, *J. Chem. Phys.* **81** (1984) 511-519.

[43] E. Plattner, H. Völlenkle and A. Wittmann, *Monatsh. Chem.* **107** (1976) 921-927.

[44] C. Keffer, A. Mighell, F. Mauer, H. Swanson and S. Block, *Inorg. Chem.* **6** (1967) 119-125.

[45] H. Völlenkle and A. Wittmann, *Naturwissensch.* **54** (1967) 441.

[46] G. Henkelman, A. Arnaldsson and H. Jónsson, *Comput. Mater. Sci.* **36** (2006) 354-360.

[47] E. Sanville, S. D. Kenny, R. Smith and G. Henkelman, *J. Comput. Chem.* **28** (2008) 899-908.

[48] W. Tang, E. Sanville and G. Henkelman, *J. Phys.: Condens. Matter* **21** (2009) 084204.

[49] S. Takai, K. Kurihara, K. Yoneda, S. Fujine, Y. Kawabata and T. Esaka, *Solid State Ionics* **171** (2004) 107-112.

[50] M. A. K. L. Dissanayake, R. P. Gunawardane, H. H. Sumathipala and A. R. West, *Solid State Ionics* **76** (1995) 215-210.

[51] K. Fujimura, A. Seko, Y. Koyama, A. Kuwabara, I. Kishida, K. Shitara, C. A. J. Fisher, H. Moriwake and I. Tanaka, *Adv. Energy Mater.* (2013), DOI: 10.1002/aenm.201300060.

[52] E. I. Burmakin and G. Sh. Shekhtman, *Russ. J. Electrochem.* **46** (2010) 243-246.

[53] M. Tachez, J.-P. Malugani, R. Mercier and G. Robert, *Solid State Ionics* **14** (1984) 181-185.

[54] A. Seko, Y. Koyama, A. Matsumoto and I. Tanaka, *J. Phys.: Condens. Matter* **24** (2012) 475402.

Chapter 4

Accelerated Materials Design of Lithium Superionic Conductors Based on First-Principles Calculations and Machine Learning Algorithms

4. 1. Introduction

Lithium-conducting oxides in the system $LiO_{1/2}$-$AO_{m/2}$-$BO_{n/2}$ (where m and n denote the formal valences of cations A and B, respectively), known as LISICONs and corresponding to general formula $Li_{8-c}A_aB_bO_4$ (where $c = ma + nb$) [1], have been intensively studied since the 1970s. The original LISICON composition, $Li_{3.5}Zn_{0.25}GeO_4$, was reported to exhibit an ionic conductivity of over 10^{-1} S cm^{-1} at 673 K [2], and stimulated a flurry of new research. Although the conducting properties of many different LISICONs have since been reported by various groups, there are still many compositions that have yet to be synthesized, let alone characterized. In some cases, results from different groups also vary considerably [2-6]. An Arrhenius plot of Li-ion conductivity summarizing previous experimental data is provided as Figure 4.1. Given the urgent need for improved energy storage and power devices, a more efficient means of designing ionic conductors based on a reproducible and systematic methodology is an imperative for future progress in this field.

Thanks to astonishing improvements in computer performance and computational techniques, first-principles calculations based on density functional theory (DFT) are now used routinely for quantitative analysis of ionic conduction in crystals. Combination of DFT calculations with high-throughput and machine-learning techniques is now also considered a viable means of searching for novel lithium battery materials [7-9]. For compounds with simple chemistry and structure, the saddle point associated with an ionic jump, from which the activation barrier energy can be extracted in a straightforward manner, is readily calculated. Such methods have already been applied to several Li-battery materials, e.g., $LiCoO_2$ [10], $LiFePO_4$ [11], TiO_2-B [12], and graphite

[13]. The nudged elastic band (NEB) method is popular for such a purpose [9,14-16]. The effective frequency term for the ionic jump used in the calculation of ion diffusivity can also be computed from first-principles if desired [13]. When it comes to compounds with more complicated structures, such as are typical in LISICON solid electrolytes, the search for saddle points along convoluted migration paths, often involving complex migration mechanisms, (e.g, cooperative mechanisms [17,18]), becomes a non-trivial task. When the compound is a solid solution composed of multiple elements, this becomes even more difficult because of the huge variety of chemical environments that migrating ions encounter. LISICON represents a sobering example of both kinds of complexity. In such cases, the first-principles molecular dynamics (FPMD) approach is an attractive alternative [11,18-20], since it does not require an *a priori* specification of the migration pathway or mechanism for the ionic self-diffusion to be probed.

In this study, we first performed the FPMD simulations for $Li_{2+2x}Zn_{1-x}GeO_4$ ($0 \leq x \leq 1$) to calculate Li-ion conductivities at high temperatures. The phase transition point at lower temperatures was also estimated using first-principles calculations based on the cluster expansion method. Next, these first-principles studies were systematically applied to a diverse range of LISICON-based compounds. Then, in order to predict their low-temperature ionic conductivities, a machine-learning technique using theoretical and experimental datasets was proposed.

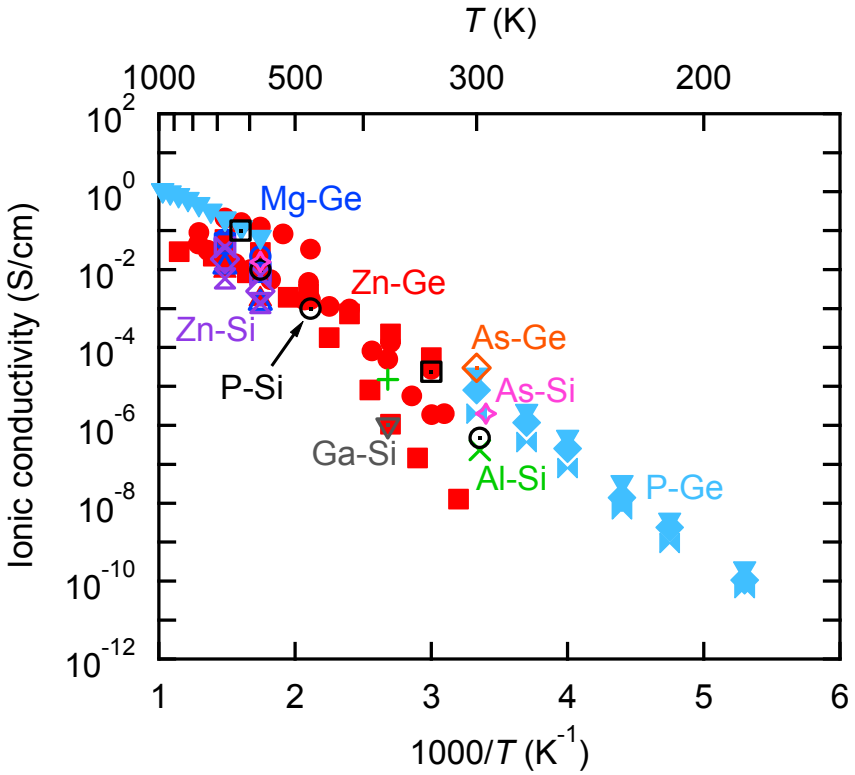

Figure 4.1. Arrhenius plots of experimental conductivity data for $Li_{8-c}A_aB_bO_4$ ($c = ma + nb$, m = charge of cation A, and n = charge of cation B), for various combination of $A = Zn^{2+}$, Mg^{2+}, Al^{3+}, Ga^{3+}, P^{5+} and As^{5+}, or $B = Si^{4+}$ or Ge^{4+}.

4. 2. Computational Methods

4. 2. 1. The DFT Calculations

The electronic structure calculations throughout this study were performed using the projector augmented-wave method [21,22] with the generalized gradient approximation [23], as implemented in the VASP code [24]. The plane-wave cutoff energy was 300 eV, and the total energy convergence was better than 10^{-2} meV per cell. Integration in reciprocal space was performed at the Γ-point only.

4. 2. 2. The FPMD Simulations

The FPMD simulations were systematically carried out within the *NVT* ensemble using the thermostat of Nosé [25]. The volume and shape of the cell were held fixed. We used the lattice volume at zero temperature calculated by DFT and neglected any contributions from thermal expansion. The simulation cells were constructed from 2 × 1 × 2 unit cells of the original γ structure, and contained between 128 and 176 atoms. In order to model disordered solid solutions, Zn and Li ions were distributed randomly over tetrahedral and octahedral sites in the initial structure. Since the average distance between neighboring tetrahedral and octahedral Li sites is 0.2 nm, the MD time required for the corresponding ionic jump is $t \sim 20$ ps when the diffusivity is $D \sim 10^{-9}$ m^2/s using the formula of $\langle r^2 \rangle = 6Dt$, where $\langle r^2 \rangle$ is the mean square displacement of individual ions. This gives a rough estimate of the lowest diffusivity we can calculated for a simulation time of 20 ps. The time step was set to 2 fs and calculations were performed for 12,500 steps, i.e., 25 ps, in total, except for the case of the 1200 K calculation, which was carried out for 45 ps. The first 2500 steps, corresponding to 5 ps, were treated as a thermal equilibrium stage and discarded before analyzing the diffusion coefficient. Diffusion coefficients were found to converge to within 1×10^{-9} m^2/s for different simulation times and choice of the initial structure.

4. 2. 3. Estimation of Phase Transition Temperature

As we will discuss in Section 4.3.1, in the case of LISICON, the deflection point in the Arrhenius plot of ion conductivity has been ascribed to a phase transition [5]. However, the

structural changes associated with this transition are largely unknown. We assume that the deflection point corresponds to ordering and disordering of Li ions on octahedral sites, since the mechanism of Li-ion conduction via octahedral sites seems to alter at this point. To check whether this is indeed the case, the phase transition temperature, T_c, was estimated by determining the point at which the free energies of ordered and disordered phases are equal, based on DFT calculations.

Ordered structures were investigated using a cluster-expansion-type method. Distributions of *A* and *B* cations were obtained by simulated annealing (SA) with a simplified point-charge model. Details of the SA are provided as Appendix (Section 4.5.1). Even when the framework cations are positioned on their experimentally determined sites, a number of different Li configurations can be constructed for a given stoichiometry. We first identified those ordered structures for which the energy is an extremum (maximum or minimum) [26,27]. These structures have correlation functions with large root mean squares computed within the formalism of the cluster expansion method. The minimum energy was taken as the energy of the ground-state configuration for a given composition. Next, the energy of a disordered structure for a given composition was estimated by averaging the energies of 20 randomly-chosen 2 × 1 × 2 supercells with different octahedral Li ion configurations. The entropy difference between ordered and disordered phases per octahedral site was calculated using the point approximation $T\Delta S = -k_B T\left[x\ln x + (1-x)\ln(1-x)\right]$, where k_B and x are the Boltzmann constant and Li occupancy of octahedral sites, respectively. At the transition temperature, T_c, ΔE is equal to $T_c\Delta S$, where ΔE is the difference between the energy of the disordered structure and the lowest energy of the ordered structures. The formation energy, $E^{mix}{}_0$, and free energy of mixing at 1200 K, $F^{mix}{}_{1200}$, are the energy of an ordered structure and free energy of the disordered structure, respectively, which are calculated from the energies / free energies of end-member compositions with the γ structure.

4. 3. Results and Discussion

4. 3. 1. $Li_{2+2x}Zn_{1-x}GeO_4$

We first carried out systematic FPMD simulations of compositions $Li_{2+2x}Zn_{1-x}GeO_4$ (x = 0.25, 0.50 and 0.75) at four temperatures assuming the γ structure. Figure 4.2 shows the calculated Li-ion diffusion coefficients for the three compositions as a function of inverse temperature. For comparison, diffusion coefficients extracted from experimental ionic conductivities [2,28] according to the Nernst-Einstein equation are also shown. Extrapolation of the calculated diffusion coefficients and their temperature dependence for $Li_{3.5}Zn_{0.25}GeO_4$ to lower temperature fits well with experimental values measured between 523 and 673 K [2]. At temperatures lower than 523 K, however, the experimental activation energy increases, indicative of a change in migration mechanism. A simple extrapolation of the high temperature data to temperatures below 523 K is thus inappropriate in this case. In order to predict the low-temperature conductivity for a wide variety of compositions, a more rigorous (or comprehensive) methodology is required. We note in this regard that FPMD has been used recently to predict Li-ion conductivity at high temperatures in other structure types [29], but not the low temperature conductivity behavior.

The phase transition temperature, T_c, was estimated by determining the point at which the free energies of ordered and disordered phases are equal. Calculated T_cs for the γ phase of four compositions in the pseudobinary Li_2ZnGeO_4-Li_4GeO_4 are plotted in Figure 4.3(a). The estimated T_cs are 1150 K for $Li_{2.5}Zn_{0.75}GeO_4$, 750 K for $Li_3Zn_{0.5}GeO_4$, and 380 K for $Li_{3.5}Zn_{0.25}GeO_4$, indicating a remarkable decrease with decreasing Zn content. Although it is overly ambitious to expect quantitative reproduction of T_cs by such a simple method, the trend is consistent with the experimental results in Figure 4.2.

The formation energy in the ground state, E^{mix}_0, is a good measure of whether a chemical system will form a solid solution or not. Values of E^{mix}_0 for the pseudobinary Li_2ZnGeO_4-Li_4GeO_4 system relative to those of the two end-members, γ-Li_2ZnGeO_4 and γ-Li_4GeO_4, are plotted in Figure 4.3(b). Relative energies of experimentally known structures β-Li_2ZnGeO_4 [30] and α-Li_4GeO_4 [31] are also included for comparison. Formation energies of different solute configurations were computed for both α and β phases. We found that the configurations reported in References [30] and

[31] correspond to the lowest energies.

The results in Figure 4.3(b) imply a preference for phase separation of β-Li_2ZnGeO_4 and α-Li_4GeO_4 at low temperatures, which is consistent with the phase diagram in Figure 1.2. The free energy of mixing for the disordered γ phase at 1200 K, F^{mix}_{1200}, is also plotted in Figure 4.3(b). Here, only the configuration entropy of Li over octahedral sites in the γ phase is taken into account, which is zero for γ-Li_2ZnGeO_4, since Li ions only occupy tetrahedral sites in this case. While the tendency for the disordered γ phase to become more stable at elevated temperature can be understood intuitively, a quantitative estimation of the phase diagram requires more detailed theoretical analysis, such as phonon calculations to estimate vibrational free energies, and a cluster expansion technique to take into account configuration terms, which are beyond the scope of the present study.

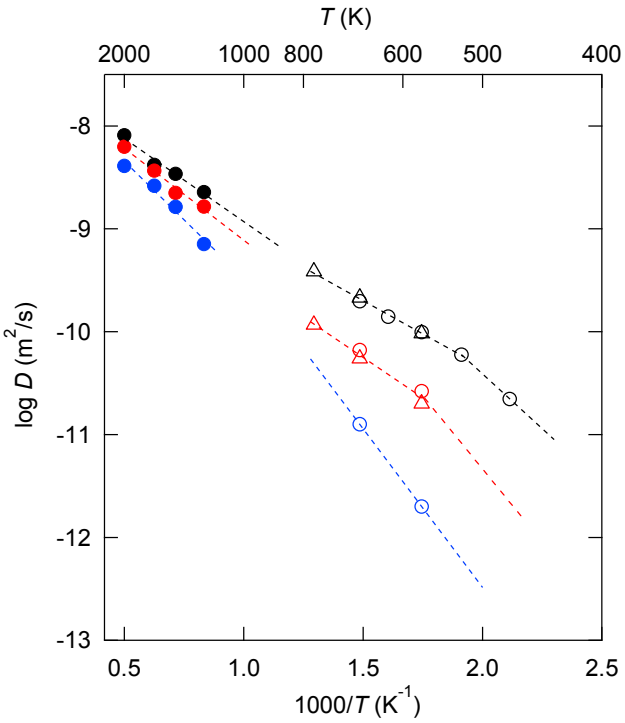

Figure 4.2. Arrhenius plots of calculated Li-ion diffusion coefficients for $Li_{2+2x}Zn_{1-x}GeO_4$ (x = 0.25, 0.50 and 0.75). Blue, red and black closed circles are for x = 0.25, 0.50 and 0.75, respectively. Experimental data, shown as open circles [2] and open triangles [28], are provided for comparison. Note that the extension to lower temperatures for x = 0.50 has a slope intermediate to that of x = 0.25 and x = 0.75 and is based on the reported deflection point of 550 K [6].

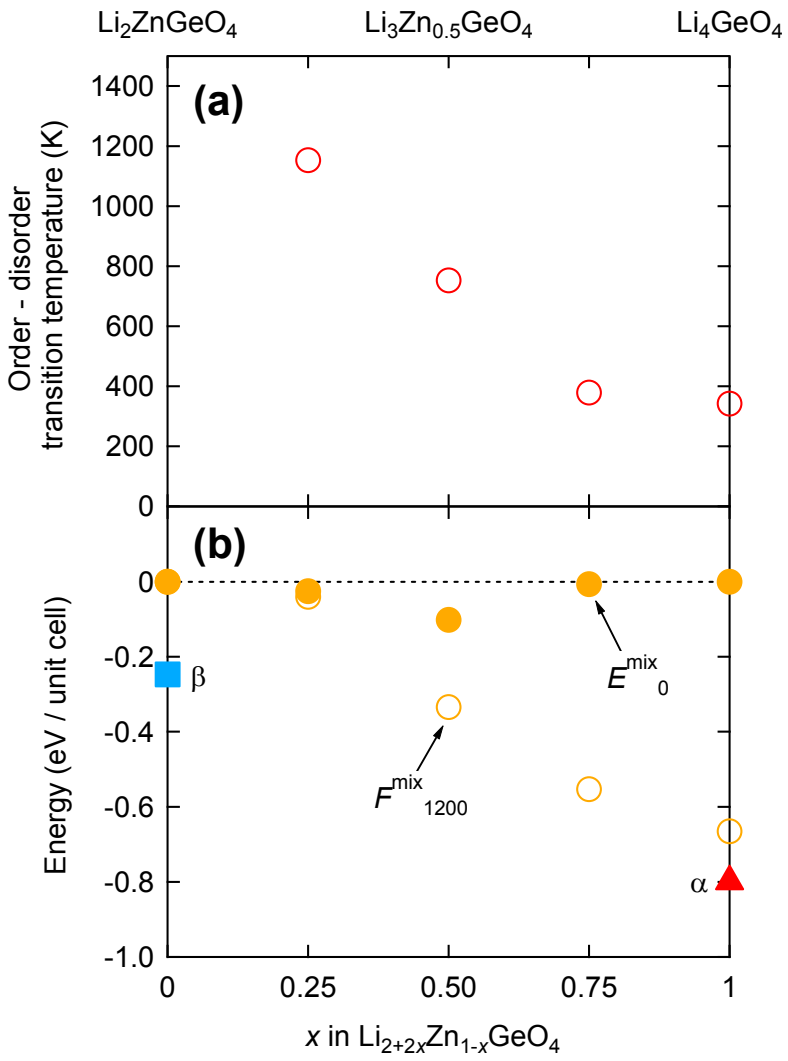

Figure 4.3. (a) Estimated T_cs for compositions with the γ structure in the pseudobinary Li_2ZnGeO_4-Li_4GeO_4. (b) Formation energies of structures in the ground state, E^{mix}_0, in the pseudobinary Li_2ZnGeO_4-Li_4GeO_4 relative to the two end-members γ-Li_2ZnGeO_4 and γ-Li_4GeO_4 (closed yellow circles). Open yellow circles show the free energy of mixing of disordered γ phases at 1200 K, F^{mix}_{1200}. Relative energies of experimentally known structures of β-Li_2ZnGeO_4 and α-Li_4GeO_4 are indicated by a blue square and red triangle, respectively, for comparison.

4. 3. 2. Systematic Evaluation of $Li_{8-c}A_aB_bO_4$

Since most LISICON oxides exhibiting high ionic conductivity are known to have the γ structure, we performed an extensive set of calculations of the system γ-$Li_{8-c}A_aB_bO_4$ (where $c = ma + nb$) for A corresponding to divalent Zn and Mg, trivalent Al and Ga, or pentavalent P and As, and B to tetravalent Si and Ge. Phase relationships between $Li_{8-c}A_aBO_4$, $Li_{8-c}AO_4$, and Li_4BO_4 are illustrated in the phase diagrams at the top of Figure 4.4. Calculations were performed for two kinds of solid solutions: the pseudobinary $Li_{8-c}A_aBO_4$-Li_4BO_4 (tie line 1) in which element A is substituted for Li in Li_4BO_4, and pseudobinary Li_4BO_4-$Li_{8-c}AO_4$ (tie line 2), in which A is substituted for B in Li_4BO_4. These permutations result in three different solid solution types, which we label II-IV, III-IV and V-IV based on the valence states of the corresponding A and B ions. FPMD simulations at 1600 K were performed for a total of 92 different compositions, and the results summarised in Figure 4.4. For $Li_{8-c}A_aB_bO_4$ with pentavalent A (V-IV), only Li_3AO_4-Li_4BO_4 solid solutions were considered, since substitution of Li by a pentavalent ion is energetically prohibitive. In addition to the FPMD simulations to determine the diffusivity at 1600 K, D_{1600}, first-principles calculations were performed systematically to determine T_c, the formation free energy of the solid solution at 1600 K, ΔF^S_{1600}, and the average volume of the disordered structures, V_{dis}. Note that the reference states for ΔF^S_{1600} are those of the end-members $x = 0$, $y = 1$ and $x = 1$, $y = 0$ with the lowest energy, in contrast to those in Figure 4.3(b). T_c, ΔF^S_{1600} and V_{dis} were calculated for 72 compositions, based on the number of permutations possible given the size of the simulation cell used. The total number of first-principles calculations required to estimate T_c and ΔF^S_{1600} was 2684.

Figure 4.4 shows that D_{1600} does not depend strongly on the choice of A and B. D_{1600} appears largely independent of V_{dis}, despite the widely held view that diffusivity increases with lattice volume. In γ-$Li_{8-c}A_aB_bO_4$, the average occupancy of Li ions on octahedral sites, p_{Oct}, can be calculated from $p_{Oct} = [(8 - c + a + b) - 4] / 4$. p_{Oct} seems to be the principal factor determining the magnitude of the diffusivity for both tie line 1 and tie line 2 compositions when A is pentavalent. However, this does not appear to be the case for tie line 2 when A is divalent or trivalent.

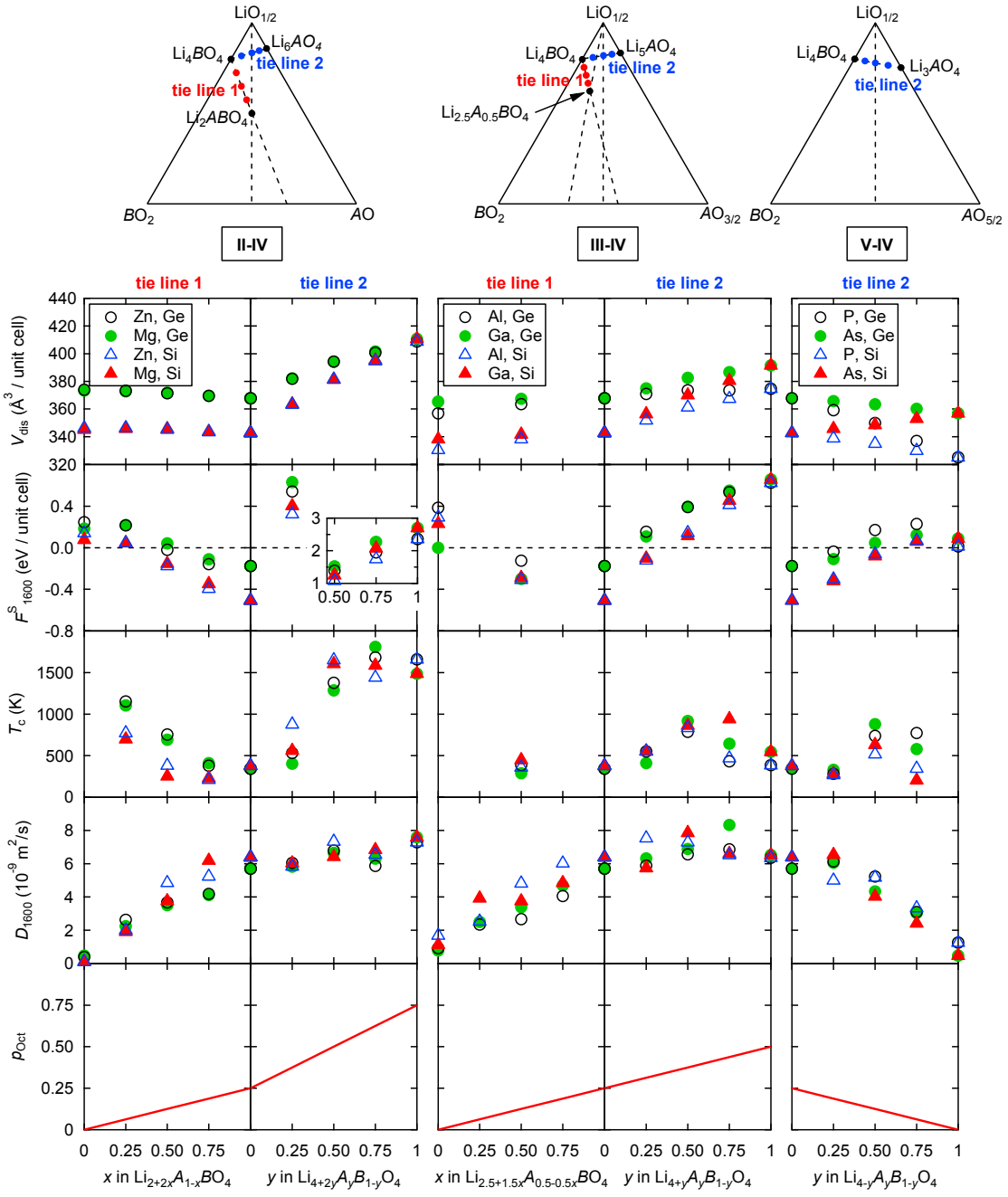

Figure 4.4. Diffusion coefficients at 1600 K, D_{1600}, transition temperatures, T_c, formation free energies of solid solutions at 1600 K, ΔF^{S}_{1600}, and average volume of disordered structures, V_{dis} as a function of chemical composition. D_{1600} was calculated from FPMD simulations, and T_c, ΔF^{S}_{1600} and V_{dis} from energy minimization calculations. The compositions are taken from tie lines 1 and 2 in the pseudobinary phase diagrams atop each plot for II-IV, III-IV and V-IV type systems. Elements *A* and *B* for each composition and their corresponding data markers are shown in the legends at the top of the V_{dis} plots. The change in p_{Oct} with composition is shown in the bottom panel.

4. 3. 3. Prediction of Low-Temperature Ionic Conductivities

High D_{1600} and low T_c are important factors for predicting good ionic conductivity. However, the DFT data alone are not yet sufficient for estimating the ionic conductivity reliably at low temperatures. Assuming that the theoretical data are complementary to and consistent with the experimental data, we applied a machine-learning technique to use both datasets in combination to predict low-temperature conductivities of the various compositions. As experimental data we used 95 conductivity measurements at different temperatures, which are plotted in Figure 4.1. The theoretical dataset was composed of the D_{1600}, T_c and V_{dis} values reported in Figure 4.4. These served as a training dataset in order to predict the ionic conductivity at 373 K, σ_{373}, using the support-vector regression (SVR) method with a Gaussian kernel [32]. The logarithm of ionic conductivity σ was taken as the dependent variable. For the independent variables, D_{1600}, T_c, V_{dis} and experimental temperature T were used. The significance values of the variables are given as Appendix (Section 4.5.2). The variance of the Gaussian kernel, the regularization constant and forms of independent variables were optimized by minimizing the prediction error estimated by the bootstrapping method [33]. The prediction error of the optimized SVR for log σ is 0.373. Variation of bootstrapping errors as a function of the independent variables is plotted in Figure 4.6 of Appendix.

Figure 4.5 shows the predicted σ_{373} for 72 compositions in which T_c and V_{dis} are available from Figure 4.4. Even though the theoretical datasets do not contain information about the activation energies explicitly, systems with high D_{1600} and low T_c tend to have high σ_{373} as expected. The conductivity of compounds with low Zn content such as $Li_{2+2x}Zn_{1-x}GeO_4$ (x = 0.75) with high D_{1600} and low T_c are greater than those with high Zn content, such as $Li_{2+2x}Zn_{1-x}GeO_4$ (x = 0.25), and high T_c. This result explains the trend observed by experimentalists, namely that the original LISICON composition $Li_{3.5}Zn_{0.25}GeO_4$ has one of the highest Li-ion conductivities. In this study, Li_4GeO_4 is predicted to have the highest σ_{373} of all 72 compounds. However, it has not yet been synthesized because it generally crystallizes in the α structure rather than γ structure. As seen in Figure 4.3(b), however, the difference in F^{mix}_{1200} for Li_4GeO_4 between α and γ is not expected to be large. If γ-Li_4GeO_4 can be successfully synthesised, our calculations predict it to exhibit an ionic conductivity at 373 K a few times higher than LISICON $Li_{3.5}Zn_{0.25}GeO_4$. Besides Li_4GeO_4, several other

compounds exhibit higher σ_{373} than the traditional LISICON with negative ΔF^{S}_{1600} values predicted. These are Li_4SiO_4, $Li_{2+2x}Zn_{1-x}SiO_4$ (for x = 0.5, 0.75), $Li_{3.5}Mg_{0.25}SiO_4$, $Li_{3.25}Al_{0.25}SiO_4$, $Li_{4.25}A_{0.25}Si_{0.75}O_4$ (A = Al or Ga), $Li_{3.5}A_{0.5}B_{0.5}O_4$ (A = P, and B = Si) and $Li_{3.75}A_{0.25}B_{0.75}O_4$ (A = P or As, and B = Ge or Si).

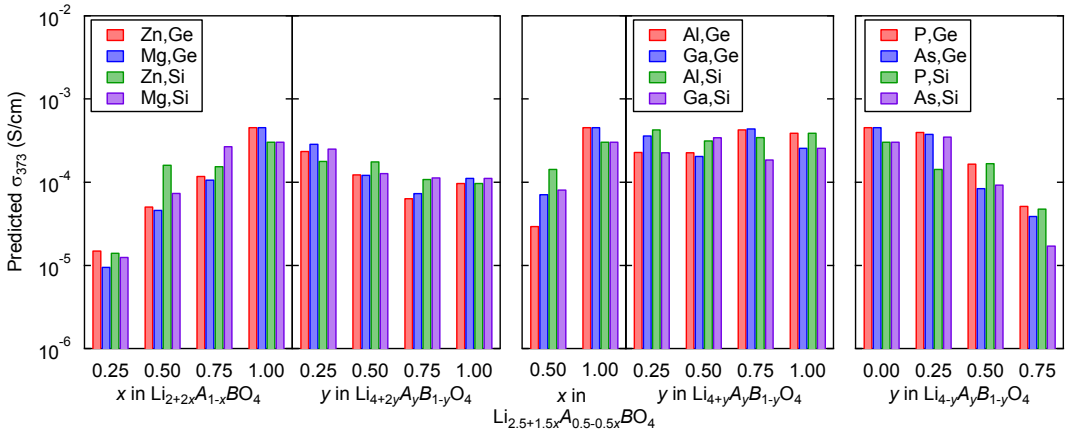

Figure 4.5. Predicted ionic conductivities at 373 K, σ_{373}, for 72 compositions in the system $Li_{8-c}A_aB_bO_4$, where A^{m+} = Zn, Mg, Al, Ga, P or As, and B^{n+} = Ge or Si, and $c = ma + nb$. Values of σ_{373} were obtained by iterative analysis of calculated datasets and experimental datasets.

4. 4. Conclusions

We aimed to establish a comprehensive method to predict low-temperature ionic conductivities for a diverse range of Li superionic conductors. Major results are as follows:

1. A deflection point, T_c, in the Arrhenius plot of ionic conductivity were estimated using first-principles calculations based on the cluster expansion method, assuming that the deflection point corresponds to ordering and disordering of excess Li ions on octahedral sites. Calculated T_c for γ-$Li_{2+2x}Zn_{1-x}GeO_4$ noticeably decreases with decreasing Zn content. This trend is consistent with the experimental results.

2. We proposed a machine-learning technique using theoretical data and experimental data in combination to predict low-temperature ionic conductivities of various compositions.

3. In order to obtain the theoretical data, an extensive set of first-principles calculations were carried out for LISICON-type oxide systems γ-$Li_{8-c}A_aB_bO_4$ (where $c = ma + nb$). Diffusion coefficient at 1600 K, D_{1600} does not depend strongly on the choice of cation A and B. D_{1600} has a correlation with the average Li occupancy on octahedral sites in the solid solutions in which Li content is smaller than four per formula unit.

4. In the machine-learning technique, the values of D_{1600}, T_c and average volume of the disordered structures were used as the theoretical dataset. 95 conductivity measurements were used as the experimental data.

5. Li_4GeO_4 is predicted to have the highest ionic conductivity at 373 K, σ_{373}, of all 72 compounds. If it crystallizes γ structure, our calculations predict it to exhibit σ_{373} a few times higher than the traditional LISICON $Li_{3.5}Zn_{0.25}GeO_4$.

4. 5. Appendix

4. 5. 1. Simulated Annealing for Determining Configurations of Cations *A* and *B*

We considered various atomic configurations of cations *A* and *B* on tetrahedral sites using simplified point charge models. In order to model a perfectly disordered Li configuration over octahedral sites, we placed equivalent point charges *q* on all octahedral sites, where *q* is the number of Li ions on the octahedral sites divided by the number of octahedral sites. For example, in the case of $Li_{3.5}Zn_{0.25}GeO_4$, q = +3/16. The placement of point charges of +4 (for Ge) and +2 (for Zn) over tetrahedral sites were then optimized using a simulated annealing procedure for all $Li_{8-c}A_aB_bO_4$. After determining the optimum cation configurations over the tetrahedral sites, we examined possible Li configurations over the octahedral sites. The number of independent Li configurations over octahedral sites in the unit cell of the γ structure was 933 and 12486 for the pseudobinary systems Li_2ZnGeO_4-Li_4GeO_4 and Li_4GeO_4-Li_6ZnO_4, respectively. (See Table 4.1 for details.)

Table 4.1. Number of independent Li configurations over octahedral sites within the unit cell of the γ structure.

(a) II - IV systems, tie line 1

x in $Li_{2+2x}A_{1-x}BO_4$	0.00	0.25	0.50	0.75	1.00	Total
Number of independent Li configurations	1	16	64	560	292	933

(b) II - IV systems, tie line 2

y in $Li_{4+2y}A_yB_{1-y}O_4$	0.00	0.25	0.50	0.75	1.00	Total
Number of independent Li configurations	292	4244	3414	4244	292	12486

(c) III - IV systems, tie line 1

x in $Li_{2.5+1.5x}A_{0.5-0.5x}BO_4$	0.00	0.25	0.50	0.75	1.00	Total
Number of independent Li configurations	1	-	120	-	292	413

(d) III - IV systems, tie line 2

y in $Li_{4+y}A_yB_{1-y}O_4$	0.00	0.25	0.50	0.75	1.00	Total
Number of independent Li configurations	292	2348	2150	6020	1814	12624

(e) V - IV systems, tie line 2

y in $Li_{4-y}A_yB_{1-y}O_4$	0.00	0.25	0.50	0.75	1.00	Total
Number of independent Li configurations	292	324	42	12	1	671

4. 5. 2. Prediction of Ionic Conductivity by Support Vector Regression (SVR)

In this study, in addition to D_{1600} and the experimental temperature, T, T_c and V_{dis} were considered as candidate independent variables for SVR. Figure 4.6 shows the prediction errors for SVR for four sets of independent variables, as estimated by the bootstrapping method. When both T_c and V_{dis} are included, the bootstrapping prediction error for log σ decreases slightly compared with the SVR performed only with D_{1600} and T. However, it is essential to include T_c and V_{dis} because without them the SVR cannot represent the deflection in the ionic conductivity curves seen in Figure 4.2. Figure 4.6, in which σ_{373} values predicted by two kinds of SVRs for $Li_{8-c}Zn_aGe_bO4$ are plotted as a function of composition, illustrates this situation. In the SVR using only D_{1600} and T, the composition dependence of σ_{373} is similar to that of D_{1600} in Figure 4.4 since information relating to the deflection comes from limited experimental data. The SVR with D_{1600}, T, T_c and V_{dis} can reproduce the ionic conductivity much better at low temperatures. Since T_c is much higher than 373 K for tie line 2, σ_{373} predicted by SVR using D_{1600}, T, T_c and V_{dis} is lower than that predicted by SVR using only D_{1600} and T.

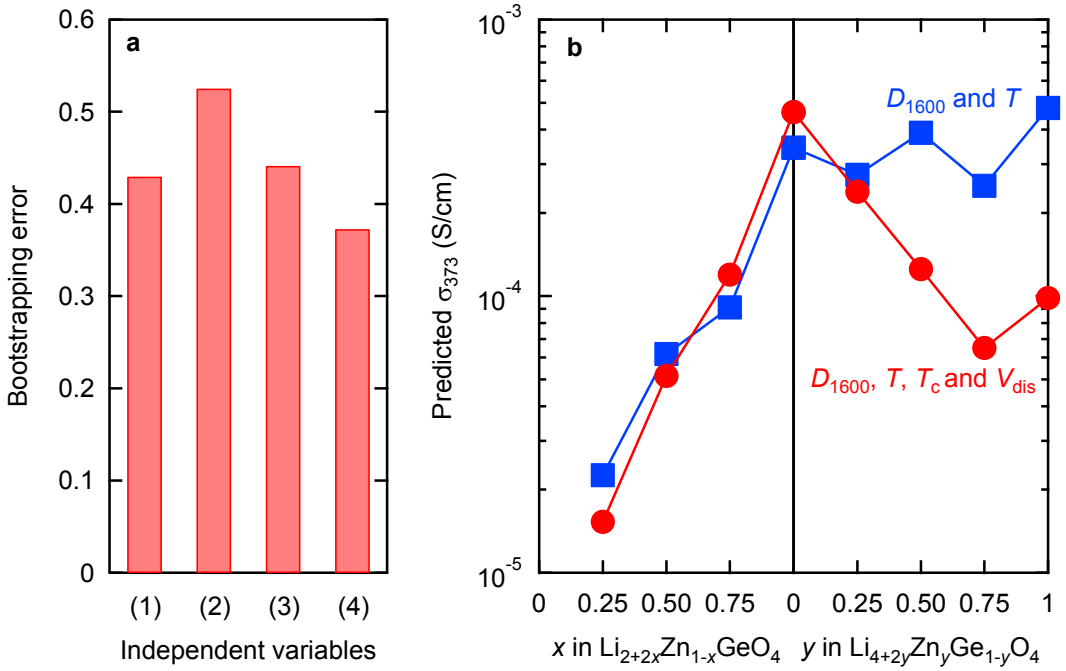

Figure 4.6. (a) Variation in bootstrapping errors for different choices of independent variables used in SVR: (1) D_{1600} and T; (2) D_{1600}, T, and T_c; (3) D_{1600}, T, and V_{dis}; and (4) D_{1600}, T, T_c and V_{dis}. (b) Predicted composition dependence of ionic conductivity at 373K, σ_{373}, for two sets of independent variable.

References

[1] A. D. Robertson, A. R. West and A. G. Ritchie, *Solid State Ionics* **104** (1997) 1-11.

[2] H. Y.-P. Hong, *Mat. Res. Bull.* **13** (1978) 117-124.

[3] U. V. Alpen, M. F. Bell and W. Wichelhaus, *Electrochim. Acta* **23** (1978) 1395-1397.

[4] D. Mazumdar, D. N. Bose and M. L. Mukherjee, *Solid State Ionics* **14** (1984) 143-147.

[5] P. G. Bruce and A. R. West, *J. Solid State Chem.* **44** (1982) 354-365.

[6] P. G. Bruce and I. Abrahams, *J. Solid State Chem.* **95** (1991) 74-82.

[7] T. Mueller, G. Hautier, A. Jain and G. Ceder, *Chem. Mater.* **23** (2011) 3854-3862.

[8] a) G. Hautier, C. Fischer, V. Ehrlacher, A. Jain and G. Ceder, *Inorg. Chem.* **50** (2011) 656-663; b) G. Hautier, A. Jain, H. Chen, C. Moore, S. P. Ong and G. Ceder, *J. Mater. Chem.* **21** (2011) 17147-17153.

[9] R. Jalem, T. Aoyama, M. Nakayama and M. Nogami, *Chem. Mater.* **24** (2012) 1357-1364.

[10] A. Van der Ven and G. Ceder, *J. Power Sources* **97-98** (2001) 529-531.

[11] C. Ouyang, S. Shi, Z. Wang, X. Huang and L. Chen, *Phys. Rev. B* **69** (2004) 104303.

[12] a) D. Panduwinata and J. D. Gale, *J. Mater. Chem.* **19** (2009) 3931-3940; b) C. Arrouvel, S. C. Parker and M. S. Islam, *Chem. Mater.* **21** (2009) 4778-4783.

[13] K. Toyoura, Y. Koyama, A. Kuwabara, F. Oba and I. Tanaka, *Phys. Rev. B* **78** (2008) 214303.

[14] I. Kishida, Y. Koyama, A. Kuwabara, T. Yamamoto, F. Oba and I. Tanaka, *J. Phys. Chem. B* **110** (2006) 8258-8262.

[15] Y. A. Du and N. A. W. Holzwarth, *Phys. Rev. B* **76** (2007) 174302.

[16] H. Moriwake, A. Kuwabara, C. A. J. Fisher, R. Huang, T. Hitosugi, Y. H. Ikuhara, H. Oki and Y. Ikuhara, *Adv. Mater.* **25** (2013) 618-622.

[17] M. Salanne, D. Marrocchelli and G. W. Watson, *J. Phys. Chem. C* **116** (2012) 18618-18625.

[18] M. Xu, J. Ding and E. Ma, *Appl. Phys. Lett.* **101** (2012) 031901.

[19] J. Yang and J. S. Tse, *J. Phys. Chem. A* **115** (2011) 13045-13049.

[20] T. Ikeshoji, E. Tsuchida, T. Morishita, K. Ikeda, M. Matsuo, Y. Kawazoe and S. Orimo, *Phys. Rev. B* **83** (2011) 144301.

[21] P. E. Blöchl, *Phys. Rev. B* **50** (1994) 17953-17979.

[22] G. Kresse and D. Joubert, *Phys. Rev. B* **59** (1999) 1758-1775.

[23] J. P. Perdew, K. Burke and M. Ernzerhof, *Phys. Rev. Lett.* **77** (1996) 3865-3868.

[24] a) G. Kresse and J. Hafner, *Phys. Rev. B* **47** (1993) 558-561; b) G. Kresse and J. Furthmüller, *Phys. Rev. B* 54 (1996) 11169-11186.

[25] S. Nosé, *J. Chem. Phys.* **81** (1984) 511-519.

[26] G. L. W. Hart, *Nature Mater.* **6** (2007) 941-945.

[27] A. Seko and I. Tanaka, *Phys. Rev. B* **83** (2011) 224111.

[28] S. Takai, K. Kurihara, K. Yoneda, S. Fujine, Y. Kawabata and T. Esaka, *Solid State Ionics* **171** (2004) 107-112.

[29] a) Y. Mo, S. P. Ong and G. Ceder, *Chem. Mater.* **24** (2012) 15-17; b) S. P. Ong, Y. Mo, W. D. Richards, L. Miara, H. S. Lee and G. Ceder, *Energy Environ. Sci.* **6** (2013) 148-156.

[30] E. Plattner, H. Völlenkle and A. Wittmann, *Monatsh. Chem.* **107** (1976) 921-927.

[31] H. Völlenkle and A. Wittmann, *Naturwissensch.* **54** (1967) 441.

[32] C.-C. Chang and C.-J. Lin, *ACM Trans. Intell. Syst. Technol.* **2** (2011) 27.

[33] B. Efron and R. J. Tibshirani, *An Introduction to the Bootstrap*, Chapman & Hall, New York, NY, USA (1993).

Chapter 5

General Conclusion

This study is concerned with properties of inorganic solid electrolytes, especially their ionic conductivities. Li-ion diffusivity and migration mechanism in LISICON-type solid electrolytes were investigated using first-principles calculations. We constructed a comprehensive and efficient method to achieve high ionic conductivity using an extensive set of first-principles calculations.

In Chapter 2, total energies of diverse cation configurations in a γ-unit cell size with α, β and γ structures for Li_4GeO_4 and $Li_3Zn_{0.5}GeO_4$ were systematically evaluated by first-principles calculations. Especially in γ-$Li_3Zn_{0.5}GeO_4$, energy stability of an interstitial site is strongly correlated with distances between an excess Li ion at the interstitial site and the neighboring Ge ions. This implies that Li ions diffuse via the sites relatively far from surrounding Ge ions. The lowest energy configurations of Li_4GeO_4 and $Li_3Zn_{0.5}GeO_4$ were obtained from α and γ structures, respectively. Those structures agree to low-temperature phases experimentally confirmed. In α-Li_4GeO_4, energy difference between the most stable configuration and the second stable one is large, 0.56 eV per $Li_{16}Ge_4O_{16}$. This wide energy gap results in an ordered structure even at higher temperatures and thereby low ionic conductivity. On the other hand, in γ-$Li_3Zn_{0.5}GeO_4$, there are many configurations energetically similar to the lowest energy one but those Li-ion spatial arrangements are definitely different from each other. Therefore, $Li_3Zn_{0.5}GeO_4$ can have a disordered structure including a variety of cation configurations. It is surmised that this is why the ionic conductivity of $Li_3Zn_{0.5}GeO_4$ is much higher than that of Li_4GeO_4. It is possible to evaluate metastable phases from the energy distributions. Our results suggest that γ-Li_4GeO_4 and α-$Li_3Zn_{0.5}GeO_4$ have the possibilities of exhibiting ionic conductivities higher than that of the most stable phase.

In Chapter 3, we evaluated Li-ion diffusion in ionic conductors with the γ-LISICON structure using the migration path search simulations and the FPMD simulations at high temperatures over 800 K. The activation energies statistically estimated by the FPMD are close to the low-temperature experimental ones. This implies that the ionic conduction mechanism is the

same over two temperature regions. In the case of oxides such as $Li_{2+2x}Zn_{1-x}GeO_4$ and $Li_{3+x}Ge_xP_{1-x}O_4$, tetrahedral sites are fully occupied and excess Li ions corresponding to x per formula unit partially occupy octahedral sites which have edge sharing with [GeO_4]. We found that Li ions mainly diffuse by the cooperative mechanism in which an excess Li ion at an octahedral site moves to a neighboring tetrahedral site and the Li ion at the tetrahedral site simultaneously moves to another neighboring octahedral site. Thus, the conduction carrier is a pair of two neighboring Li ions. On the other hand, in the case of $Li_{3+x}Ge_xP_{1-x}S_4$, more considerable vacancies are formed at tetrahedral sites. This implies that Li ion diffuse by not only the cooperative mechanism but also the single mechanism in which a Li ion at a tetrahedral site moves to a neighboring octahedral site or a Li ion at an octahedral site moves to a neighboring tetrahedral site. Since the conduction carrier of the single mechanism is a single Li ion, the carrier concentration of $Li_{3+x}Ge_xP_{1-x}S_4$ is much larger than that of oxides. This probably leads to the difference of conductivities between sulfides and oxides.

As has been discussed in Chapter 2 and 3, partial occupation on Li sites significantly affects the Li-ion migration mechanism. Namely, Li-ion arrangements associated with disordering are important for high ionic conductivity. In the future it is strongly suggested that we will be able to design more Li-ion disordered solid electrolytes by properly selecting constituent elements and crystal structure.

In Chapter 4, the FPMD simulations for a diverse range of LISICON-based oxides were performed to calculate Li-ion conductivities at high temperature. We also estimated the deflection point in the Arrhenius plot using first-principles calculations based on the cluster expansion method assuming that the point corresponds to ordering and disordering of Li ions on octahedral sites. Moreover, we applied a machine-learning technique to use theoretical and experimental datasets in combination to predict conductivities at 373 K, σ_{373}, of various compositions. The conductivity of γ-Li_4GeO_4 is predicted to be highest and a few times higher than that of the traditional LISICON ($Li_{3.5}Zn_{0.25}GeO_4$). Besides Li_4GeO_4, the following compounds are predicted to exhibit higher σ_{373} than the traditional LISICON with negative formation free energy at 1600 K. These are Li_4SiO_4, $Li_{2+2x}Zn_{1-x}SiO_4$ (for x = 0.5, 0.75), $Li_{3.5}Mg_{0.25}SiO_4$, $Li_{3.25}Al_{0.25}SiO_4$, $Li_{4.25}A_{0.25}Si_{0.75}O_4$ (A = Al or Ga),

$Li_{3.5}A_{0.5}B_{0.5}O_4$ (A = P, and B = Si) and $Li_{3.75}A_{0.25}B_{0.75}O_4$ (A = P or As, and B = Ge or Si). Focused experiments based on these predictions should be performed and are currently being planned.

The present study considered pseudobinary solid solutions with γ-LISICON structure only. However, our methodology is not limited to such systems. Materials with more complex chemistries and structures can be analyzed efficiently in the same way once a database of systematic first-principles calculations is constructed. This method illustrates the potential for rational design of superior Li-ion conductors based on optimization of materials compositions through machine-learning techniques. We believe that this study will accelerate the materials design process for safer and more environmentally friendly energy storage devices.

Acknowledgement

First of all, I would like to express my sincere gratitude to my supervisor, Professor Isao Tanaka at Kyoto University for constant guidance, considerable encouragement and extensive discussion throughout this study. I would like to express my gratitude to Associate Professor Fumiyasu Oba at Kyoto University for useful comments. I would like to thank Assistant Professor Atsuto Seko at Kyoto University for detailed advice on first-principles calculations and machine-learning techniques.

I would like to express my gratitude to Doctor Hiroki Moriwake at Japan Fine Ceramics Center for helpful advice and generous support. I would like to show my sincere appreciation to Doctor Akihide Kuwabara at Japan Fine Ceramics Center for both valuable guidance on first-principles calculations and wide-ranging discussion. Special thanks also to Doctor Craig A. J. Fisher and Doctor Takafumi Ogawa at Japan Fine Ceramics Center for useful advice on molecular dynamics simulations. I would also like to express my gratitude to Associate Professor Yukinori Koyama at Kyoto University for practical advice on the study about lithium superionic conductors. I am deeply grateful to Assistant Professor Ippei Kishida at Osaka City University for meaningful discussion on electronic structure calculations.

I would like to offer my special thanks to the colleagues of both Professor Tanaka's Laboratory at Kyoto University and Nanostructures Research Laboratory at Japan Fine Ceramics Center for constructive discussion and long-term support.

Finally, I want to say my gratitude to my wife Eriko Fujimura for her love, understanding, support, encouragement and sacrifice throughout my study.

Koji Fujimura

2013